5-2010

Mechanical behavior of alloy 230 at temperatures relevant to NGNP program

Sudin Chatterjee
University of Nevada, Las Vegas

MECHANICAL BEHAVIOR OF ALLOY 230 AT TEMPERATURES RELEVANT TO NGNP PROGRAM

by

Sudin Chatterjee

Bachelor of Engineering in Metallurgical Engineering
National Institute of Technology, Rourkela, India
1999

Master of Technology in Materials and Metallurgical Engineering
Indian Institute of Technology, Kanpur, India
2001

A dissertation submitted in partial fulfillment
of the requirements for the

Doctor of Philosophy in Mechanical Engineering
Department of Mechanical Engineering
Howard R. Hughes College of Engineering

Graduate College
University of Nevada, Las Vegas
May 2010

UNLV
UNIVERSITY OF NEVADA LAS VEGAS

THE GRADUATE COLLEGE

We recommend the dissertation prepared under our supervision by

Sudin Chatterjee

entitled

Mechanical Behavior of Alloy 230 at Temperatures Relevant to NGNP Program

be accepted in partial fulfillment of the requirements for the degree of

Doctor of Philosophy in Mechanical Engineering
Mechanical Engineering

Brendan O'Toole, Committee Chair

Ajit K. Roy, Committee Co-chair

WooSoon Yim, Committee Member

Anthony E. Hechanova, Committee Member

Daniel Cook, Committee Member

Edward S. Neumann, Graduate Faculty Representative

Ronald Smith, Ph. D., Vice President for Research and Graduate Studies
and Dean of the Graduate College

May 2010

ABSTRACT

Mechanical Behavior of Alloy 230 at Temperatures Relevant to NGNP Program

by

Sudin Chatterjee

Dr. Brendan O'Toole, Examination Committee Chair
Associate Professor of Mechanical Engineering
University of Nevada, Las Vegas

Dr. Ajit K. Roy, Examination Committee Co-Chair
Professor of Mechanical Engineering
University of Nevada, Las Vegas

Identification and selection of suitable structural materials for heat exchanger application within the purview of the next generation nuclear plant (NGNP) program constitute a major challenge. This challenge stems from the lack of many desired metallurgical and mechanical properties of conventional metallic materials and alloys for applications at temperatures approaching 950 ^{o}C. Nickel (Ni)-base Alloy 230 has been highly recommended as a suitable structural material for such application due to its excellent resistance to high-temperature plastic deformation and superior corrosion resistance in many hostile environments.

Systematic studies on tensile, fracture toughness, creep, stress-rupture and creep-fatigue behavior of this alloy have been performed in this investigation. A gradual reduction in yield and ultimate tensile strength has been observed with increasing temperature, as expected. The room-temperature fracture toughness of this alloy was relatively lower compared to that of other Ni-base alloys. The results of creep testing indicate that Alloy 230 may be resistant to plastic deformation at 750, 850 and 950 ^{o}C at applied stresses not exceeding 10% of its yield strength (YS) at these temperatures. At

0.25YS, this alloy exhibited an enhanced creep deformation at 850 and 950 ^{o}C. The results of stress-rupture testing, performed at 750, 800 and 850 ^{o}C under applied stress levels of 20, 25 and 30 ksi, respectively, have also been presented using different parametric extrapolation techniques. The Larson-Miller (LM) parameter was found to be very useful in predicting the rupture time. However, another approach based on the Minimum Commitment Method (MCM) was also applied that proved to be quite efficient in predicting the creep-rupture behavior of this alloy. Further, the effect of combined creep-fatigue loading on its cracking susceptibility has been studied by imposing different hold times on a triangular waveform associated with cyclic loading under a constant stress-intensity-factor range. These results indicate that the crack-growth-rate of Alloy 230 may be significantly enhanced at higher temperatures even after holding for very short durations. As to the fracture morphology, its mode of failure was changed from transgranular to predominantly intergranular due to the introduction of longer hold times and/or increasing temperature.

TABLE OF CONTENTS

LIST OF TABLES

LIST OF FIGURES

ACKNOWLEDGEMENTS

First and foremost, I offer my prayers to the Almighty, who gave me all the mental strength and courage for preparing this dissertation. I would like to express my sincere thanks and gratitude to my advisors, Dr. Ajit K Roy and Dr. Brendan O'Toole, for their support, patience, and encouragement throughout the course of my Doctoral program. Both Dr. Roy and Dr. O'Toole have taught me innumerable lessons and insights on the workings of academic research in general.

I am thankful to US Department of Energy (DOE) for funding this work under Grant numbers DE-FC07-04ID14566 and DE-AC07-051D141517.

I would also take this opportunity to pay my warm and hearty regards to the other members of my dissertation committee: Dr. Anthony E. Hechanova, Dr. Woosoon Yim, Dr. Daniel P. Cook and Dr. Edward S Neumann for their valuable comments that helped me improving the contents of this dissertation. I would also like to thank my colleagues at Material Performance Laboratory for providing their necessary help and support.

I would like to thank all the faculty and staffs from College of Engineering, Graduate College and Harry Reid Center, who assisted and supported me in various ways during my course of studies. I am especially grateful to Dr. Thomas Hartmann and Dr. Longzhou Ma for their technical support during my final microstructural characterization work.

While I present this dissertation, I can never forget the sacrifices and blessings of my parents, Mr. Subir Chatterjee and Mrs. Kalpana Chatterjee, without whom I could never be what I am. My charming and beautiful wife, Sumi, has always been my inspiration and has provided me with all her love, care and moral support during difficult times. My son,

Shuban always let me forget all my tensions after work and will always remain my strength. My special gratitude to both my elder sisters, Surina and Subina, Jijaji Mr. Prabir Mukherjee, cousin Sunny for their love and moral support. Last but not the least, my special thanks to my Father in-law, Mr. Vivek Banerjee, Mother in-law, Mrs. Ila Banerjee and Brother in-law, Sushant, for their continuous encouragement and support.

CHAPTER 1

INTRODUCTION

The demand for energy has been rising continuously for the past two decades, and is expected to follow a similar trend due to ongoing global industrial expansion and development of many future projects. Therefore, the cost of conventional fossil fuel-derived energy, such as oil and gas, has been increasing steadily. The National Energy Policy proposed in recent years by the United States Department of Energy (USDOE) has been focused on more efficient utilization of nuclear power to generate electricity, and develop alternate sources of energy including hydrogen for many industrial applications [1-3]. Electricity generation using heat from Very-High-Temperature-Reactor (VHTR) has recently been emphasized by the USDOE within the purview of the Next Generation Nuclear Plant (NGNP) program. The NGNP program has been designed to develop hydrogen using 10% of the heat generated from VHTR, while 90% of the heat would be utilized to generate electricity [2].

Figure 1 illustrates a schematic view of the NGNP concept, which will have an operating temperature in the vicinity of 950 ^{o}C. This temperature would be roughly three times higher than that of light water reactors, which are cooled by water and have been extensively used in the United States and around the world for quite some time. In contrast, the high heat generated from VHTR will be transmitted by an inert gas such as helium (He) through a heat exchanger, providing a greater safety during its operation. A very small amount of the generated heat, also known as the process heat, will be transferred to the hydrogen generation plant through two heat exchangers, as shown in Figure 1.1.

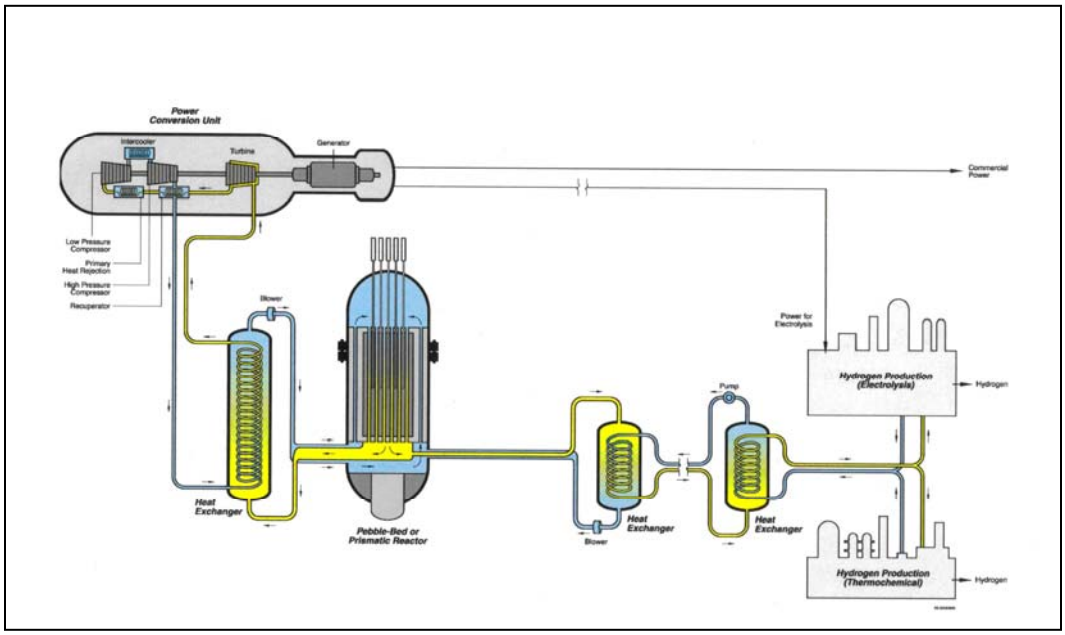

Figure 1.1 NGNP Concept [2]

The NGNP program constitutes a part of Generation IV Nuclear Energy Systems Initiative of USDOE. The current projects under the NGNP program are focused on many areas including the validation of reactor physics and core design analyses tools, development and validation of reactor thermal-hydraulic and mechanical design analysis tools, materials research, power-conversion unit assessments, and safety and risk analysis. The scope of these projects consists of project design, system design and analysis methodology, and fuel development and qualification. Nevertheless, the development of next generation nuclear systems requires extensive research and development efforts to identify, qualify and codify structural materials capable of withstanding extreme operating conditions including unusually high reactor temperature, high neutron flux, highly corrosive environments, yet providing long lifetime expectancy [4].

Nickel (Ni)-base Alloy 230 and Alloy 617 are two reference candidate structural materials for components such as intermediate heat exchangers in high-temperature gas-cooled reactor system. The materials for the primary circuit must exhibit good thermal stability for long operating time, good creep strength, and should be easily formable and weldable. Extensive research work has already been performed at the Materials Performance Laboratory (MPL) of UNLV for the past three years involving Alloy 617 to evaluate its high-temperature tensile properties, crack-growth-rate (CGR), fracture toughness, and creep deformation at elevated temperatures [5, 6]. However, very limited data exist in the open literature for Alloy 230.

There are indications [7, 8] that Alloy 617 possesses superior creep resistance compared to that of Alloy 230 but has relatively poor fatigue properties at elevated temperatures. Further, Alloy 617 is known to exhibit comparatively poor corrosion resistance due to its less-protective oxide films leading to internal oxidation and decarburization. Also, the presence of high cobalt (Co) content in this Alloy may give rise to potential radioactive contamination [4]. Alloy 230 was developed in 1980s primarily to sustain many hostile industrial environments, and is believed to possess considerably good creep resistance at elevated temperatures. In view of this rationale, Alloy 230 was considered for evaluation of its creep deformation behavior at temperatures relevant to the NGNP program using the existing load frames at MPL. Simultaneously, efforts have been made to evaluate the tensile properties, fracture toughness and synergistic creep and fatigue interactions (creep-fatigue) of Alloy 230 for prospective application in the NGNP program.

Creep is a phenomenon of temperature-induced progressive deformation of a structural material at a constant load or stress [9, 10]. It is well known that the strength of metals and alloys can decrease with increasing temperature due to enhanced plasticity under tensile loading by virtue of faster dislocation motion through their grain boundaries. Other deformation mechanisms such as changes in slip systems and grain boundary diffusion, etc. can also come into play. At elevated temperatures, the strength of metals and alloys can also become very much dependent on the strain rate under sustained loading.

The temperature-dependency of creep strength may vary depending on the types of material. A temperature that could be high for one material may not be so for another. Thus, to differentiate the temperature effect on materials' properties, a term known as a homologous temperature, i.e., the ratio of the testing temperature to the melting temperature on an absolute scale is often used. Generally, time-dependent plastic deformation (creep) of metals and alloys may become significantly important at homologous temperatures of greater than or equal to 0.5 [9, 10]. The melting point of Alloy 230 is known to be approximately 1600 K. A decision was made in this investigation to evaluate the creep deformation behavior of Alloy 230 at temperatures of 750, 850 and 950 ^{o}C that represent intermediate, intermediately-high, and high operating temperatures, respectively for the proposed NGNP system. Thus, these testing temperatures fell within a range of 1023-1223 K. Corresponding to these temperatures, the homologous temperature for Alloy 230 ranged between 0.63 and 0.76, which are well above 0.5.

This investigation is primarily aimed at developing a basic understanding on creep deformation of Alloy 230 under sustained loading at temperatures of 750, 850 and 950 ^{o}C. There are indications in the literature [11-25] that metallurgical microstructures can significantly influence the creep strength of structural materials. Parameters such as grain size, stacking fault energy, sub-grain size, distribution of dislocations at the sub-boundaries and in the interior of the sub-grains, etc. can play significant role on the extent of deformation due to creep [11-25]. The presence of tungsten (W) in this Alloy is very effective in lowering the stacking fault energy of Ni. Low stacking fault energy is expected to increase the activation energy required for thermally-activated cross-slip of screw dislocations during creep deformation [11].

Other important microstructural characteristics influencing the creep strength of Alloy 230 are the presence of grain boundary and intragranular precipitates [24, 25]. Literature [25] indicates that there are two types of carbide precipitations in Alloy 230. The first one is M_6C carbide of type Ni_3W_3C, which could result from precipitation during thermomechanical processing and is expected to resist the grain boundary migration and sliding at elevated temperatures, particularly when present at the triple points. The second type of precipitate is the $M_{23}C_6$ carbides, which is chromium-rich and can also result from thermomechanical processing. However, the morphology of this type of precipitate depends on the cooling rate following rolling and annealing operations. Intragranular and continuous grain boundary precipitates of $M_{23}C_6$ carbides are beneficial for creep strength rather than discontinuous precipitates [24]. Therefore, a characterization of microstructural aspects by analytical tools such as transmission

electron microscopy (TEM) was performed in this investigation to develop a creep deformation mechanism of Alloy 230.

Apart from the microstructural effects, the creep strength of a material can depend on the applied stress and the duration of sustained loading. The ASTM Designation E 139-06 [26] recommends that creep testing be performed at stresses that would result in 1% strain following 100,000 hours (approximately, 11.5 years) of loading. However, testing for such a long period is impractical since results are needed within a reasonable timeframe. Therefore, it is widely accepted in the scientific and engineering communities to assume a material to be creep resistant if its total strain does not exceed 1% following 1000 hours of loading at a desired temperature [27].

Another approach to the prediction of long-term creep properties is the performance of stress rupture testing that needs much shorter duration. Stress rupture testing is very similar to creep testing with a difference that, during the stress-rupture testing, the specimens are normally loaded at higher stresses and testing is continued until the sample fails. Usually, stress levels applied in this type of testing are selected so as to have a rupture time ranging between 30 and 300 hours [26]. The resultant rupture usually occurs by intergranular or intragranular cracking due to nucleation, growth, and link-up of grain-boundary voids [28-30].

As indicated earlier, carbide precipitates of specific types have significant effect in influencing the creep properties of Ni-base alloys. Unlike creep, the stress rupture properties are enhanced by discontinuous carbide precipitation, thus providing an easy fracture path [31, 32]. The primary goal of stress rupture testing was to evaluate the long-term creep deformation behavior of Alloy 230 by using different empirical models based

on Larson-Miller (LM) analysis [33], Orr-Sherby-Dorn (OSD) analysis [34] and Manson-Hafred (MH) methodology [35]. Apart from the empirical techniques, efforts were made to predict the creep-rupture properties of Alloy 230 using a generalized time-temperature-stress regression model based on the Minimum Commitment Method (MCM) [36]. Although, it is difficult to precisely determine the long-term creep properties of this alloy beyond the ranges of the tested parameters using such methods, it may be closely approximated using a reasonable factor of safety, thus leading to the development of master plots for long-term predictions.

In addition to time and temperature-dependent deformation, Alloy 230 would also be subjected to thermal stresses generated from fluctuating temperatures associated with alternate heating and cooling of the heat exchanger during transfer of nuclear heat into the power generation plants. Thus, another requirement for Alloy 230 for NGNP application is to ensure its adequate resistance to failure under cyclic loading (thermal fatigue). Simultaneously, it is necessary to determine the fracture toughness of this alloy in the presence of sub-critical flaws or cracks that may exist in the as-received condition. In view of this rationale, the fracture toughness of Alloy 230 was also determined at ambient temperature using the elastic-plastic-fracture-mechanics (EPFM) concept [37-40]. Additionally, the combined effect of hold time and cyclic loading (creep-fatigue) on the crack-growth behavior of Alloy 230 was evaluated by imposing different hold times on a triangular waveform associated with cyclic loading under a constant stress-intensity-factor range. The creep-fatigue behavior study of this alloy was performed within a temperature range of 600-800 ^{o}C. Finally, efforts were made to evaluate the

microstructural aspects of creep-fatigue interaction of Alloy 230 using optical and scanning electron microscopy (SEM).

The test matrix for this investigation was developed based on the recommendations from the materials consortium within the NGNP program that consisted of participants from both the National Laboratories and Universities of the United States of America. The complete test matrix and scope of work defined by the materials consortium are given in Appendix A. Table 1.1 shows the test matrix that was carried out within the scope of the current investigation.

Table 1.1 Test Matrix for Alloy 230

Type of Testing	Environment	Temperature (^{o}C)	Loading Conditions
Tensile	Air	Ambient, 150, 300, 500, 750, 850, 950	Strain rate = 10^{-3} sec^{-1}
Creep	Air	750, 850, 950	10 and 25% of yield strength corresponding to a specific test temperature
Stress-Rupture	Air	750, 800, 850	138, 172, 207 MPa
Fracture Toughness	Air	Ambient*	variable
Creep-Fatigue	Air	600, 700, 800	Constant stress-intensity-factor range, $\Delta K = 25$ $MPa\sqrt{m}$

* Testing could not be performed at elevated temperatures due to both equipment and funding constraint.

CHAPTER 2

EXPERIMENTAL: TEST MATERIAL AND SPECIMENS

2.1. Test Material

Alloy 230 is a nickel-chromium-tungsten-molybdenum (Ni-Cr-W-Mo) alloy that combines excellent high-temperature tensile strength, outstanding resistance to deformation in oxidizing environments at temperatures up to 1149 °C, excellent corrosion resistance in nitriding environments, and superior long-term thermal stability [41]. It can be readily fabricated and formed, and is castable. Other desirable properties of this alloy include lower thermal expansion compared to most high-temperature alloys, and a significant resistance to grain coarsening during prolonged exposure at elevated temperatures. Alloy 230 has excellent weldability. It may also be forged or otherwise hot-worked, provided it is held at 1177 °C for sufficient time to heat the entire piece uniformly. This alloy can also be readily formed by cold-working due to its moderate ductility. Hot- or cold-worked Alloy 230 can be annealed and rapidly cooled to restore its desired properties.

Wrought Alloy 230 is usually furnished in a solution annealed condition. The typical annealing temperature ranges from 1177 to 1246 °C. Subsequently, it can be rapidly cooled or water-quenched to develop the desired metallurgical and mechanical properties. Alloy 230 used in this investigation was procured from the Haynes International Inc. Initially, two heats (Heat Numbers 830557766 and 830557896) were used to prepare the creep and stress rupture specimens. Later, a third heat (Heat Number 830587843) was procured to fabricate compact-tension (CT) specimens for evaluation of fracture toughness and creep-fatigue behavior of this alloy. All three heats were received from the

vendor in a heat-treated condition. The chemical composition and the room temperature tensile properties of the test materials are given in Tables 2.1 and 2.2, respectively.

Table 2.1 Chemical Composition of Alloy 230 (wt %)

Heat Number	C	Mn	Fe	Si	Cr	Ni	Al	Co	Mo	W
830557766	0.10	0.57	2.51	0.41	21.76	58.56	0.23	0.15	1.37	14.3
830557896	0.11	0.53	1.34	0.37	22.43	59.46	0.29	0.21	1.34	13.9
830587843	0.11	0.50	0.42	0.39	22.01	60.76	0.40	0.10	1.25	14.0

Table 2.2 Ambient-Temperature Tensile Properties of Alloy 230

Heat Number	YS, ksi (MPa)	UTS, ksi (MPa)	%El	%RA	Hardness (R_B)
830557766	54 (372)	127 (876)	49	55	91
830557896	52 (361)	119 (820)	46	43	92
830587843	50 (348)	115 (793)	47	44	90

2.2 Test Specimens

Tensile testing was performed using a 4-inch long smooth cylindrical specimen having a gage length of 1-inch, and a gage diameter of 0.25-inch. The specimen used in tensile testing is shown in Figure 2.1. Creep testing was performed using a 4-inch long smooth cylindrical specimen having a gage length of 1.48-inch, as shown in Figure 2.2. These specimens had grooves at both ends so as to attach an extensometer for measurement of strain. Stress rupture testing was conducted using a smooth cylindrical specimen having a 3.6-inch length and two notches machined within a gage length of 1.1-inch, as shown in Figure 2.3. These two notches were placed at a distance of 0.5 inch from the center of the gage section. The notch diameter and root radius were 0.266-inch and 0.0073-inch, respectively. The fracture toughness (J_{IC}) of this alloy was determined

using 1-inch thick CT specimens, based on the elastic-plastic-fracture-mechanics (EPFM) concept [42], which is shown in Figure 2.4. Finally, the crack-growth-rate (CGR) of this alloy under creep-fatigue conditions was determined by using 0.25-inch thick CT specimens (Figure 2.5) that were machined according to the ASTM Designation E 647-2000 [43].

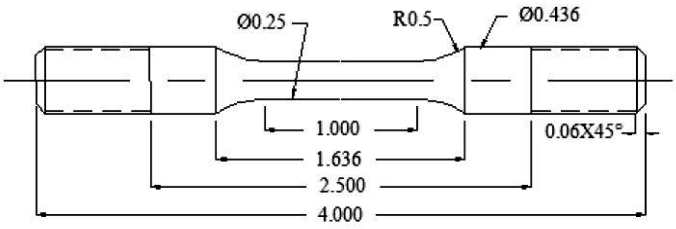

(a) Specimen dimensions (Inch)

(b) Pictorial View

Figure 2.1 Tensile Specimen

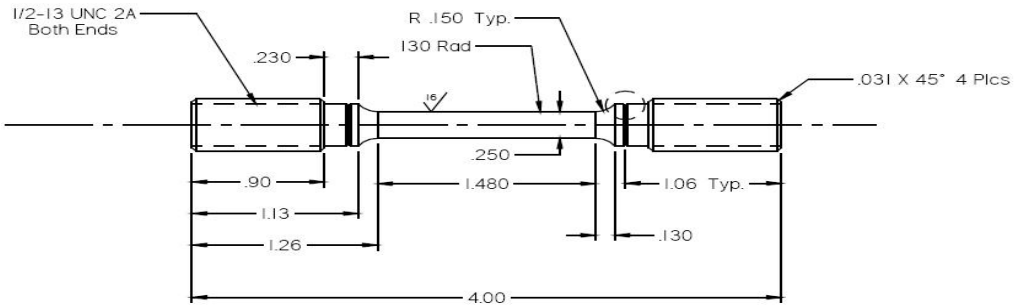

(a) Specimen Dimensions (Inch)

(b) Pictorial View

Figure 2.2 Specimen used in Creep Testing

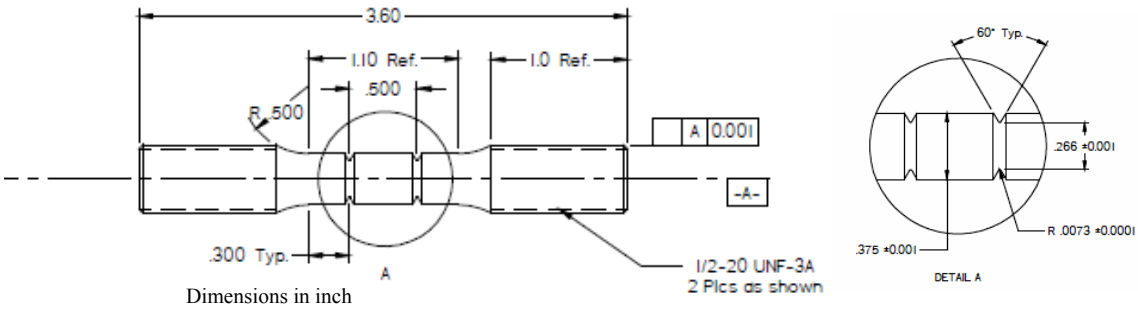

Figure 2.3 Specimen used in Stress Rupture Testing

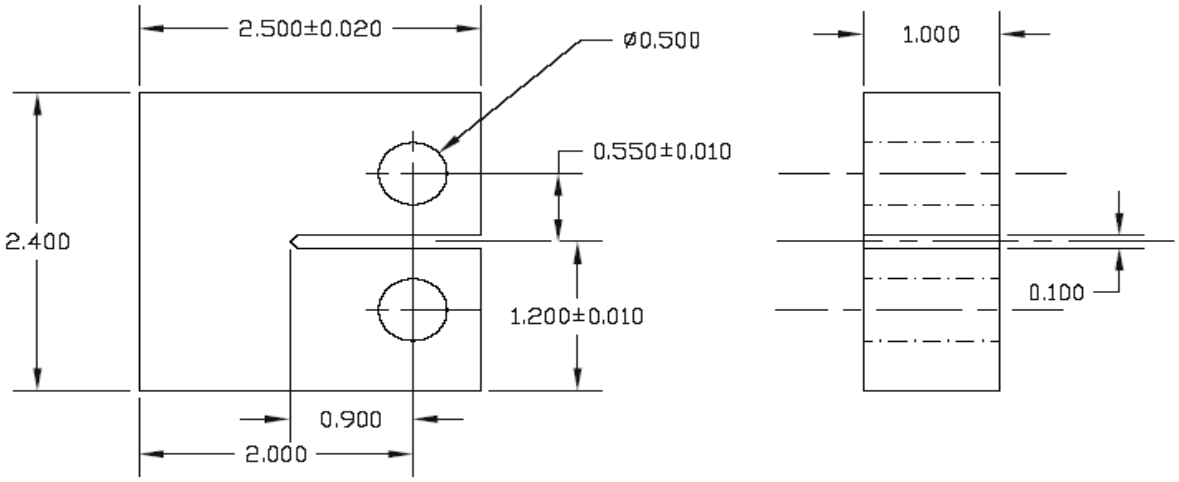

(a) Specimen Dimensions (Inch)

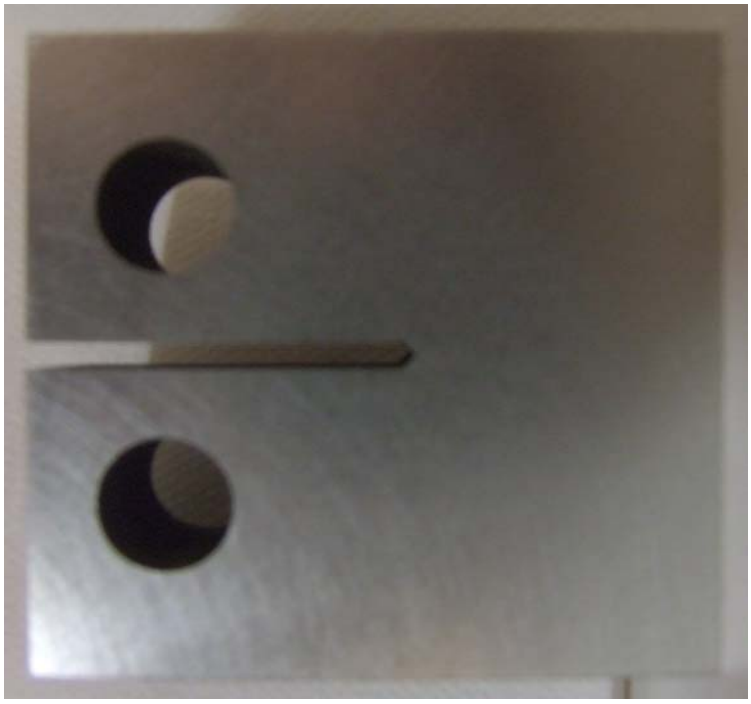

(b) Pictorial View

Figure 2.4 Specimen used in J_{IC} Measurement

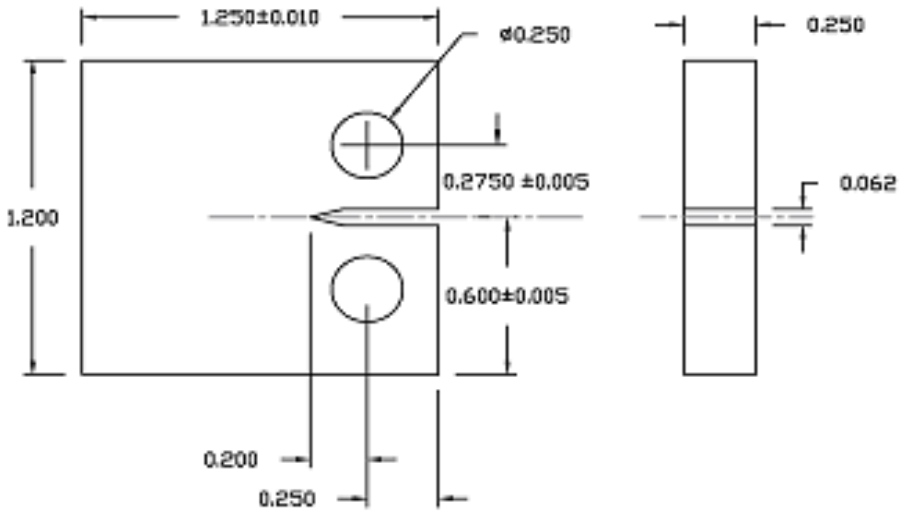

(a) Specimen Dimensions (Inch)

(b) Pictorial View

Figure 2.5 Specimen used in Creep-Fatigue Testing

CHAPTER 3

EXPERIMENTAL PROCEDURES

As indicated earlier, this investigation is focused on the evaluation of mechanical properties of Alloy 230 at temperatures relevant to the intermediate heat exchanger for the NGNP program. Since the anticipated design life of components for NGNP application is relatively high, evaluation of time-dependent deformation, and rupture life determination are necessary. Therefore, creep and stress rupture testing were performed in this study. Further, an effort was made to generate baseline tensile data at ambient and elevated temperatures. These tensile data were needed to select the magnitude of stresses to be applied in creep testing at specific temperatures. Certain percentages of the YS values at the selected testing temperatures were considered. Plane strain fracture toughness (J_{IC}) of Alloy 230 was also determined at ambient temperature using pre-cracked CT specimens. However, J_{IC} testing could not be performed at elevated temperatures due to a limitation of testing equipment. CT specimens of different dimensions were used to evaluate the crack-growth behavior of this alloy under creep-fatigue conditions using an in-situ crack monitoring device (DCPD) at different temperatures.

Optical microscopy was used to characterize the metallurgical microstructures of Alloy 230 including the grain size, volume fraction and size of precipitates. The extent and morphology of failure of all tested specimens were determined by using SEM. Finally, TEM was used to develop a basic understanding of different types of deformations as functions of metallurgical and mechanical variables. Experimental

procedures used in the evaluation of tensile, J_{1C}, creep, stress rupture, creep-fatigue, microstructures and fractography of Alloy 230 are described in the following subsections.

3.1 Tensile Testing

The tensile properties including the yield strength (YS), ultimate tensile strength (UTS), and the ductility in terms of percent elongation (%El) and percent reduction in area (%RA) were evaluated using an Instron testing equipment (Model 8862). Smooth cylindrical specimens were loaded in tension at a strain rate of 1×10^{-3} sec^{-1} according to the ASTM Designation E 8-2004 [44]. Duplicate specimens were tested under each experimental condition, and the average values of the measured parameters were recorded. The experimental data including the load, engineering stress (s) and engineering strain (e) were recorded in the data file. The engineering stress versus strain (s-e) diagram was automatically generated using Bluehill 2 software program [45]. The magnitudes of YS, UTS, and %El (based on Linear Variable Displacement Transducers) at each temperature were also determined using this software. Upon completion of testing, the magnitudes of %El and %RA were calculated using Equations 3.1 through 3.4.

$$\%El = \left(\frac{L_f - L_0}{L_0} \right) \times 100 \qquad \text{Equation 3.1}$$

$$\%RA = \left(\frac{A_0 - A_f}{A_0} \right) \times 100 \qquad \text{Equation 3.2}$$

$$A_0 = \frac{\pi D_0^{\,2}}{4} \qquad \text{Equation 3.3}$$

$$A_f = \frac{\pi D_f^{\,2}}{4} \qquad \text{Equation 3.4}$$

where A_0 = Initial cross sectional area (inch^2)

A_f = Cross sectional area at failure (inch^2)

L_o = Initial overall length (inch.)

L_f = Final overall length (inch.)

D_o = Initial gage diameter (inch.)

D_f = Final gage diameter (inch.)

3.1.1 Instron Testing Machine

The Instron testing machine, shown in Figure 3.1, had an axial load transducer capacity of 22.5 kip (100 kN). It had a single screw electromechanical top actuator that was developed for static and quasi-dynamic cyclic testing at slow speed. This equipment consisted of a large heavy-duty load frame with an adjustable crosshead attached to the top grip, and a movable actuator with another grip at the bottom to enable loading and unloading of the test specimen. The axial motion was controlled by force, displacement, or an external signal from the strain gage. The specimen was mounted between the two grips and pulled by the movable actuator. The load cell measured the applied force on the tensile specimen. The movement of the upper crosshead relative to the lower one measured the strain within the specimen and consequently, the applied load. The key specifications of this equipment are given in Table 3-1.

Table 3-1 Specifications of Instron Model 8862 System

Load Capacity	Total Actuator Stroke	Maximum Ramp Rate	Actuator Attachment Threads	Load Cell Attachment Threads
100 kN	100 mm	350 mm/min	M30 × 2	M30 × 2

Figure 3.1 Instron Testing Machine

A split furnace (Model 3320) was attached to the testing system for evaluating the tensile properties at elevated temperatures in air. This furnace was capable of sustaining a maximum temperature of 1540 ^{o}C and had two layers of micro-pores and ceramic fibers over them. Six U-shaped molybdenum disilicide heating elements were used for attaining the desired testing temperature. The specimen temperature during straining was monitored by three B-type thermocouples contained inside this furnace. A separate control panel (model CU666F) was used to perform the overall monitoring of temperature during tensile loading. A maximum heating rate of 8 ^{o}C per minute could be achieved by this control panel. However, a slow heating rate of 4 ^{o}C per minute was used during testing to prevent any thermal shock of the pull rods and the fixtures inside the furnace. Since the grip material could undergo phase transformation and plastic

deformation at elevated temperatures during straining of the specimen, a pair of custom-made grips of high strength and temperature resistant MarM 246 alloy was used to hold the tensile specimen in an aligned position.

3.2 Fracture Toughness Evaluation

Fracture toughness of metals and alloys can be determined by application of two concepts, namely linear elastic fracture mechanics (LEFM) and elastic plastic fracture mechanics (EPFM). The LEFM concept involves the use of CT specimens with larger thickness to comply with limited plasticity at the crack-tip (Plane-strain condition) as prescribed by the ASTM Designation E 399-1999[46]. However, the use of thicker specimens may be unrealistic from a practical point of view. So, the principle of EPFM is often applied to evaluate the fracture toughness of structural materials in terms of plane stress fracture toughness (J_{1C}).

J_{1C} testing involving Alloy 230 was performed in this investigation according to the ASTM Designation E 813-1989, using 1-inch thick CT specimens [42]. Two types of J_{1C} testing method exist, namely single-specimen technique and multiple-specimen technique. The multiple-specimen technique requires at least five specimens to be tested at a specific temperature to determine the J_{1C} value. Thus, it involves higher cost and longer test duration. Therefore, to minimize cost and time, the single-specimen technique was employed in this investigation to determine J_{1C} at ambient temperature using an Instron testing machine. Testing could not be performed at elevated temperatures due to both equipment and funding constraint. A "J_{1C} fracture toughness software" [47], provided by the Instron corp., was used to calculate and validate the measured J_{1C} value.

For J_{1C} determination, the CT specimens were pre-cracked in the Instron equipment up to an approximate length of 2 mm using a load ratio (R) value of 0.1 and a frequency of 1 Hz. The maximum load during pre-cracking was maintained at 20 kN. Later the specimens were subjected to several loading and unloading sequences (15 to 30). Due to these loading/unloading sequences, the load-line-displacement (LLD) or, the crack-opening displacement (COD) i.e. the gap between the two arms of CT specimens was increased. The magnitude of LLD was measured by a knife-edge extensometer, which was attached to the specimen arms at the start of the J_{1C} testing. A maximum travel distance of this extensometer was maintained at +/- 2 mm. A pictorial view of the J_{1C} test setup, showing the extensometer arrangement, is illustrated in Figure 3.2.

A typical load versus LLD plot is shown in Figure 3.3. The shaded area, shown in Figure 3.4, represents loading/unloading energy (J-Integral/J) required for increment of crack.

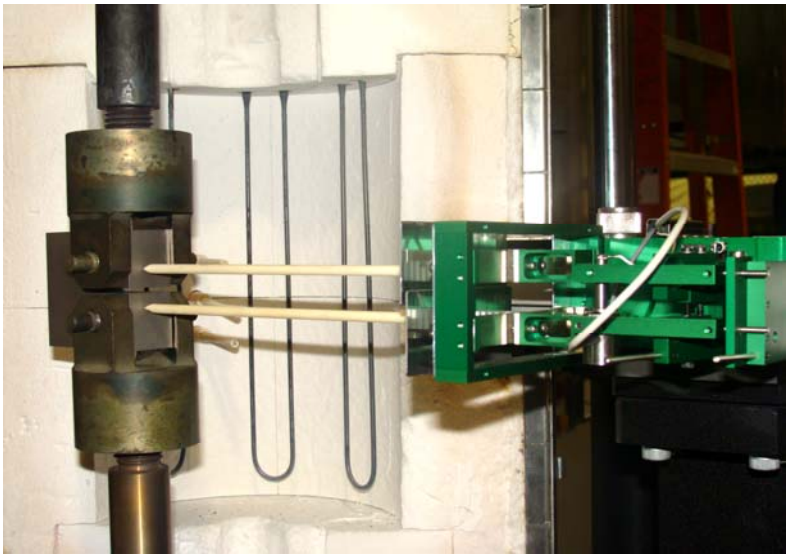

Figure 3.2 J_{1C} Test set-up

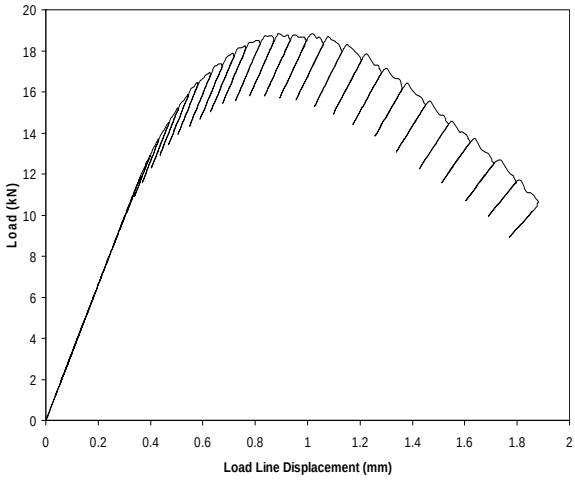

Figure 3.3 Loads versus LLD Plot

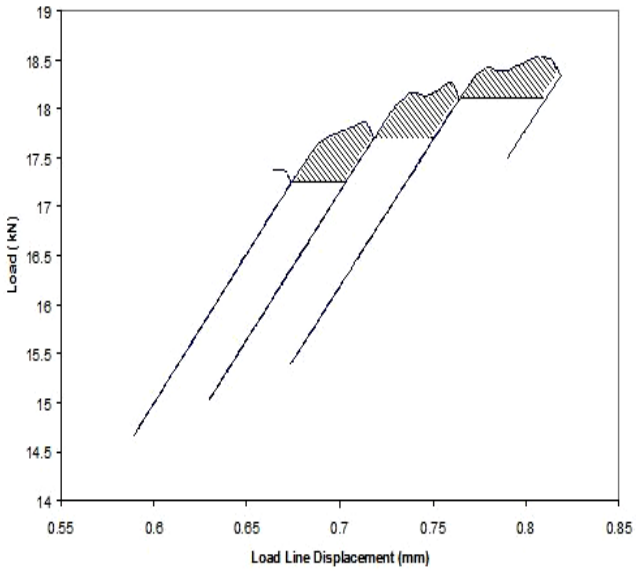

Figure 3.4 Areas representing J-Integral

The J-Integral value for each area will be calculated by using Equation 3.5 [42].

$$J = J_{elastic} + J_{plastic} \qquad \text{Equation 3.5}$$

where $J_{elastic} = \frac{K^2}{E}\left[1 - \nu^2\right]$

$$K = \text{Stress-intensity-factor } (\text{MPa}\sqrt{\text{m}}) = \left[\frac{P}{(BB_N W)^{0.5}}\right] X\, f\left(\frac{a}{W}\right),$$

P = Load (N),

B = Specimen Thickness (mm),

B_N = Net specimen thickness (mm) = B, in present study,

W = Width of the specimen (mm),

E = Elastic modulus of the material = 211 GPa, and

ν = Poisson's ratio of the material (=0.3)

$$f\left(\frac{a}{W}\right) = \text{Geometric factor} = \frac{\left[2+\frac{a}{W}\right]\left[0.866+4.64\frac{a}{W}-13.32\left(\frac{a}{W}\right)^2+14.72\left(\frac{a}{W}\right)^3-5.6\left(\frac{a}{W}\right)^4\right]}{\left(1-\frac{a}{W}\right)^{\frac{3}{2}}}$$

$$\text{and } J_{plastic} = \frac{\eta_{pl}}{Bb}\int_0^{v_{pl}} P dv_{pl}$$

$$\Rightarrow J_{plastic} = \frac{\eta_{pl}}{Bb} X\, A_{pl}$$

where b = Uncracked ligament (mm),

$$\eta_{pl} = 2 + 0.522\frac{b}{W}$$

v_{pl} = Plastic displacement (mm) (LLD/COD), and

A_{pl} = Area corresponding to each loading/ unloading sequence (mm^2)

Each calculated J value, was then plotted against the corresponding crack extension (Δa), as shown in Figure 3.8. The crack extension (a_i) for each sequence will be measured using the unloading compliance principle, based on Equation 3.6 [48-49].

$$a_i/W = 1.000196 - 4.06319u_{LL} + 11.242u_{LL}^2 - 106.043u_{LL}^3 + 464.335u_{LL}^4 - 650.677u_{LL}^5$$

Equation 3.6

where $u_{LL} = \frac{1}{\left[B_e E C_i\right]^{0.5} + 1}$

B_e = Effective thickness of the CT specimen (mm) = $[B - (B - B_N)^2/B] = B$ (since $B = B_N$), in current study

C_i = Specimen load line elastic compliance on an unloading/reloading sequence ($\Delta v/\Delta P$) (mm/N)

Δv = Increment in LLD/COD (mm)

ΔP = Change in load (N)

The data obtained from the J-Integral vs. Crack-Extension plots were fitted to a power law curve and four parallel lines were drawn, as shown in Figure 3.5. These lines were identified as blunting line, 0.15-mm exclusion line, 1.5-mm exclusion line and 0.2-mm exclusion line, respectively.

The resultant data was considered valid if at least one J-Δa point lies between the 0.15-mm extension line and a line parallel to the blunting line at an offset of 0.5-mm from the blunting line. The point of intersection of the power law curve and the 0.2-mm exclusion line (as shown in Figure 3.5) was taken as J_Q, or a conditional J_{1C} value. J_Q was considered as the J_{1C} value of the material if it met the following two criteria

1. Thickness (B) of the specimen > [25 J_Q / σ_Y], where σ_Y = effective yield strength of the material = average of the yield and ultimate tensile strength of the material = [σ_{YS} + σ_{UTS}] / 2
2. Initial uncracked ligament (b_0) > [25 J_Q / σ_Y]

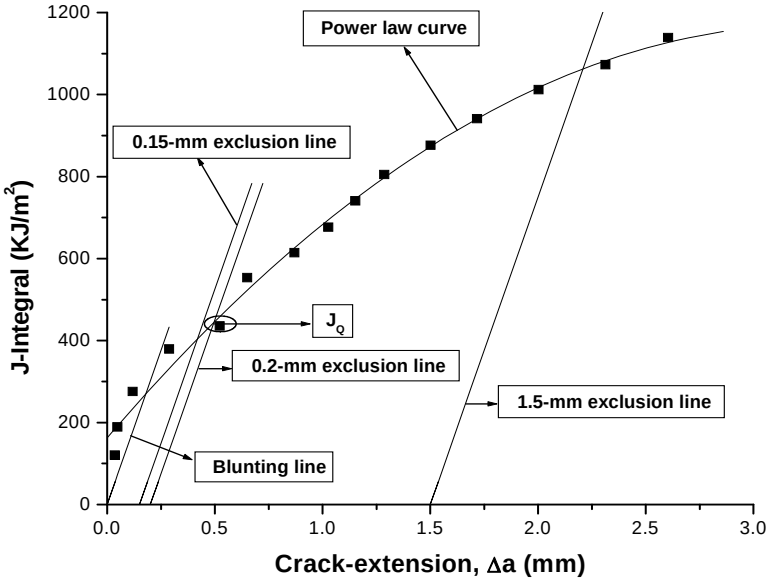

Figure 3.5 Determination of J_Q using J-Integral versus Δa Plot

K_{1C} can be computed [42, 50] from the J_{1C} value of a material using Equation 3.7, as shown below.

$$K_{1C} = \sqrt{J_{1C} \times E \times \left(1 - \nu^2\right)} \qquad \text{Equation 3.7}$$

J_{1C} can also be related to the crack-tip-opening-displacement (CTOD) according to Equation 3.8, given below

$$\delta = \frac{K_1^2}{mE\sigma_{YS}} \qquad \text{Equation 3.8}$$

where δ = CTOD (mm)

$K_1 = K_{1C}$ value of the material (MPa√m)

m = A constant = 2 for plane-strain condition

σ_{YS} = Yield strength of the material (MPa)

3.3 Creep Testing

Creep is a time-dependent deformation phenomenon of structural materials that occurs under a sustained loading condition at elevated temperatures. Creep testing was performed in this study in accordance with the ASTM Designation E 139-06 [26] using ATS loading frames (Series 3210), shown in Figure 3.6, having an arm ratio of 20:1. Smooth cylindrical specimens having two circular grooves were used in these tests. The elongation at the gage section was measured by using two extensometers, as shown in Figure 3.7. The average elongation measured by the left and right extensometers was taken into consideration for estimating the resultant deformation of the tested specimen at a constant load.

The testing equipment consisted of four K-type thermocouples to monitor the specimen temperature. Four connecting ports were attached to the load frame, where one end of thermocouple was connected. Three thermocouples were firmly wrapped up at three locations of the specimen (top, middle and bottom) to monitor its temperature during testing. Windows Computer Creep System (WINCCS) software was used for automatic data acquisition. Fourth slot of the thermocouple port was used to measure the room temperature for reference.

The split tube furnace (model 3210) had three zones. This furnace had a heating capability of heating specimens up to 1100 ^{o}C. Kanthal A1 was used as a heating element in this furnace. Creep tests were conducted at temperatures of 750, 850 and 950 ^{o}C, each at applied stresses corresponding to 10 and 25% of the YS values of Alloy 230 at these temperatures. Testing temperatures were maintained precisely within +/- 0.3 ^{o}C. Each test

was performed for 1000 hours, except for the testing at 950 ^{o}C and 25% of the YS values where the creep rate was very high and the testing was stopped beyond 470 hours.

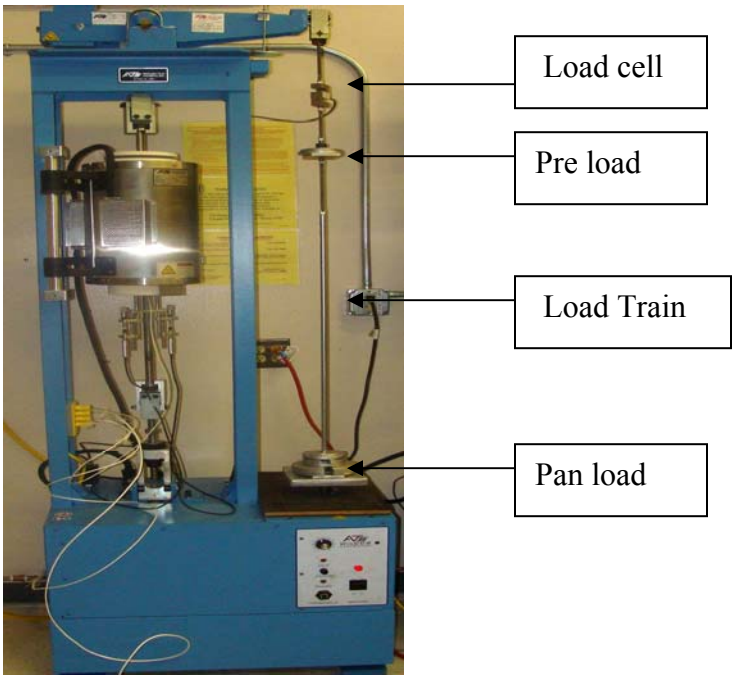

Figure 3.6 Creep Test Setup

Figure 3.7 Extensometer Setup

In general, a three-stage curve is generated in creep testing that can be compared for different testing temperatures. These three regions are known as primary creep, secondary creep and tertiary creep. A schematic representation of a conventional creep curve, showing all three regions, is illustrated [9] in Figure 3.8. The slope of the secondary or steady-state region ($d\varepsilon/dt$, or ε_s^o) is known as the creep rate of the tested material. Initially, there is a rapid elongation of the specimen (ε_0), followed by a reduced rate in the primary stage until a steady-state region is reached. Finally, the deformation rate increases drastically in the tertiary region until the specimen fails.

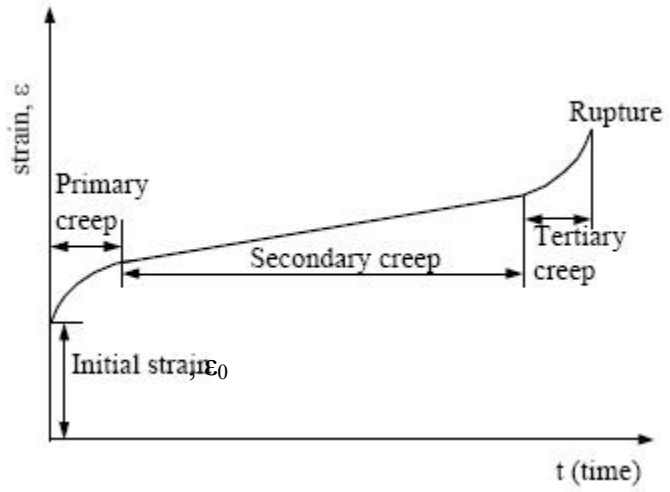

Figure 3.8 Three Stage Creep Curve

Since creep is a thermally-activated phenomenon, the activation energy (Q) needed for plastic deformation in the steady-state region has an important role. The magnitude of Q for creep at a particular stress or load level can be determined using two methods. The first method is based on Equation 3.9 [9].

$$\dot{\varepsilon}_s^{o} = A\exp\left(\frac{-Q}{RT}\right) \qquad \text{Equation 3.9}$$

where A = Pre-exponential complex constant containing the frequency of vibration of the flow unit and the entropy change, and is a factor that depends on the structure of the material,

T = Absolute temperature (K)

Taking natural logarithm on both sides of Equation 3.9, one can get Equation 3.10, as given below.

$$\ln\left(\dot{\varepsilon}_s^{o}\right) = \left(\frac{-Q}{R}\right)\left(\frac{1}{T}\right) + \ln(A) \qquad \text{Equation 3.10}$$

Equation 3.10 represents a straight line having a linear equation (y = mx + c) when ln (ε_s^{o}) is plotted against (1/T). Q can be calculated from this equation as the product of the negative of the slope of this straight line and R (universal gas constant).

The second method of Q calculation is based on the applications of Equations 3.11 and 3.12, as given below. Here the magnitude of A is considered to be constant irrespective of the testing temperature. Thus, rearranging Equation 3.9, one arrives at equation 3.11.

$$A = \dot{\varepsilon}_1^{o} \exp(Q/RT_1) = \dot{\varepsilon}_2^{o} \exp(Q/RT_2) \qquad \text{Equation 3.11}$$

Equation 3.8 can be reached by simplification, as given below.

$$Q = \frac{R\ln(\dot{\varepsilon}_1^{o} / \dot{\varepsilon}_2^{o})}{(1/T_2 - 1/T_1)} \qquad \text{Equation 3.12}$$

where $\dot{\varepsilon}_1^{o}$ and $\dot{\varepsilon}_2^{o}$ are the steady-state creep rates at temperatures T_1 and T_2, respectively.

3.4 Stress Rupture Testing

Stress rupture testing is very similar to creep testing with an exception of higher applied stresses, compared to that of creep test. This type of testing is continued until the specimen fails. Stress rupture testing has been performed in this investigation in accordance with the ASTM Designation E 139-06 [26] using load frames that were also used in creep testing. However, for stress rupture testing, an auto load mode was used, thus maintaining a constant level of applied load until the sample failed. Cylindrical double-notched specimens were used in this type of testing. Since elongation measurements were not needed, extensometers were not used in stress rupture testing. Testing was conducted at 750, 800, and 850 ^{o}C under applied stress levels of 20, 25 and 30 ksi, respectively. Triplicate testing was performed under each experimental condition. Two sets of data were used to determine the different stress rupture parameters, and a third set was used to check the accuracy of the predicted rupture time using the calculated parameters.

3.4.1. Extrapolation of Stress Rupture Data

The primary objective of stress rupture testing was to predict the long-term creep deformation behavior of Alloy 230. However, reliable extrapolation of creep and stress rupture curves to longer times can be made only if structural changes do not occur in the region of extrapolation, thus preventing a change in slope of the curve [9]. For extrapolation of stress rupture data, several parameters have been considered. These parameters include the time, temperature and stress, incorporated into a single expression. The stress at a service temperature can be estimated from a ‘master curve’ generated over a prolonged period at temperatures significantly higher than the operating temperature

range. Some of the commonly accepted expressions for extrapolation are the Larson-Miller (LM) parameter, Orr-Sherby-Dorn (OSD) parameter, and the Manson-Hafred (MH) parameter.

Larson and Miller [33] first introduced the concept of a time-temperature grouping in the form of Equation 3.13.

$$P = T (\ln t_r + C) \qquad \text{Equation 3.13}$$

where P = LM parameter

T = Temperature

t_r = Rupture time, and

C = LM constant

The value of C was originally proposed to be 20, but optimized values ranging between 10 and 40 were subsequently accepted, depending on a specific type of material. For common usage, T is expressed in absolute unit and t in hours. In the current work, the value of C was determined from a plot of ln (t_r) versus 1/T corresponding to different applied stress levels. A linear relationship was observed, which was allowed to converge to a single point as the value of 1/T approached zero. This point along the vertical axis was taken as an approximate value of C.

Unlike the LM plot, the relationship between ln (t_r) and 1/T under different stress levels was manifested as parallel lines without any convergence to a single point in the analysis of the OSD parameter [34]. The OSD parameter is expressed as θ, which can be given by Equation 3.14.

$$\theta = \ln t_r - \frac{Q}{2.3RT} \qquad \text{Equation 3.14}$$

Equation 3.14 also represents a linear relationship for which the slope can be given by -Q/2.3R, where Q is the activation energy for creep deformation and R is the universal gas constant.

The expression for the MH parameter $[f(\sigma)]$ is given by Equation 3.15, which is somewhat different from that of the LM and OSD parameters in that $\ln t_r$ is plotted as a function of T, causing the lines to intersect at coordinates given by T_a and $\ln t_a$, respectively [35].

$$f(\sigma) = \frac{(\ln t_r - \ln t_a)}{(T - T_a)} \qquad \text{Equation 3.15}$$

All three parameters (LM, OSD and MH) are shown in Table 3.2. The different equations, shown in this Table, were used to calculate the various stress-rupture parameters and subsequently analyzed for comparison purpose.

Table 3.2. Stress Rupture Test parameters

LM Parameter	$P = T(\ln t_r + C)$	t_r is the time to rupture in hours, T is the absolute temperature, and C is a constant
OSD Parameter	$\theta = \ln t_r - \frac{Q}{2.3RT}$	Q is a characteristic activation energy for the process determined from the creep experiments and R is the universal gas constant
MH Parameter	$f(\sigma) = \frac{(\ln t_r - \ln t_a)}{(T - T_a)}$	Constants $\ln t_a$ and T_a are the coordinates of the point of convergence

3.4.2 Minimum Commitment Method

A major deficiency of the empirical parameters discussed in section 3.4.1 is that they are assumed to be constant at a specific temperature irrespective of the stress level. Further, none of these parameters consider the effect of metallurgical instabilities. In this

regard, the minimum commitment method (MCM), proposed by Manson and Ensign [36], holds considerable promise. The basic purpose of MCM is to consider a generalized time-temperature-stress relationship, which has a form given by Equation 3.16.

$$\ln(t_r) + A\,P\ln(t_r) + P = G \qquad \text{Equation 3.16}$$

where t_r = Time to rupture

A = Constant

P = Function of temperature and is given by Equation 3.17

$$P = R_1(T - T_m) + R_2\left(\frac{1}{T} - \frac{1}{T_m}\right) \qquad \text{Equation 3.17}$$

where T = Temperature in absolute scale

T_m = Mid-range temperature of data base

R_1 and R_2 = Constants

G = Function of stress and is given by Equation 3.18

$$G = B + C\log\sigma + D\sigma + E\sigma^2 \qquad \text{Equation 3.18}$$

where B, C, D, E = Constants, σ = Applied Stress

Equations 3.16, 3.17 and 3.18 can be combined to arrive at Equation 3.19, as shown below.

$$\ln t_r = R_1X_1 + R_2X_2 + CX_3 + DX_4 + EX_5 + B \qquad \text{Equation 3.19}$$

where $X_1 = (T_m - T)\,(1 + A \ln t_r)$

$X_2 = (1/T_m - 1/T)\,(1 + A \ln t_r)$

$X_3 = \ln \sigma$

$X_4 = \sigma$

$X_5 = \sigma^2$

Equation 3.19 is a linear equation, where the value of ln ($t_{r)}$ depends on independent variables X_1, X_2, X_3, X_4, and X_5. In order to get a generalized expression for time-temperature-stress relationships given by Equation 3.16 and 3.19, it is necessary to determine the values of seven constants (A, B, C, D, E, R_1 and R_2). The value of 'A' was determined by focal point convergence method, proposed by Manson and Ensign [51]. As indicated in section 3.4.1 the time-temperature plots were assumed to converge to a common point, except for the OSD analysis where the plots of ln (t_r) versus 1/T were assumed to generate parallel lines. A negative inverse of ordinate of this point of convergence was considered to provide the best theoretical A-value for the MCM analysis. Multiple linear regression analysis [52] was used to determine the values of the remaining constants.

3.4.3 Application of Stress-Rupture Parameters and MCM Analysis

The stress rupture parameters, determined from different extrapolation techniques, were used to estimate the time to rupture in stress-rupture testing. It is a common practice by the scientific community to represent the variation of these parameters with stress in a single plot, which is often referred to as the 'master plot' for that particular parameter. The master plot is a best fit line drawn for all estimated values of parameters, which is independent of temperature. It serves as a look-up chart for predicting a particular stress-rupture parameter, and eventually the rupture life using Equations 3.13, 3.14 and 3.15. Efforts have been made in this investigation to construct a master plot involving three stress-rupture parameters discussed earlier. The linear equation obtained from this plot was then used to predict the value of a particular parameter under consideration and substituted in Equations 3.13, 3.14 or 3.15, depending on the chosen parameter. The

strength and accuracy of the best fit line or master plot is judged based on the value of coefficient of determination (R^2) [52], given by Equation 3.20. The value of R^2 can range from 0 to 1, with $R^2 = 1$ being the best fit, and $R^2 = 0$ defining no correlation.

$$R^2 = \left[\frac{n\sum_{i=1}^{n} X_i Y_i - \left(\sum_{i=1}^{n} X_i\right)\left(\sum_{i=1}^{n} Y_i\right)}{\sqrt{n\left(\sum_{i=1}^{n} X_i^2\right) - \left(\sum_{i=1}^{n} X_i\right)^2}\sqrt{n\left(\sum_{i=1}^{n} Y_i^2\right) - \left(\sum_{i=1}^{n} Y_i\right)^2}} \right]^2 \qquad \text{Equation 3.20}$$

where Y_i = Particular Stress Rupture Parameter Data Points, X_i = Stress Data Points

The values of constant considered in the LM analysis, slope in OSD analysis and coordinates (T_a, ln $t_{a)}$ in MH analysis were same as those determined experimentally, as discussed in section 3.4.2. Thus, it was possible to predict the rupture time of Alloy 230 for any particular combination of stress and temperature. Predictions of rupture time were also carried out by using the results of the MCM analysis. A generalized equation was obtained by substituting the values of the constant in Equation 3.19, which enabled the prediction of the rupture time for Alloy 230 for any combination of stress and temperature. However, it was necessary to check the accuracy of these parameters and techniques used in predicting the rupture time. The accuracy level in prediction was decided based on the root-mean-square (RMS) value [53], given by Equation 3.21.

$$RMS = \left[\frac{\sum \left(\ln t_{actual} - \ln t_{predicted}\right)^2}{N} \right]^{1/2} \qquad \text{Equation 3.21}$$

where t_{actual} = Actual time to rupture

$t_{predicted}$ = Predicted time to rupture

N = Number of data points

3.5 Crack-Growth-Rate (CGR) Evaluation

In view of the extreme operating conditions associated with the GEN IV program, identification and subsequent selection of suitable structural materials for heat exchanger constitute an enormous challenge. A combination of monotonic creep and fatigue, resulting from the synergistic effect of high temperature environment and temperature-induced repeated or alternating stress, can adversely influence the mechanical performance of these materials. Thus, the consequence of creep and fatigue interaction (creep-fatigue) must be addressed in the selection of materials prior to the design of high temperature structural components such as heat exchangers. The complex creep-fatigue loading can often be simplified by considering high temperature low-cycle-fatigue (LCF) conditions with a hold time at a constant tensile strain [54, 55]. The fatigue life of a high temperature component under an LCF condition, however, depends not only on the temperature but also on the loading waveform due to the occurrence of time-dependent deformation or creep.

Prior to the CGR testing, the 0.25-inch CT specimens were precracked up to a length of 2 mm (0.078 in.) in the Instron testing equipment (Figure 3.1) at room temperature according to the ASTM Designation E 647-2000 [56] at a load ratio (R = minimum load, P_{min}/maximum load, P_{max}) and a frequency of 0.1 and 1 Hz, respectively. A direct-current-potential-drop (DCPD) technique was used to continuously monitor the crack propagation during both precracking and CGR testing involving the CT specimens. The DCPD method involved passing a constant current of 300 mA through the cracking specimen and detecting the voltage drop across the crack mouth due to the extension of crack length using Johnson's equation [57], given by Equation 3.22.

$$\frac{V_i}{V_o} = \frac{\cosh^{-1}\left[\frac{\cosh(\pi y/W)}{\cos(\pi a_i/W)}\right]}{\cosh^{-1}\left[\frac{\cosh(\pi y/W)}{\cos(\pi a_o/W)}\right]} \qquad \text{Equation 3.22}$$

where V_o and a_o are the initial crack mouth potential and crack length, V_i and a_i are the instantaneous crack mouth potential and crack length, y is half of the distance between the two points for which the crack mouth potential is measured, and W is the specimen width.

A CT specimen, showing the current and potential leads used in crack-growth monitoring, is shown in Figure 3.9. A ceramic-lined split furnace (model 3320), attached to the Instron testing machine, was used to heat the CT specimens to the desired testing temperatures. CGR testing was performed involving precracked CT specimens under a constant ΔK ($K_{max} - K_{min}$) of 25 MPa$\sqrt{m}$ at 600, 700 and 800 ^{o}C. The load range ($\Delta P = P_{max} - P_{min}$) was gradually reduced as the crack length was enhanced to maintain a constant ΔK of 25 MPa$\sqrt{m}$. Initially, testing under cyclic loading (fatigue CGR) was performed using a triangular waveform (constant ΔK-controlled mode) with frequency (f) and R value of 0.33 Hz and 0.1, respectively without any hold time. Subsequently, the creep-fatigue CGR testing was performed at each temperature involving the same CT specimen (initially tested under R and f values of 0.1 and 0.33, respectively) by superimposing hold times of 60, 120, 300, 600 and 1000 seconds on the triangular waveform employed in the fatigue CGR testing at P_{max}. Crack extensions ranging from 0.5 to 0.8 mm between each hold time was selected to monitor the instantaneous crack length as a function of the loading cycle at each tested temperature. A software program [58], provided by the Fracture Technology Associates, Bethlehem, PA, was used to

continuously monitor cracking and record data, leading to the development of crack length versus number of loading cycle plots. Figure 3.10 illustrates the waveform associated with the CGR testing performed under synergistic effect of cyclic loading and variable hold time at P_{max}.

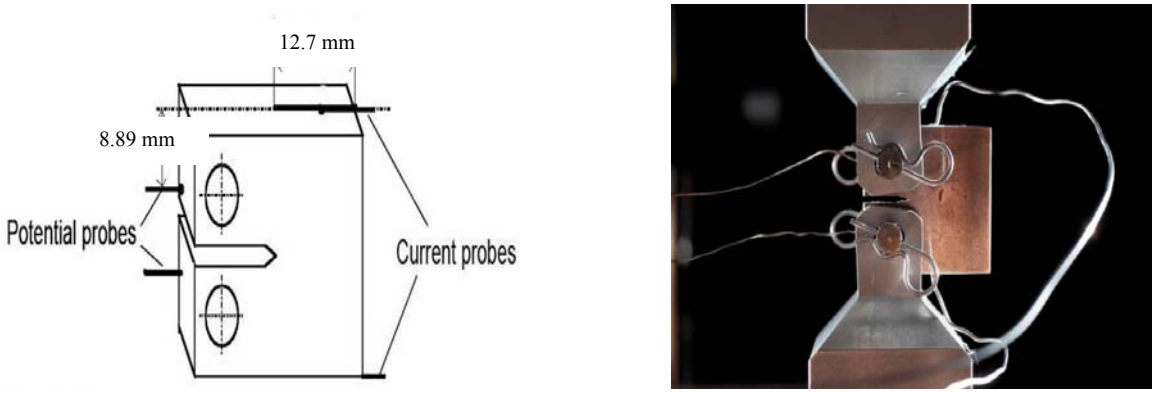

Figure 3.9 Creep-Fatigue Test Setup

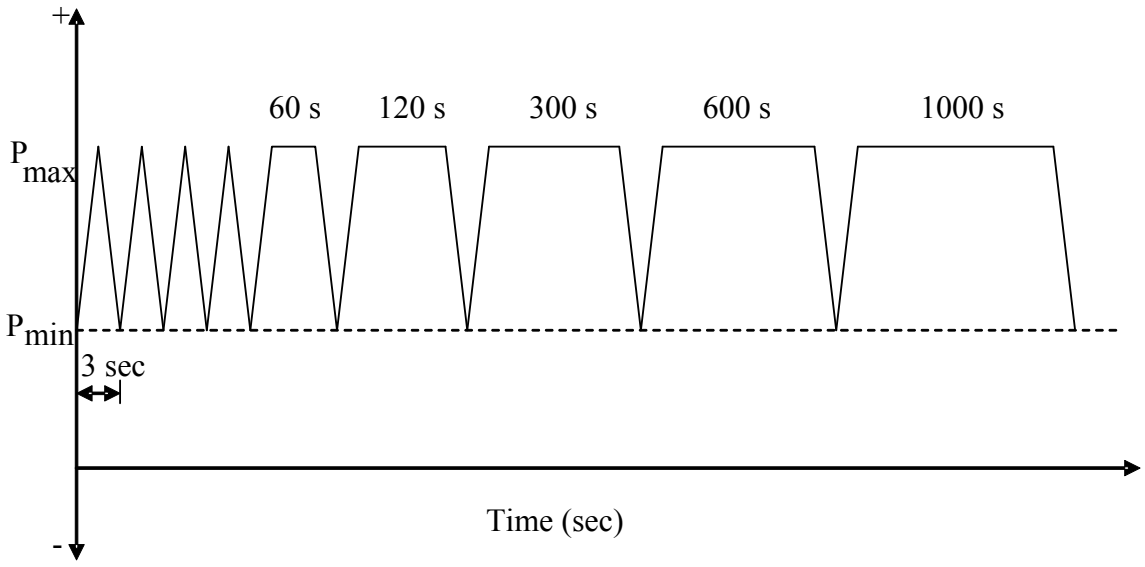

Figure 3.10 Loading Waveform vs. Hold time.

3.6. Microstructural Characterization

The metallographic technique, using an optical microscope, enables the characterization of phases present, their distributions within grains and their sizes that depend on both the chemical composition and the thermal treatment of the test material. The principle of an optical microscope is based on the impingement of a light source perpendicular to the test specimen. The light rays pass through the system of condensing lenses and then shutters up to the half-penetrating mirror. This brings the light rays through the objective to the surface of the specimen. Light rays are reflected off the surface of the sample, which then return to the objective, where they are gathered and focused to form the primary image. This image is then projected to the magnifying system of the eyepiece. The contrast observed under the microscope results from either an inherent difference in intensity or wavelength of the light absorption characteristics of the phases present. It may also be induced by preferential staining or attack of the surface by etching with a chemical reagent.

The test specimens were sectioned, and mounted using standard metallographic technique, followed by polishing and etching to reveal their metallurgical microstructures. The etchant used was Kalling's Reagent, which composed of a mixture of 40 ml of distilled water, 2 grams of cupric chloride ($CuCl_2$), 40 ml of hydrochloric acid and 40 ml of ethanol. The polished and etched specimens were then evaluated for determination of their microstructures in a Leica optical microscope, shown in Figure 3.11. This microscope was capable of resolution of up to 1000X. A digital camera with a resolution of 1 Mega pixel enabled the image capture on a computer screen, utilizing the Leica software.

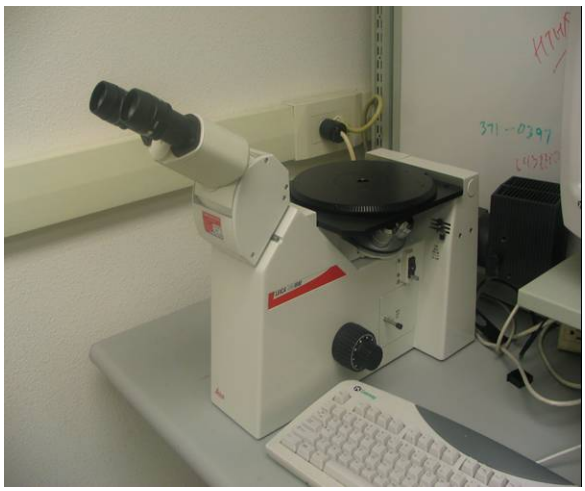

Figure 3.11 Leica Optical Microscope

3.6.1 Grain Size Evaluation

Efforts were made to determine the grain size of the tested materials from their optical micrographs. The ASTM grain size number (G) as well as the grain size (diameter D) will be determined using the 'mean lineal intercept method,' prescribed by the ASTM Designation E 112-1996 [59]. The following steps were used to determine the G and D values.

- First, a template (Figure 3.12) consisting of three concentric circles with a total length of 500 mm was placed over the resultant optical micrograph, and the total number of grain boundary intersections with these test lines was determined.

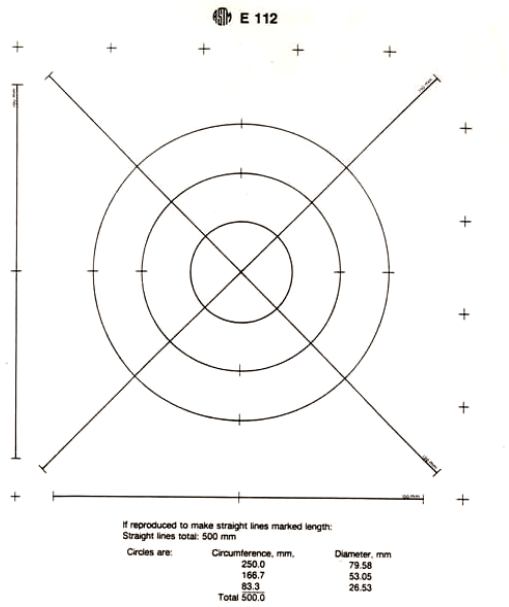

Figure 3.12 Template used in Grain Size Determination

- Then, the mean lineal intercept length ($\bar{L}_L$) was determined by using Equation 3.23.

$$\bar{L}_L = \frac{L_T}{PM} \qquad \text{Equation 3.23}$$

where

L_T = Total length of test lines

P = Total number of grain boundary intersections

M = Magnification of the micrograph

- Next, the value of G was calculated using Equation 3.24

$$.G = -3.2877-6.438\log \bar{L}_L \qquad \text{Equation 3.24}$$

- Finally, the grain diameter (D) was determined using Equations 3.25 and 3.26

$$N = 2^{G-1} \qquad \text{Equation 3.25}$$

$$D = \frac{1}{\sqrt{N}} \qquad \text{Equation 3.26}$$

where

N = Number of grains/sq. mm at a magnification of 1X

D = Grain diameter, mm

3.6.2. Calculation of Volume Fraction and Precipitate Size

The volume fraction and size of second phase particles or precipitates visible under optical microscopy were evaluated using methods of quantitative stereology [60]. In order to measure the volume fraction of precipitates, point count method [60] was used. A (10 x 10) grid consisting of total 100 points was placed over the optical micrograph and the number of points lying within the precipitates was determined. The volume fraction of precipitate was calculated using Equation 3.27.

$$V_v = \frac{n_p}{P} \qquad \text{Equation 3.27}$$

where V_v = volume fraction of precipitate,

n_p= number of points lying within the precipitate, and

P = total number of grid points (=100).

The size of the precipitates was determined using mean linear intercept method [60]. A series of 10 lines of equal lengths at same spacing were placed and the number of points intersecting the precipitates was counted. The counting was performed both in the horizontal and vertical direction to minimize the error due to different aspect ratios of the particles. The precipitate size was determined using Equation 3.28.

$$\bar{L} = \frac{2V_v}{P_L} \qquad \text{Equation 3.28}$$

where $\bar{L}$ = Mean particle size,

V_v = Volume fraction of particles

P_L = number of intersection points per unit length of lines.

3.7 Fractographic Evaluations

The extent and morphology of failure of the tested specimens were determined using a scanning electron microscope (SEM). Analysis of failure in metals and alloys involves identification of the type of failure. The tested specimens were sectioned into 1/2 to 3/4 of an inch in length to accommodate them in the vacuum chamber of the SEM. Failures can usually be classified into two common types including ductile and brittle. Dimpled microstructure is a characteristic of ductile failure. Brittle failure can be of two types; intergranular and transgranular. An intergranular brittle failure is characterized by crack propagation along the grain boundaries while a transgranular failure is characterized by crack propagation across the grains.

In SEM evaluations, electrons from a metal filament are collected and focused, just like light waves, into a narrow beam. The beam scans across the subject, synchronized with a spot on a computer screen. Electrons scattered from the subject are detected and can create a current, the strength of which makes the spot on the computer brighter or darker. This current can create a photograph-like image with an exceptional depth of field. Magnifications of several thousands are possible to achieve. A JEOL-5610 SEM, shown in Figure 3.13, and capable of resolution of up to 50 nm at magnifications of up to 100,000 times was used in this study. The manual stage of this SEM unit can accommodate four 1 cm diameter samples or one sample with up to 3.2 cm diameter.

Figure 3.13 Scanning Electron Microscope

3.8 Transmission Electron Microscopic Study

Transmission electron microscopic (TEM) studies were conducted to characterize dislocations and precipitates of the tested creep specimens using a Tecnai G² F30 S-TWIN TEM (Figure 3.14). This equipment operates at 300kV acceleration voltage that allows a point-to-point resolution of 0.2 nanometer. Magnifications up to 1,000,000 times can be achieved with this TEM. This system is fully loaded including HAADF (high angle annular dark field) detector, EDX (X-ray energy disperse spectrometry), and GIF (Gatan Image Filter). Multiple samples were prepared from tested specimens of interest to obtain valid TEM micrographs. The sample preparation technique is described in details in the next subsection.

Figure 3.14 Transmission Electron Microscope

3.8.1 TEM Sample Preparation

Sample preparation for the TEM study involved a state-of-art technique. To ensure electron transparency of the sample by the TEM method, the specimen thickness was maintained between 50-100 nanometers. This was achieved through a series of operations [61-64]. Initially, multiple circular disc-shaped samples were cut from the gage length of a tested creep specimen up to a thickness of 500–700µm, using a precision cutter. These sectioned samples were mechanically ground (Figure 3.15) to about 100–150 µm using a grinder in the TEM laboratory. This process involved rough-grinding and fine-polishing. Specimen thickness was monitored periodically during this process. The samples were punched into 3mm diameter discs using a disc puncher (Figure 3.16). Finally, electro-

polishing was done to attain the desired specimen thickness. A twin-jet TenuPol-5 electro polisher (Figure 3.17) was used for this purpose. The electro-polishing process involved removal of material from the sample surface as well as surface finish prior to the TEM observation. The electrolyte used composed of 5% perchloric acid ($HClO_4$) in methanol (CH_3OH) under an applied potential of 50V and a pump flow rate of 12 at a temperature of -3°C [61]. Care was taken to control the flow of electrolyte to prevent the formation of anodic film that could cause etching of the specimen rather than polishing [61-64].

Figure 3.15 Grinding Accessories

Figure 3.16 Disc Puncher

Figure 3.17 TenuPol-5 Electro-polisher

CHAPTER 4

RESULTS

This chapter presents the results of all experimental work identified in the proposed test matrices, shown in Table 1.1. These data include the results of tensile testing, fracture toughness evaluation, creep and stress rupture testing, crack growth study under creep-fatigue conditions, microstructural characterization using optical microscopy and transmission electron microscopy (TEM), and fractographic evaluation by scanning electron microscopy (SEM).

4.1 Microstructural Evaluation of As-Received Material

Figure 4.1 shows the optical and TEM micrographs of the as-received samples of Alloy 230. The optical micrograph, shown in Figure 4.1(a), revealed a fully austenitic microstructure with an average grain size of 50 ± 4 μm that correspond to an ASTM grain size number of 5. There were no evidence of precipitation within the grain and grain boundaries, as expected for a fully annealed material. The TEM image, shown in Figure 4.1(b), shows dislocation alignment in a particular direction, which is a characteristic of dislocation climb phenomenon that occurred due to recovery during solution annealing treatment. The EDX analysis revealed common elements such as Ni, Cr, W, Mo, Fe and C that are present in Alloy 230, as shown in Figure 4.1(c).

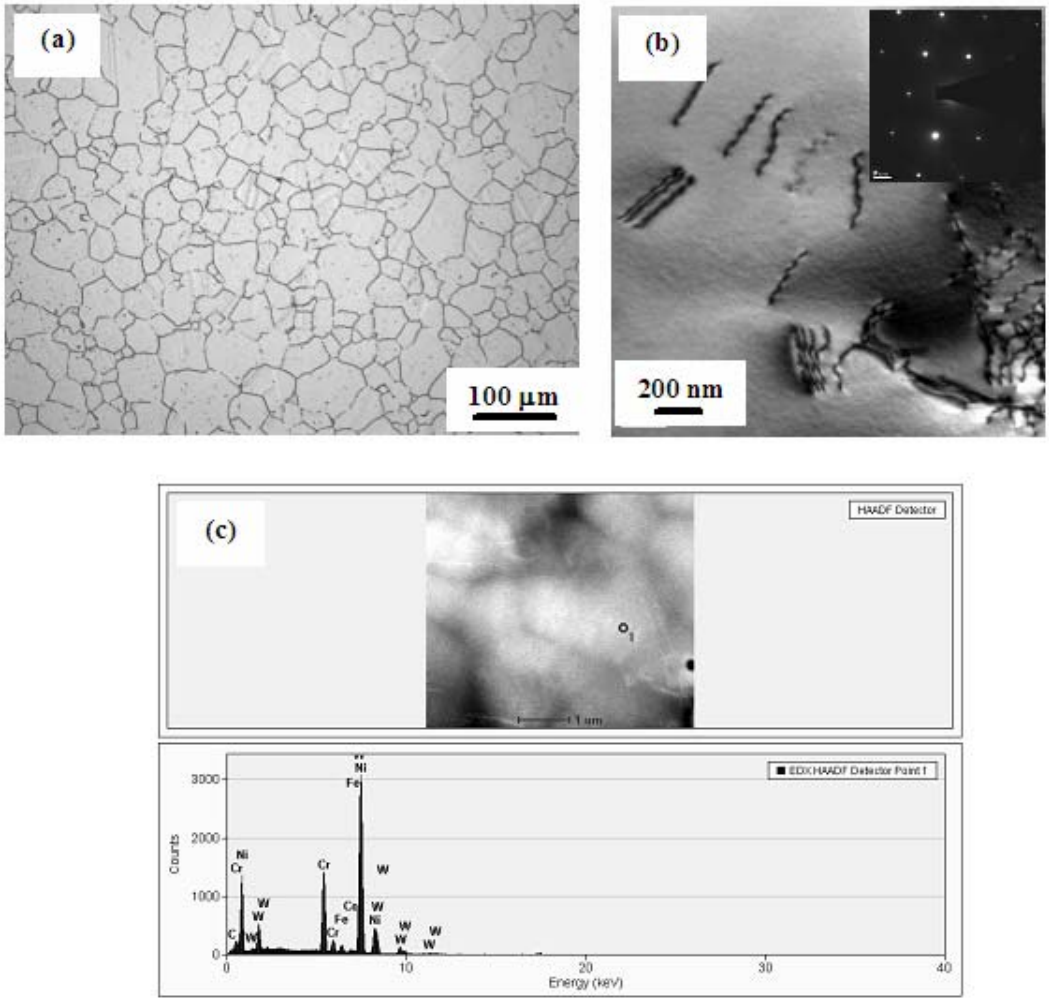

Figure 4.1 (a) Optical Micrograph; (b) TEM Image; and (c) EDX Spectra of As-Received Alloy 230

4.2 Results of Tensile Testing

Tensile testing was performed at a strain rate of 0.001 sec^{-1} to generate a baseline mechanical properties data including the yield strength (YS), ultimate tensile strength (UTS), percent elongation (%El) and percent reduction in area (%RA) of Alloy 230 at temperatures ranging from ambient to 950 °C. The magnitudes of stress applied in creep testing were calculated from the YS values determined at different temperatures. The results of tensile testing are illustrated in Figure 4.2 in the form of superimposed

engineering stress versus engineering strain (s-e) diagram as a function of the testing temperature. It is interesting to note that serrations of different heights were observed in the s-e diagrams at 300 and 500 °C. Formation of serrations at some specific temperatures could be the result of repeated hardening and softening due to the diffusion of solute elements within the matrix and near grain boundaries, thus causing reduced dislocation mobility and plastic strain. Such phenomenon is known as dynamic strain ageing, which is beyond the scope of the current investigation. The overall tensile data, shown in Table 4.1, revealed that both YS and UTS were gradually reduced with increasing temperature, as expected. Simultaneously, the ductility in terms of %El and %RA was gradually enhanced as the testing temperature was increased.

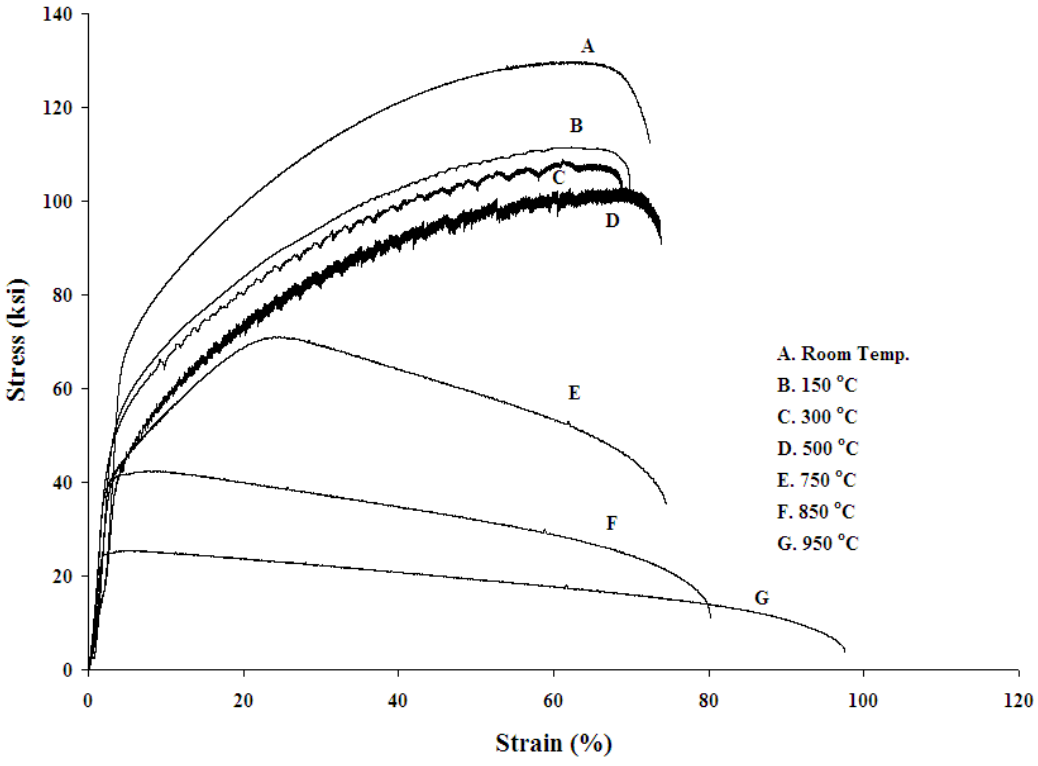

Figure 4.2 s-e Diagrams vs. Temperature

Table 4.1 Tensile Properties of Alloy 230

Temperature (^{o}C)	YS, ksi (MPa)	UTS, ksi (MPa)	%El	%RA
Room Temperature	63 (434)	130 (896)	15.0	40.6
150	46 (317)	111 (765)	15.8	42.9
300	41 (283)	109 (751)	16.5	44.0
500	40 (276)	103 (710)	17.3	53.4
750	40 (276)	71 (489)	18.5	61.4
850	37 (255)	43 (296)	20.0	76.0
950	21 (145)	25 (172)	23.0	83.7

4.3. Results of J_{1C} Testing

J_{1C} testing was performed to develop a baseline fracture toughness data as a function of temperature. However, testing could not be performed at elevated temperatures due to combined equipment and funding constraint. Figure 4.3 shows a Load versus LLD curve at ambient temperature. A plot of J-integral value with corresponding increment in crack length is also illustrated in Figure 4.4. Both figures were automatically generated by using a J_{1C} fracture toughness software [refs]. The conditional J_Q value was calculated to be 98.27 KJ/m^2, which satisfied the validation criteria prescribed by the ASTM Designation E 813-1989 [42]. Thus, the calculated J_Q value was taken as J_{1C}, which was subsequently converted into K_{IC} value using Equation 3.7. A K_{IC} value of 137 MPa$\sqrt{m}$ was estimated based on this conversion, which was lower than those of Alloys 617 and 276 [6, 65]. Thus, the resistance of Alloy 230 to fracture in the presence of a pre-existing crack appears to be somewhat lower than that of other Ni-base alloys considered for the NGNP application.

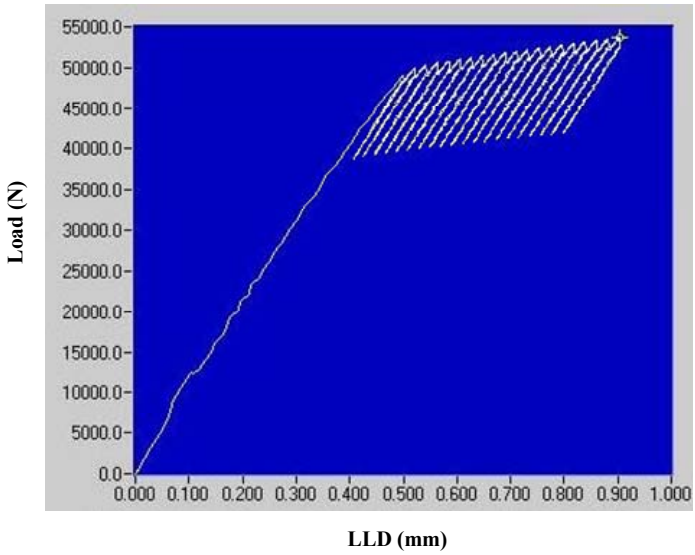

Figure 4.3 Load vs. LLD

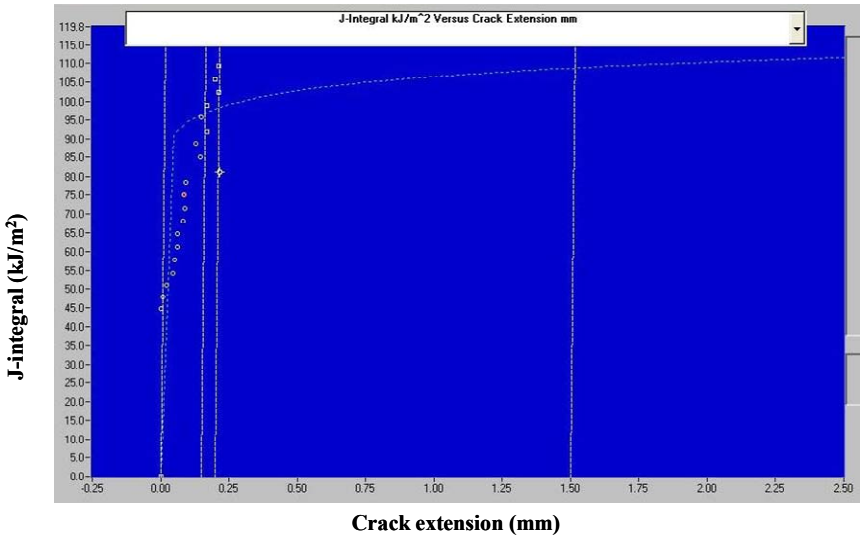

Figure 4.4 J-integral vs. Crack Extension

4.4 Results of Creep Testing

Figures 4.5 and 4.6 show the creep curves of Alloy 230 generated under applied stresses of 10 and 25% of its YS values at 750, 850 and 950 ^{o}C. As shown in Figure 4.5, this alloy exhibited two-stage (primary and secondary) creep deformation under applied stresses equivalent to its 0.10YS values at three temperatures. The total strain did not exceed 1% at all three tested temperatures even after 1000 hours of loading. Creep strain not exceeding 1% following 1000 hours of sustained loading has been considered to be the maximum allowable plastic strain for creep-resistant materials [66]. Using such an acceptance criterion, it can easily be stated that Alloy 230 would be a creep-resistant material at temperatures ranging between 750 and 950 ^{o}C when loaded to stresses up to its 0.10YS values at temperatures within this range. It is, however, interesting to note that the steady-state creep rate and the total creep strain after 1000 hours of testing was slightly higher at 750 ^{o}C compared to those at 850 ^{o}C. Such anomaly in creep deformation could possibly be attributed to microstructural changes resulting from the combined effect of temperature and applied stress. Table 4.2 shows the overall creep data of this alloy following 1000 hours of loading at the tested temperatures.

At higher applied stress levels (0.25YS values), this alloy showed enhanced creep deformation at 850 and 950 ^{o}C. At these temperatures, all three stages (primary, secondary and tertiary stages) of creep deformations were observed. The onset of tertiary deformation occurred following 200 hours of testing at 950 ^{o}C, as illustrated in Figure 4.6. Further, the extent of total creep strain was increased beyond 1% at 850 and 950 ^{o}C under applied stresses equivalent to the material's 0.25YS values. Thus, Alloy 230 failed to satisfy the acceptance criterion of maximum creep strain of 1% at these temperatures

when loaded under applied stresses corresponding to its 0.25YS values. However, at 750 ^{o}C, this alloy exhibited a maximum creep strain (0.45) that fell within the acceptable level under an applied stress equivalent to its 0.25YS value. The overall results of creep testing are given in Table 4.2.

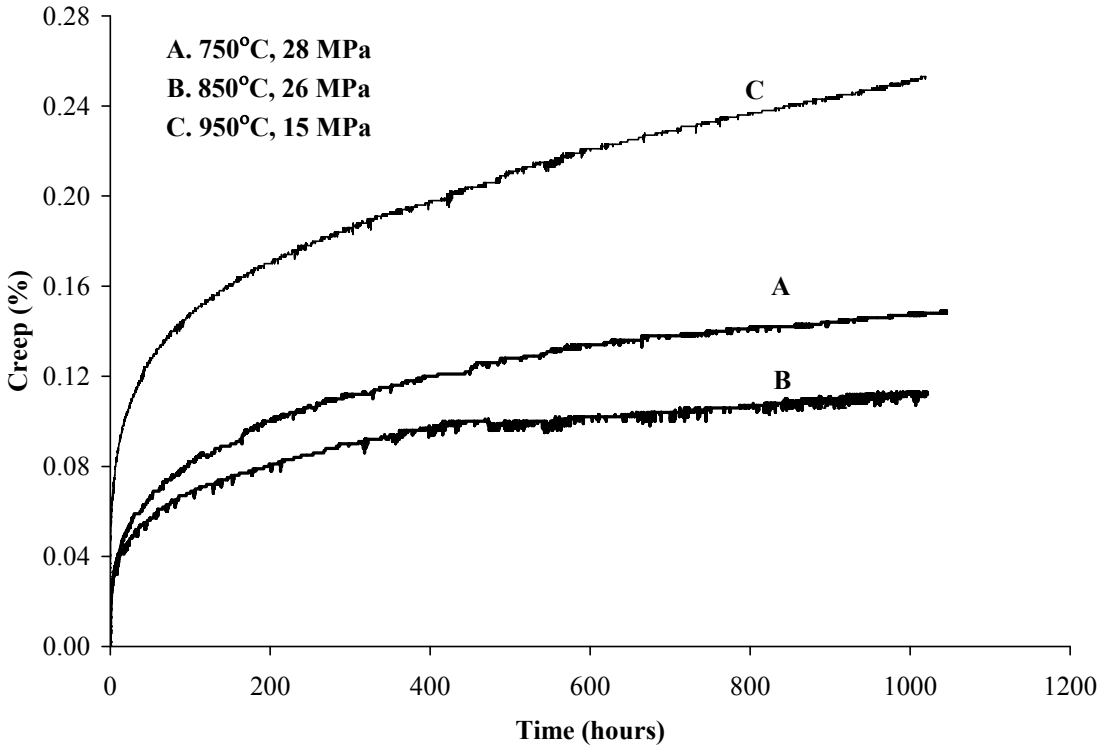

Figure 4.5 Creep Curves of Alloy 230 vs.Temperature under 0.10YS Stress Values

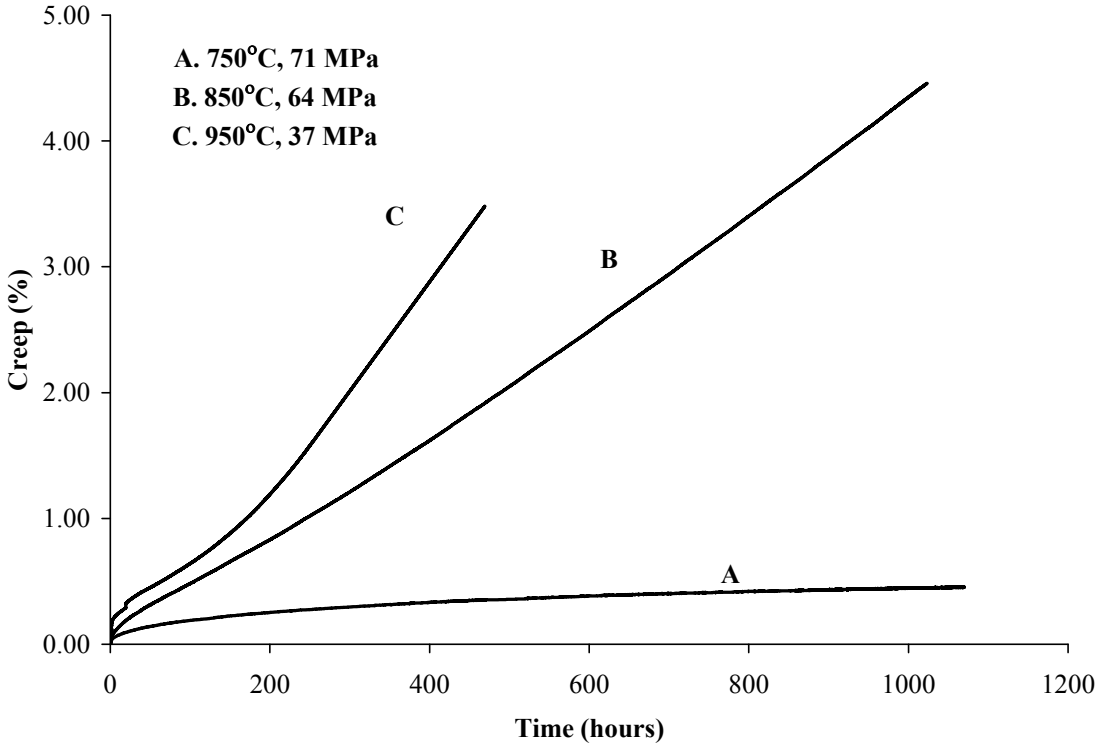

Figure 4.6 Creep Curves of Alloy 230 vs. Temperature under 0.25YS Values

Table 4.2 Results of Creep Testing

Temperature (°C)	Applied Stress (MPa)	Steady State Creep Rate (% creep/hour)	Total Creep Strain after 1000 hours testing
750	28	3.96E-05	0.147
	71	1.71E-04	0.446
850	26	2.57E-05	0.112
	64	3.47E-03	4.352
950	15	8.32E-05	0.252
	37	3.72E-03	3.482*

* Testing was discontinued after 470 hours due to unstable plastic deformation

Microstructural characterization was performed using both optical microscopy and TEM to develop a basic understanding of creep deformation of Alloy 230. Parameters

including grain size, dislocation structures, and size and volume fraction of precipitates formed during creep deformation were analyzed. The optical micrographs of specimens tested at 750, 850 and 950 ^{o}C under applied stresses corresponding to 10 and 25% of the material's YS values are shown in Figures 4.7 and 4.8, respectively. Precipitates of secondary particles, both intra- and intergranular, were observed in these micrographs. However, the formation of intergranular precipitates was more pronounced at 750 and 850 ^{o}C, showing very thick layers along grain boundaries irrespective of the applied stress levels.

Characterization of these precipitates were performed by TEM, verifying the formation of superstructures having a composition of type Ni_2 (Cr, W) based on the analyses of the EDX spectra and indexing of the electron diffraction pattern, as shown in Figure 4.9. The EDX data showed the presence of Cr, Ni and W as major elements in the precipitate, but no carbon. The absence of carbon confirmed that these precipitates were not carbides. The formation of orthorhombic Ni_2 (Cr, W) superstructures due to long-term exposure of Ni-base alloys at temperatures above 500 ^{o}C has been reported in the open literature [67-69]. The Ni_2 (Cr, W) superstructures are known to be sufficiently coherent with the matrix, and have long-range ordering, as seen in the diffraction pattern presented in Figure 4.9. However, their size and volume fraction varied with the temperature and the applied stress level, as shown in Table 4.3. The calculated values of the average size of the austenitic grains have also been included in this table, showing insignificant variation even under different experimental conditions. Annealing twins were also observed in all micrographs.

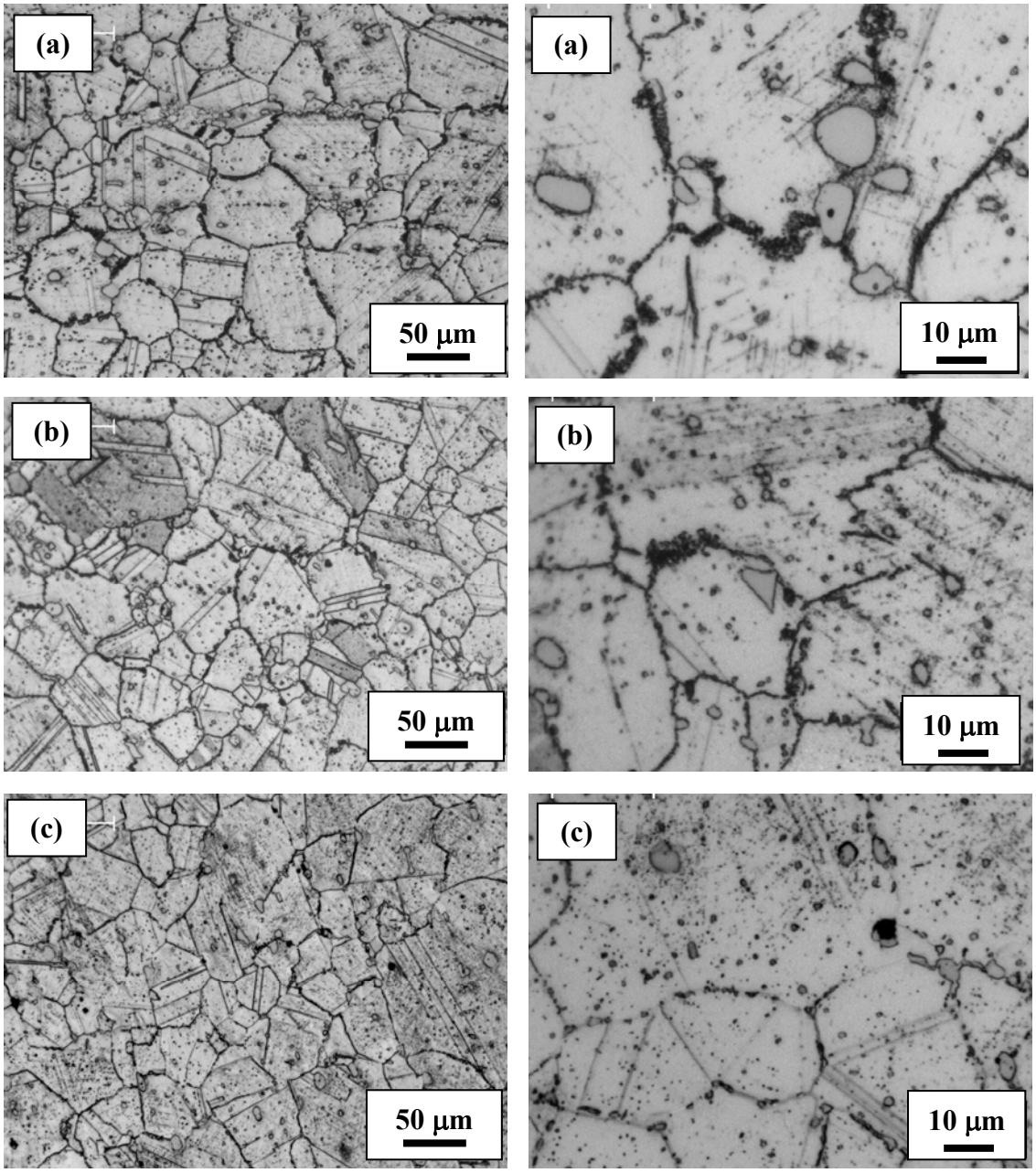

Figure 4.7 Optical Micrographs of Samples Tested at (a) 750 ^{o}C (b) 850 ^{o}C, and (c) 950 ^{o}C under Applied Stresses of 0.10YS

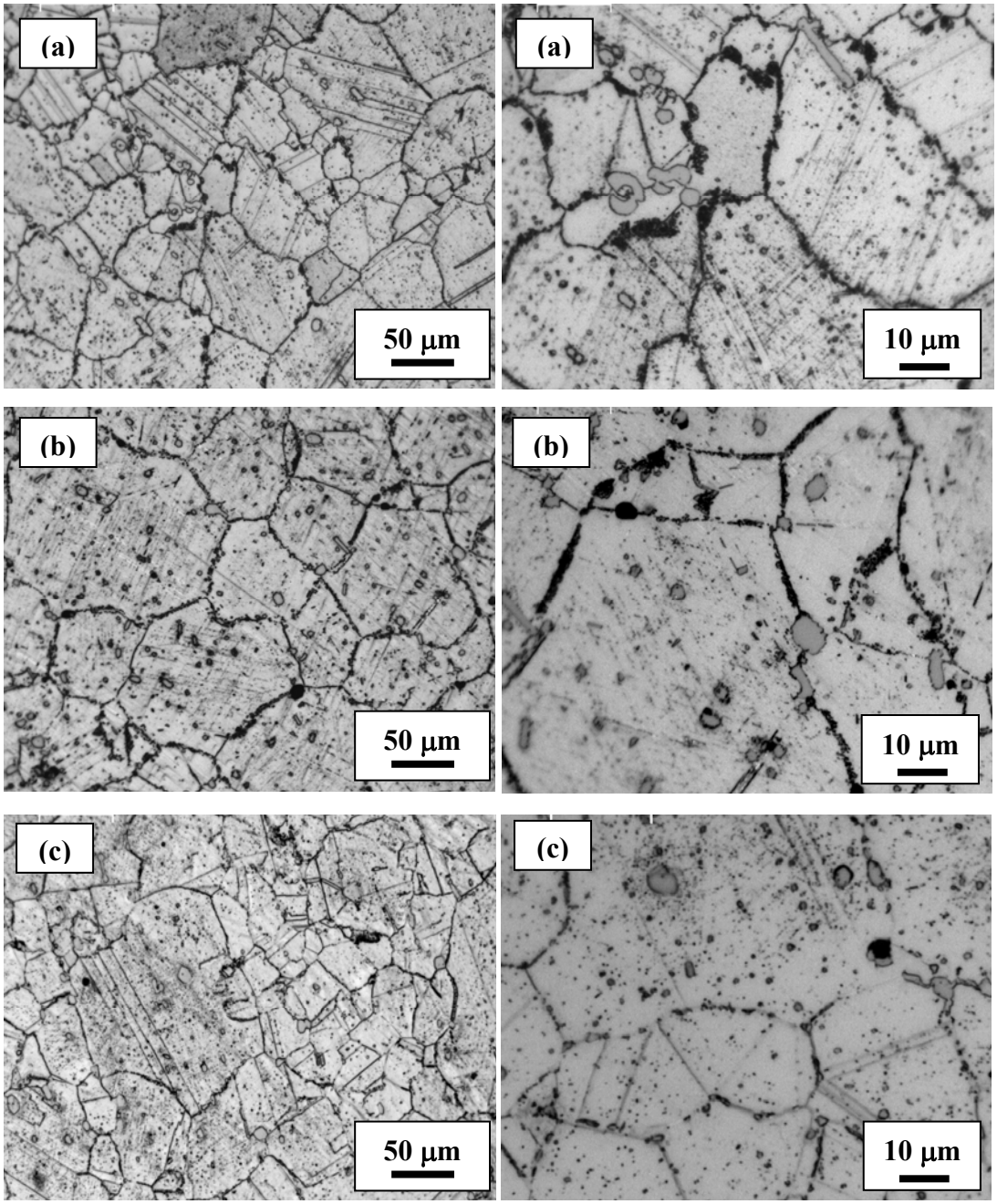

Figure 4.8 Optical Micrographs of Samples Tested at (a) 750 ^{o}C (b) 850 ^{o}C, and (c) 950 ^{o}C under Applied Stresses of 0.25YS

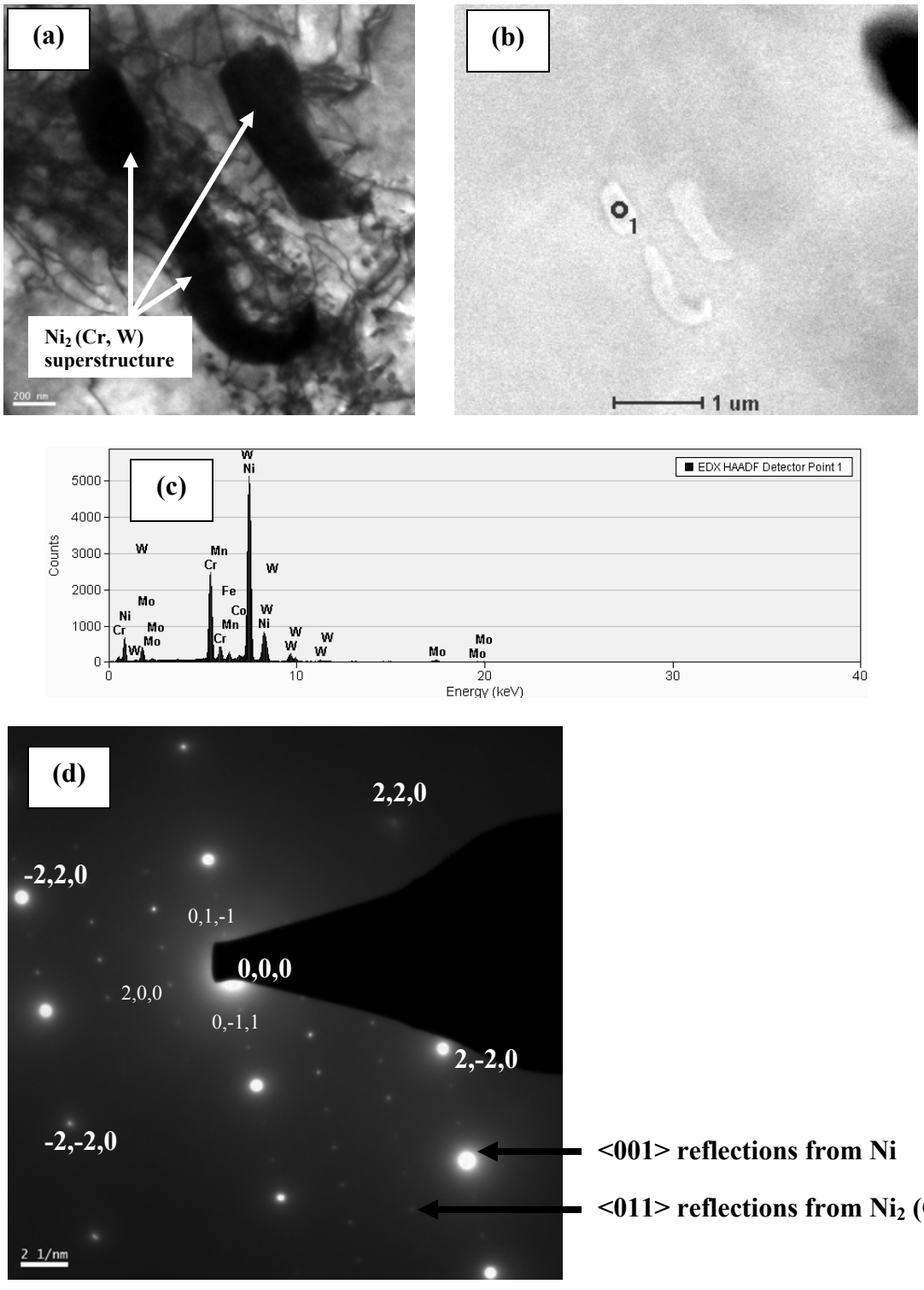

Figure 4.9 Characterization of Ni_2 (Cr, W) Superstructures using (a) TEM (b) STEM (c) EDX Analysis, and (d) Indexed Electron Diffraction Pattern

Table 4.3 Austenitic Grain Size and Characteristics of Ni_2 (Cr, W) Superstructure

Temperature (^oC)	Applied Stress (MPa)	Grain Size (μm)	Volume fraction of Ni_2 (Cr,W) superstructures	Size of Ni_2 (Cr,W) superstructures (μm)
750 ^oC	10%YS	96	0.09	13.8
	25%YS	98	0.06	9.9
850 ^oC	10%YS	97	0.09	7.4
	25%YS	102	0.07	3.4
950 ^oC	10%YS	103	0.03	2.9
	25%YS	105	0.01	1.0

The relatively lower steady-state creep rate and total strain, observed in Alloy 230 at 850 ^oC, compared to those at 750 ^oC, could possibly be explained by a precipitation hardening mechanism that would depend on the size of the resultant precipitates. Evaluation of the data shown in Table 4.3, and the optical micrographs (Figures 4.7 and 4.8) suggests that the size of Ni_2 (Cr, W) superstructures formed at 750 ^oC was much larger than those developed at higher temperatures. Further, the volume fraction of these superstructures was gradually reduced with increasing temperature and applied stress level. The formation of second phase particles, such as superstructures, can impede the dislocation motion through the austenitic grains and past the grain boundaries, thus causing reduced plastic strain. Since the superstructures formed at 750 ^oC were relatively larger in size and greater in volume fraction, dislocations could move through the metal lattice by bowing out around these second phase particles, thus resulting in relatively greater plastic strain than that developed in the presence of finer secondary particles formed at higher temperatures around dislocations.

As the size of these second phase particles became smaller at a relatively higher temperature (850 ^oC), the dislocations would need greater driving forces to cut through

the metal lattice since these finer precipitates would exert significant resistance to plastic deformation by either minimizing or preventing dislocation motion. As a result of such reduced dislocation mobility, the plastic strain would also be reduced, as indicated by the lower creep strain observed in this alloy under an applied stress of 0.10YS at 850 ^{o}C.

Precipitates of different types, such as Cr-rich $Cr_{23}C_6$ ($M_{23}C_6$ type) and Ni-rich Ni_3W_3C (M_6C type) can also be formed at higher temperatures. However, under a greater loading constraint (0.25YS level), the formation of these types of precipitates would not be able to prevent or reduce the dislocation motion, thus causing accelerated creep deformation. Such a phenomenon could possibly account for enhanced total creep strain and steady-state creep rate under higher applied stress levels at elevated temperatures tested in this investigation. Figure 4.10 illustrates the STEM images and the corresponding EDX spectra of a specimen tested under an applied stress equivalent to the material's 0.10YS value at 950 ^{o}C. All three types of second phase particles including Ni_2 (Cr, W), Ni_3W_3C and $Cr_{23}C_6$ formed under this experimental condition are evident in this figure. These results are consistent with the observations made by other investigators involving Ni-base alloys [24-25, 67-69].

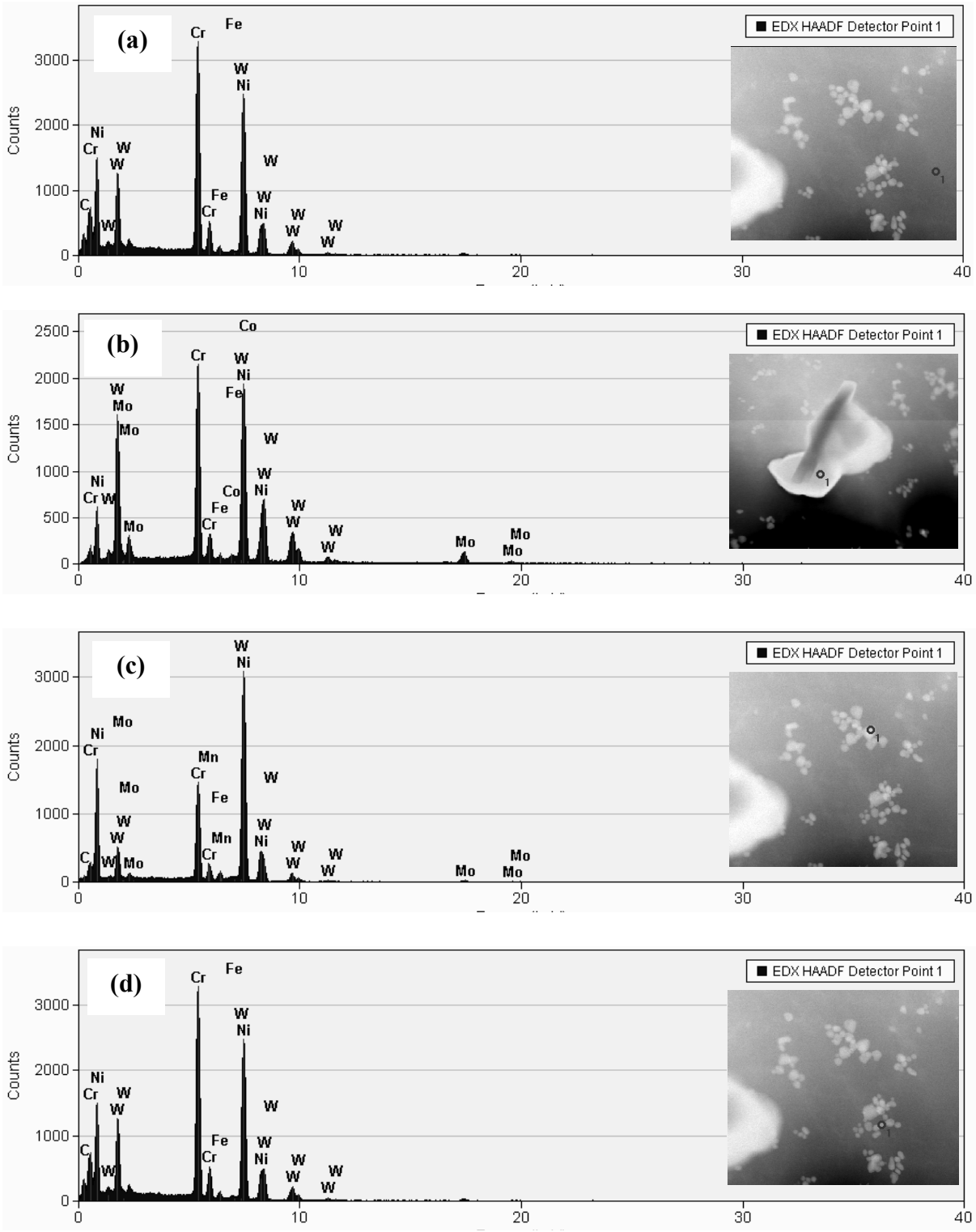

Figure 4.10 STEM images and corresponding EDX analysis of (a) Alloy 230 matrix (b) Ni_2 (Cr, W) superstructure (c) Ni-rich Ni_3W_3C carbides (d) Cr-rich $Cr_{23}C_6$ carbides

The dislocation structure changed depending on the temperature and stress. Figure 4.11 shows the dislocation network in Alloy 230 seen at 750, 850 and 950 ^{o}C, respectively for an applied stress of 0.10YS corresponding to the test temperature. At 750 ^{o}C, the TEM image shows random distribution of dislocations, as shown in Figure 4.11 (a). At a higher temperature of 850 ^{o}C, the dislocations align themselves along the stress axis, as indicated by Figure 4.11 (b). Complete re-arrangement of dislocation and subgrain formation is seen when the temperature is raised to 950 ^{o}C. As the applied stress is increased to 0.25YS, the dislocations now form complete subgrain structure. In addition to the subgrain, newly recrystallized grains and very fine microcracks are seen along the grain boundary, as indicated in Figure 4.12 (a) and (b). Hence, the material reaches the unstable tertiary region of creep at a higher stress of 0.25YS and 950 ^{o}C. In a nutshell, it can be said that the plastic flow resulting in softening during creep is controlled by dislocation glide, subgrain formation and recrystallization, while the strain hardening occurs due to obstructions to the dislocation motion by second phase particles of Ni_2 (Cr,W) superstructures, Ni_3W_3C and $Cr_{23}C_6$ precipitates. The amount of creep strain and the steady state creep rate is controlled by the morphology (size and volume fraction) of these precipitates.

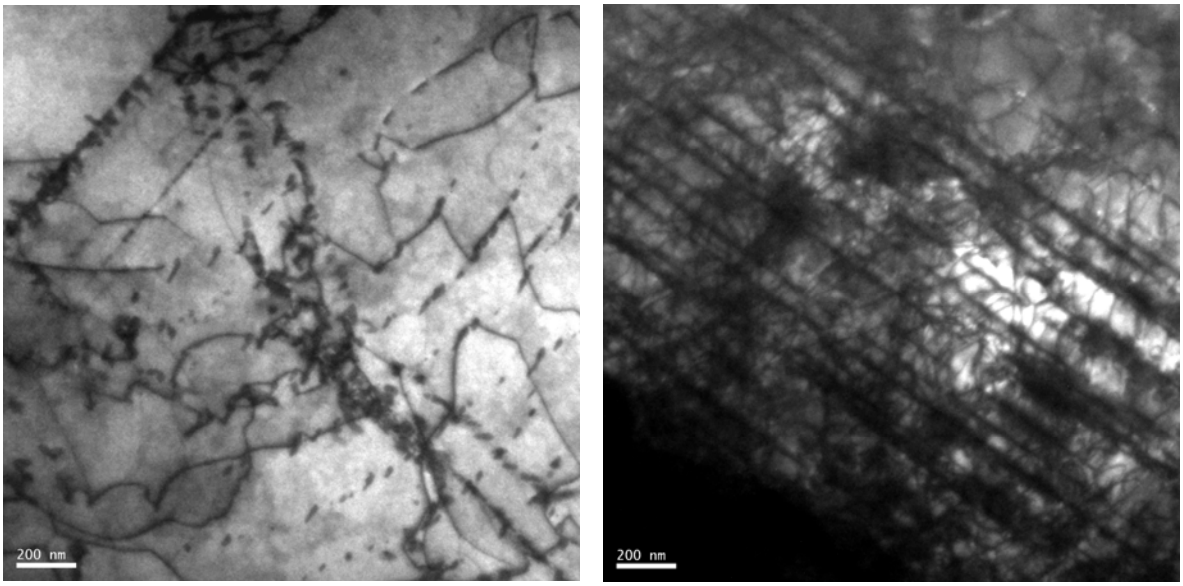

(a) (b)

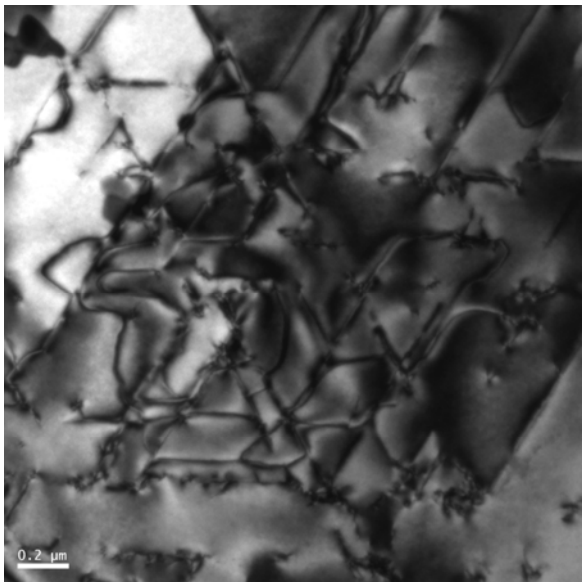

(c)

Figure 4.11 Dislocation structures of creep tested samples at (a) 750 ^{o}C (b) 850 ^{o}C and (c) 950 ^{o}C for an applied stress of 0.10YS

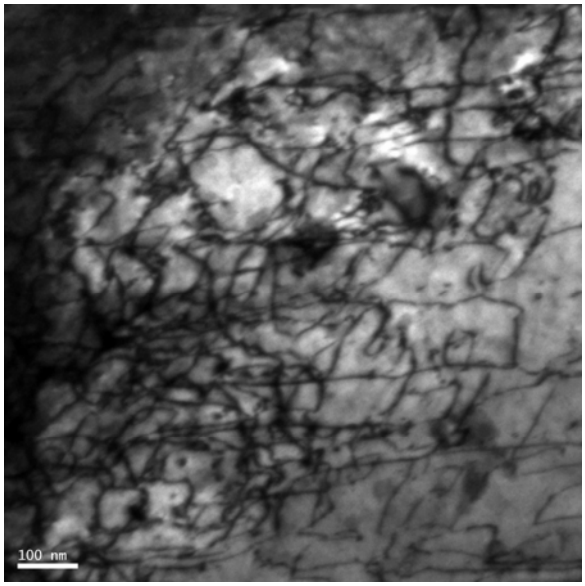

\ (a)

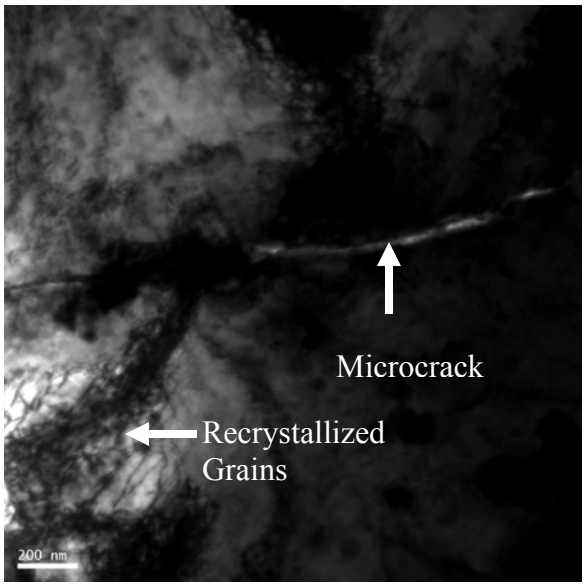

(b)

Figure 4.12 TEM image of Alloy 230 creep tested at 950 ^{o}C and 0.25YS showing (a) dislocation structure (b) microcrack at grain boundary

4.4.1 Activation Energy Evaluation

The activation energy (Q) for creep deformation of Alloy 230 was estimated by using Equations 3.10 and 3.12. Method 1 of Q calculation, using Equation 3.10, was based on the plot of natural logarithm of steady-state creep rate (ϵ_s^o) versus reciprocal of the testing temperature (T). A linear relationship was observed, as shown in Figure 4.13, from which the Q value was calculated using the negative slope for two levels of applied stresses. Q values of 195 and 90 kJ/mole.K, respectively were determined corresponding to applied stresses equivalent to the material's 0.10YS and 0.25YS values. The Q values, obtained by using Equation 3.12, were 110 and 97 kJ/mole.K, respectively under similar levels of applied stress. Even though literature data on Q for Alloy 230 do not exist, values ranging from 300 to 3000 kJ/mole.K have been cited [66, 70] for creep deformation of Ni-base alloys.

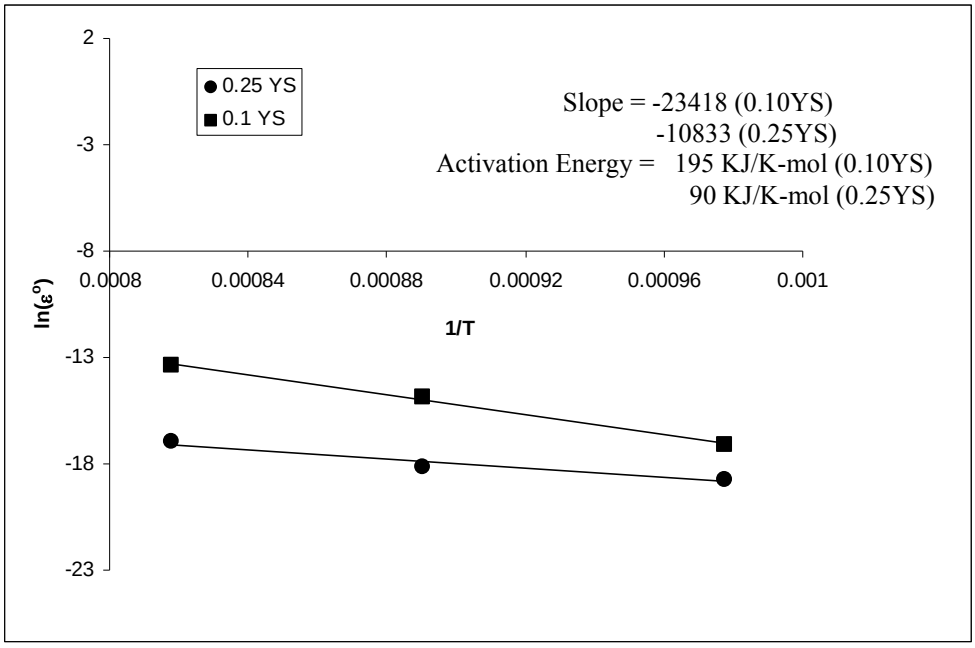

Figure 4.13 ln (ϵ_s^o) vs. 1/T

4.5 Results of Stress Rupture Testing

Stress rupture testing was performed at stress levels of 20, 25 and 30 ksi at 750, 800 and 850 ^{o}C. Efforts were made to determine the different stress rupture parameters including the Larson-Miller Parameter (LMP), Orr-Sherby-Dorn Parameter (θ) and Manson-Hafred Parameter [$f(\sigma)$]. Figures 4.14, 4.15 and 4.16 show the graphical representations for determination of these three parameters using Equations 3.13, 3.14 and 3.15, respectively. As expected, the rupture time was reduced with increasing temperature at higher applied stresses. The estimated values of these three parameters are given in Table 4.4 as functions of temperature and applied stress.

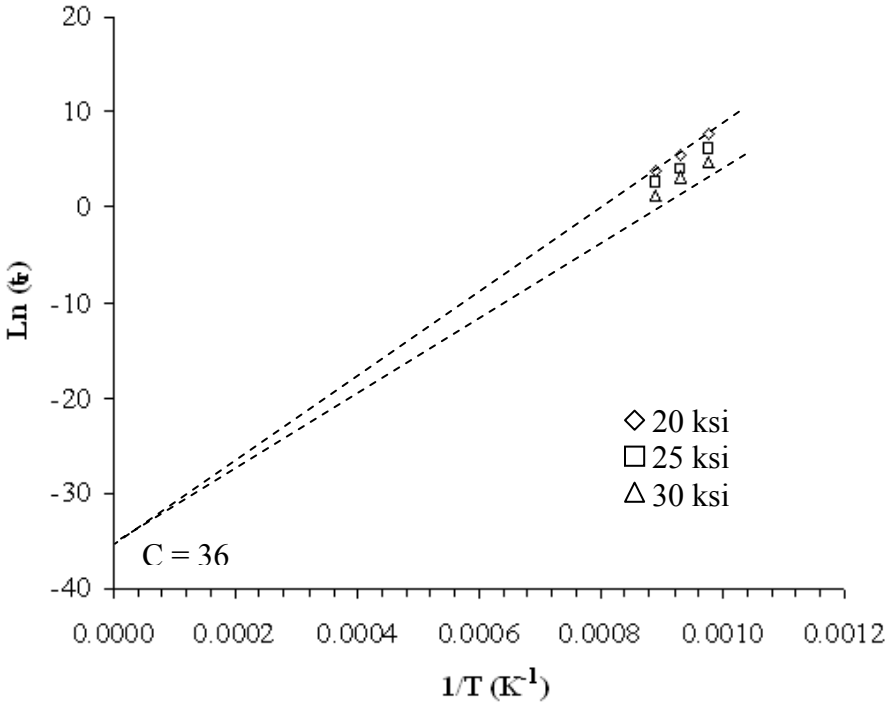

Figure 4.14 Plots for Larson-Miller Parameter Determination

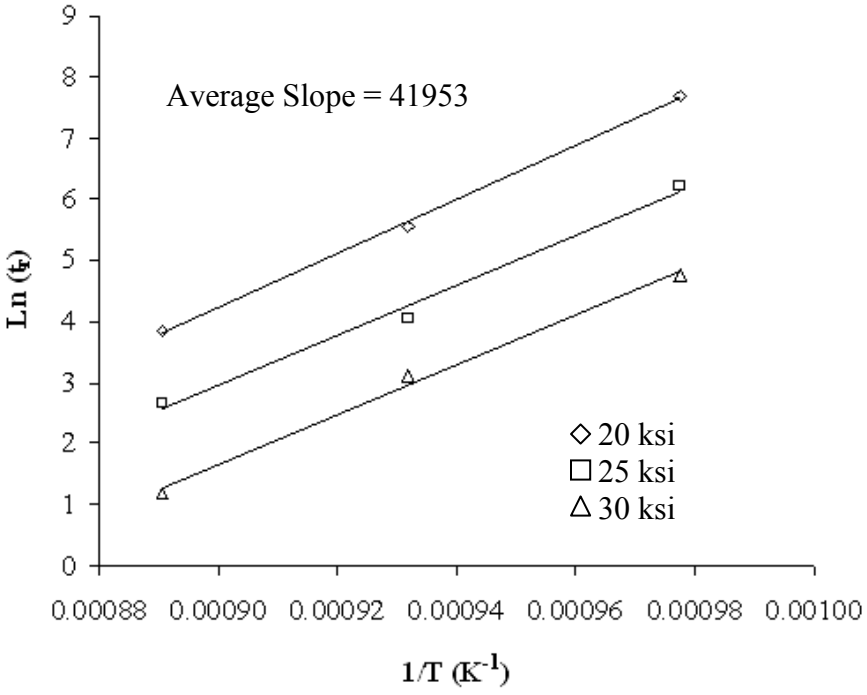

Figure 4.15 Plots for Orr-Sherby-Dorn Parameter Determination

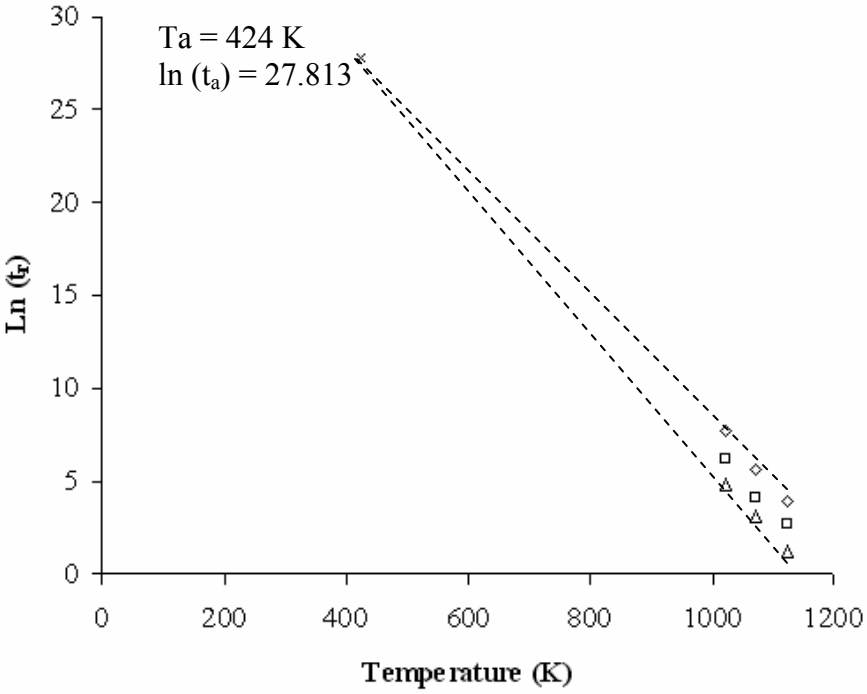

Figure 4.16 Plots for Manson-Hafred Parameter Determination

Table 4.4 Stress Rupture Testing Parameters

Temperature (^{o}C)	Stress (ksi)	Larson-Miller Parameter (P)	Orr-Sherby-Dorn Parameter (θ)	Manson-Hafred Parameter [f(σ)]
750	20	43665	-35.40	-0.0333
	25	42160	-36.87	-0.0361
	30	40685	-38.31	-0.0385
800	20	43526	-32.53	-0.0343
	25	41918	-34.03	-0.0366
	30	40888	-34.99	-0.0381
850	20	43629	-32.57	-0.0343
	25	42295	-33.76	-0.0360
	30	40657	-35.22	-0.0381

The value of Larson-Miller Constant (C) was estimated to be 36 that falls within an acceptable range of 20 to 46 for conventional stress-rupture analysis. The average value of the slope in the OSD analysis was found to be 41953. Using backward interpolation, the coordinates (T_a, ln t_a) for the MH analysis were estimated to be 424 and 27.813, respectively. As mentioned in section 3.4.3, efforts were also made to draw master plots for all three parameters that are shown in Figures 4.17, 4.18 and 4.19 for LM parameter, OSD parameter and MH parameter, respectively. Of all these master plots, the LM plot showed the highest correlation coefficient (R^2) of 0.998. As defined in section 3.4.3, R^2 is a measure of how well the data fits the regression model, with $R^2 = 1$ being a perfect fit, and $R^2 = 0$ being no correlation. The mathematical expression for R^2 is given by Equation 3.20 in Chapter 3. The OSD master plot exhibited the lowest value of R^2 (0.385), and hence a considerable risk may be expected in such extrapolation. The MH master plot, however, had an acceptable correlation coefficient of 0.963.

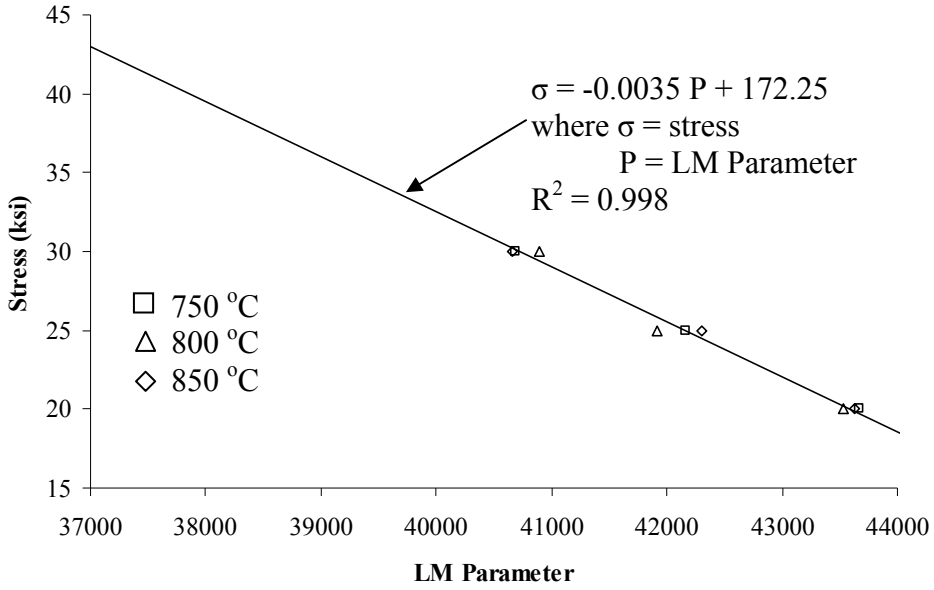

Figure 4.17 Master Plot for LM parameter

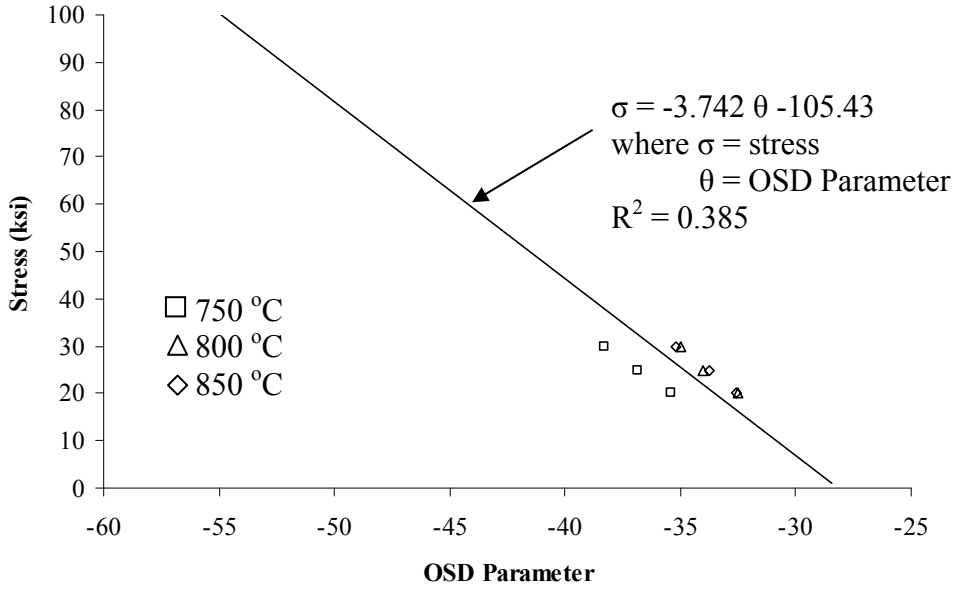

Figure 4.18 Master Plot for OSD parameter

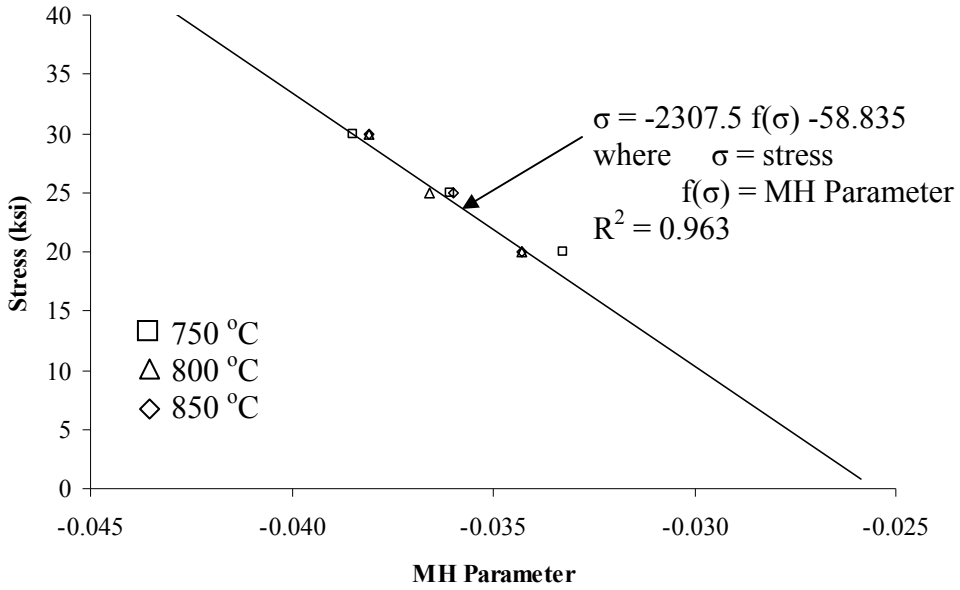

Figure 4.18 Master Plot for MH parameter

Tables 4.5, 4.6 and 4.7 present the predicted rupture times at 750, 800 and 850 ^{o}C under applied stresses of 20, 25 and 30 ksi, which were calculated using the C value, the slope and the coordinates (T_a, ln t_a) estimated from the LM analysis, the OSD analysis and the MH analysis, respectively. The data presented in these tables indicate that among the three parametric extrapolations, the LM and OSD analyses showed the least Root Mean Square (RMS) value of 0.13. The RMS value is a frequently-used measure of the differences between values predicted by a model or an estimator and the values actually observed from the thing being modeled or estimated. The mathematical expression of RMS value is given in Equation 3.21, in Chapter 3. However, if the master plots are considered, the LM master plot had a greater R^2 value of 0.998 compared to a R^2 value of 0.385 in the OSD plot. The OSD analysis might have resulted in a good prediction within the current testing conditions but significant errors may result if extrapolation is done

beyond the current temperature range of 750 to 850 ^{o}C. The MH analysis showed the largest amount of error in rupture time prediction with an RMS value of 0.19. Thus, based on the overall analyses, it may be concluded that of all parametric extrapolation techniques, LM analysis could provide the best estimate of rupture time.

Table 4.5 Time to rupture prediction data using LM analysis.

Temperature (^{o}C)	Stress (ksi)	ln (t_r) - Actual	ln (t_r) - Predicted	Difference	RMS Value
750	20	7.683	7.522	0.161	0.13
750	25	6.213	6.126	0.087	
750	30	4.771	4.729	0.042	
800	20	5.565	5.541	0.024	
800	25	4.060	4.209	-0.149	
800	30	3.091	2.878	0.214	
850	20	3.850	3.736	0.115	
850	25	2.639	2.463	0.176	
850	30	1.099	1.191	-0.092	

Table 4.6 Time to rupture prediction data using OSD analysis.

Temperature (^{o}C)	Stress (ksi)	ln (t_r) - Actual	ln (t_r) - Predicted	Difference	RMS Value
750	20	7.683	7.490	0.193	0.13
750	25	6.213	6.154	0.059	
750	30	4.771	4.818	-0.047	
800	20	5.565	5.579	-0.015	
800	25	4.060	4.243	-0.183	
800	30	3.091	2.907	0.184	
850	20	3.850	3.838	0.012	
850	25	2.639	2.502	0.137	
850	30	1.099	1.163	-0.065	

Table 4.6 Time to rupture prediction data using MH analysis.

Temperature (^{o}C)	Stress (ksi)	ln (t_r) - Actual	ln (t_r) - Predicted	Difference	RMS Value
750	20	7.683	7.348	0.335	0.19
750	25	6.213	6.050	0.162	
750	30	4.771	4.752	0.018	
800	20	5.565	5.640	-0.076	
800	25	4.060	4.234	-0.173	
800	30	3.091	2.827	0.264	
850	20	3.850	3.932	-0.082	
850	25	2.639	2.417	0.222	
850	30	1.099	0.900	0.198	

The MCM analysis, discussed in section 3.4.2, is a more generalized approach and is based on experimental data. The objective of such analysis was to determine the values of constants namely, A, B, C, D, E, R1 and R2. As indicated earlier, the value of A was calculated by using the focal point convergence method. This method considers the negative inverse of the ordinate of a point, where the plots shown in Figures 4.14 and 4.16 converge. For both LM and MH analyses, extrapolation of linear plots to a point of convergence gave 'A' values of +0.0278 and -0.036, respectively. The OSD analysis gave the 'A' value of zero, since the resultant lines were parallel leading to a convergence point of infinity. Table 4.7 summarizes the values of 'A' based on all three approaches. The reference temperature (T_m) of Alloy 230 was considered to be 1073 K (800 ^{o}C), which represents a mid-value within the testing temperature range. Finally, the rupture times at 1023 K (750 ^{o}C) and 1123 K (850 ^{o}C) under applied stress levels of 20, 25 and 30 ksi were used to estimate the magnitude of the other six constants (B, C, D, E, R1 and R2) based on the multiple linear regression analyses, which are given in Table 4.8.

Table 4.7 Theoretical values for the Constant A in MCM analysis

Parameter	Value of 'A'
Larson-Miller	$+\left\|\frac{1}{C}\right\| = +\frac{1}{36} = +0.0278$
Orr-Sherby-Dorn	$\frac{1}{\infty} = 0$
Manson-Hafred	$- -\left\|\frac{1}{\ln t_A}\right\| = -\frac{1}{27.83} = -0.036$

Table 4.8 Estimated values of constants for MCM analysis

	A = 0.0278	A = 0	A = -0.036
R1	0.0052	-0.0278	-0.1004
R2	-31418	-73901	-165629
B	12.029	12.104	12.271
C	0	0	0
D	-0.359	-0.364	-0.374
E	0.0018	0.0019	0.0021

The estimated values of these constants were then substituted in Equation 3.19 to predict the rupture time for different values of 'A', which are shown in Tables 4.9, 4.10 and 4.11 as functions of temperature and applied stress level. An RMS value of 0.09 was obtained by the MCM analysis taking the magnitude of 'A' as 0.0278 based on the LM approach, as shown in Table 4.9. This is the least RMS value obtained so far. With A = 0 and -0.036, the predictions were similar to parametric extrapolations, with RMS values equal to 0.11 and 0.15, respectively.

Table 4.9 Prediction using MCM analysis with constants determined using A = 0.0278

Temperature (^{o}C)	Stress (ksi)	ln (t_r) - Actual	ln (t_r) - Predicted	Difference	RMS Value
750	20	7.683	7.639	0.044	0.09
750	25	6.213	6.191	0.021	
750	30	4.771	4.839	-0.069	
800	20	5.565	5.592	-0.028	
800	25	4.060	4.212	-0.152	
800	30	3.091	2.924	0.167	
850	20	3.850	3.864	-0.013	
850	25	2.639	2.541	0.098	
850	30	1.099	1.306	-0.208	

Table 4.10 Prediction using MCM analysis with constants determined using A = 0

Temperature (^{o}C)	Stress (ksi)	ln (t_r) - Actual	ln (t_r) - Predicted	Difference	RMS Value
750	20	7.683	7.576	0.108	0.11
750	25	6.213	6.190	0.023	
750	30	4.771	4.900	-0.129	
800	20	5.565	5.599	-0.035	
800	25	4.060	4.213	-0.153	
800	30	3.091	2.924	0.167	
850	20	3.850	3.923	-0.072	
850	25	2.639	2.537	0.102	
850	30	1.099	1.247	-0.148	

Table 4.11 Prediction using MCM analysis with constants determined using A = -0.036

Temperature (^{o}C)	Stress (ksi)	ln (t_r) - Actual	ln (t_r) - Predicted	Difference	RMS Value
750	20	7.683	7.467	0.216	0.15
750	25	6.213	6.180	0.033	
750	30	4.771	4.988	-0.217	
800	20	5.565	5.622	-0.058	
800	25	4.060	4.218	-0.158	
800	30	3.091	2.917	0.174	
850	20	3.850	4.040	-0.190	
850	25	2.639	2.536	0.103	
850	30	1.099	1.142	-0.044	

4.6 Results of Creep-Fatigue Testing

The variations of crack length (a) with the number of cycles (N), superimposed for no hold time, and hold times testing at 600, 700 and 800 ^{o}C, are illustrated in Figures 4.19a, 4.19b and 4.19c, respectively. It is interesting to note that, in general, 'a' versus N plots generated under all tested conditions exhibited a linear relationship, showing steeper slopes at longer hold times. These data clearly indicate that the extent of cracking became more pronounced at longer hold times, irrespective of the testing temperature. However, it should be noted that at higher temperatures (700 and 800 ^{o}C), the crack length could not be measured by the DCPD method at hold times of 1000 seconds, and 300, 600 and 1000 seconds, respectively (Figures 4.19b and 4.19c) due to plastic instability of Alloy 230 at these temperatures that caused bending and buckling of the two arms of the tested CT specimens.

Another interesting observation made from these data was the overlapping of 'a' versus N plots at 600 ^{o}C when the test specimen was subjected to cyclic loading at hold times of 60 and 120 seconds, respectively, as shown in Figure 4.19a. Thus, no appreciable crack extension occurred at this temperature even though the hold time was increased from 60 to 120 seconds. However, the crack length was enhanced to some extent at 700 ^{o}C when the CT specimen was held for 120 seconds under longer cycles of loading (Figure 4.19b).

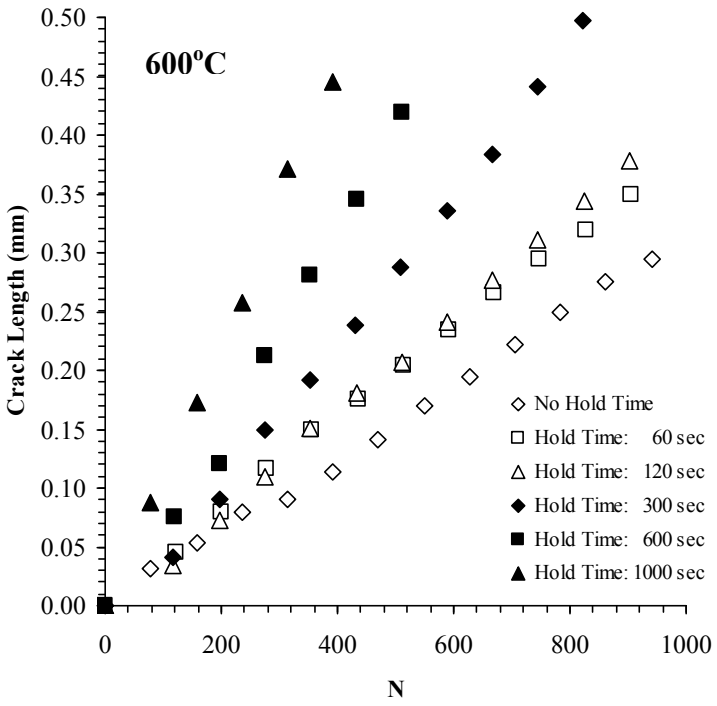
600°C
Crack Length (mm)
N
0.00
0.05
0.10
0.15
0.20
0.25
0.30
0.35
0.40
0.45
0.50
0
200
400
600
800
1000
No Hold Time
Hold Time: 60 sec
Hold Time: 120 sec
Hold Time: 300 sec
Hold Time: 600 sec
Hold Time: 1000 sec

(a)

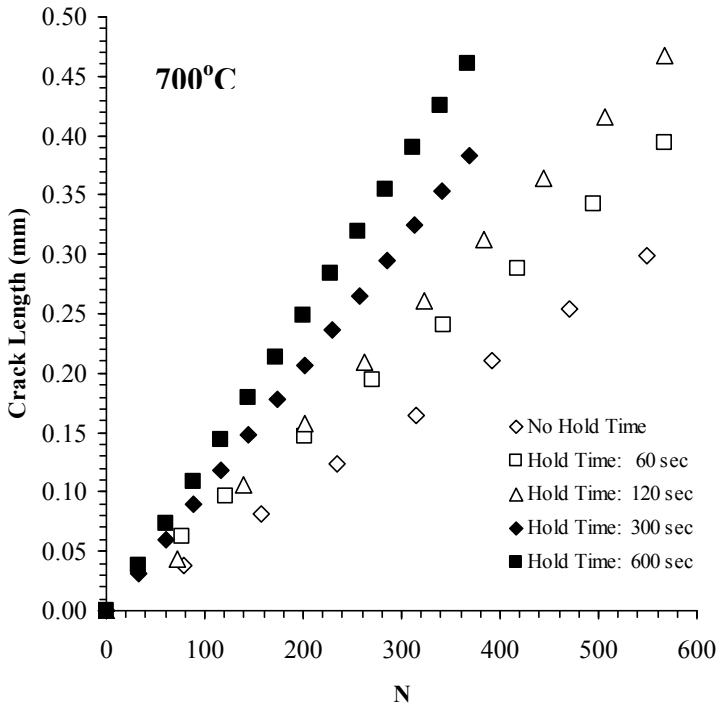
700°C
Crack Length (mm)
N
0.00
0.05
0.10
0.15
0.20
0.25
0.30
0.35
0.40
0.45
0.50
0
100
200
300
400
500
600
No Hold Time
Hold Time: 60 sec
Hold Time: 120 sec
Hold Time: 300 sec
Hold Time: 600 sec

(b)

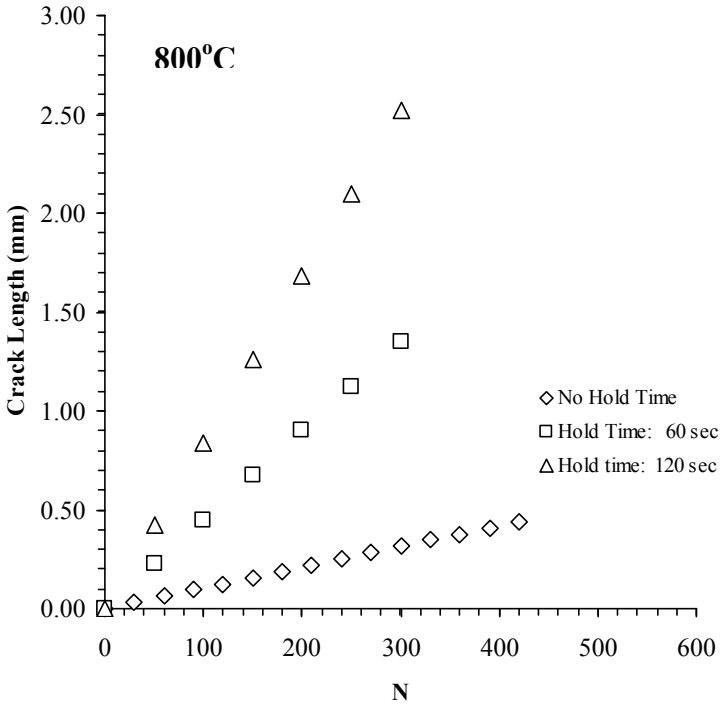

(c)

Figure 4.19 Crack Length vs. N. (a) 600 °C; (b) 700 °C; (c) 800 °C

The data, shown in Figure 4.19, were subsequently converted to crack-growth-rate (CGR) in terms of da/dN that were plotted as a function of hold time at three different tested temperatures, as illustrated in Figure 4.20. These results clearly indicate that substantial crack-growth occurred at 800 °C even at shorter hold times of 60 and 120 seconds. Further, the same test specimen could not sustain any cyclic loading at longer hold times (300, 600 and 1000 seconds) at this temperature, suggesting that Alloy 230 may not be capable to withstand the long-term creep-fatigue loading constraint at temperatures in the vicinity of 800 °C. In a similar manner, this alloy showed unstable crack-growth when tested at 700 °C at a hold time of 1000 seconds.

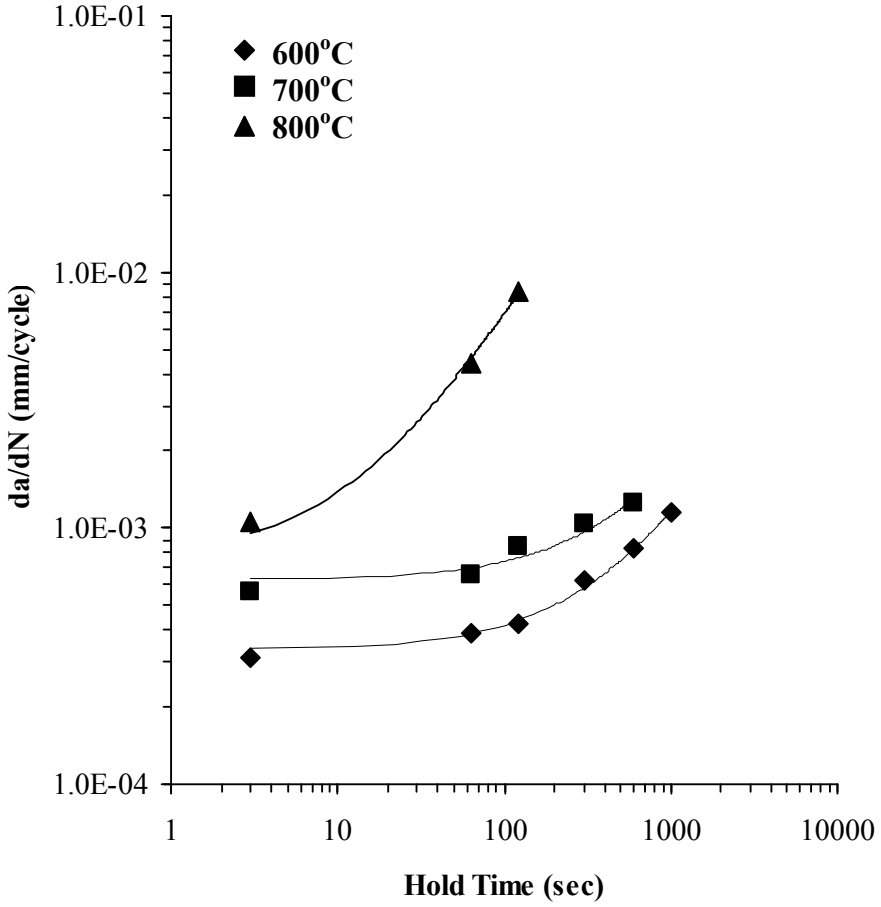

Figure 4.20 da/dN vs. Hold Time

Based on the data shown in Figures 4.19 and 4.20, it appears that temperature plays an important role in enhancing the CGR of Alloy 230 under creep-fatigue conditions incorporated in this investigation. Figure 4.21 illustrates 'a' versus N plots as functions of both temperature and hold time.

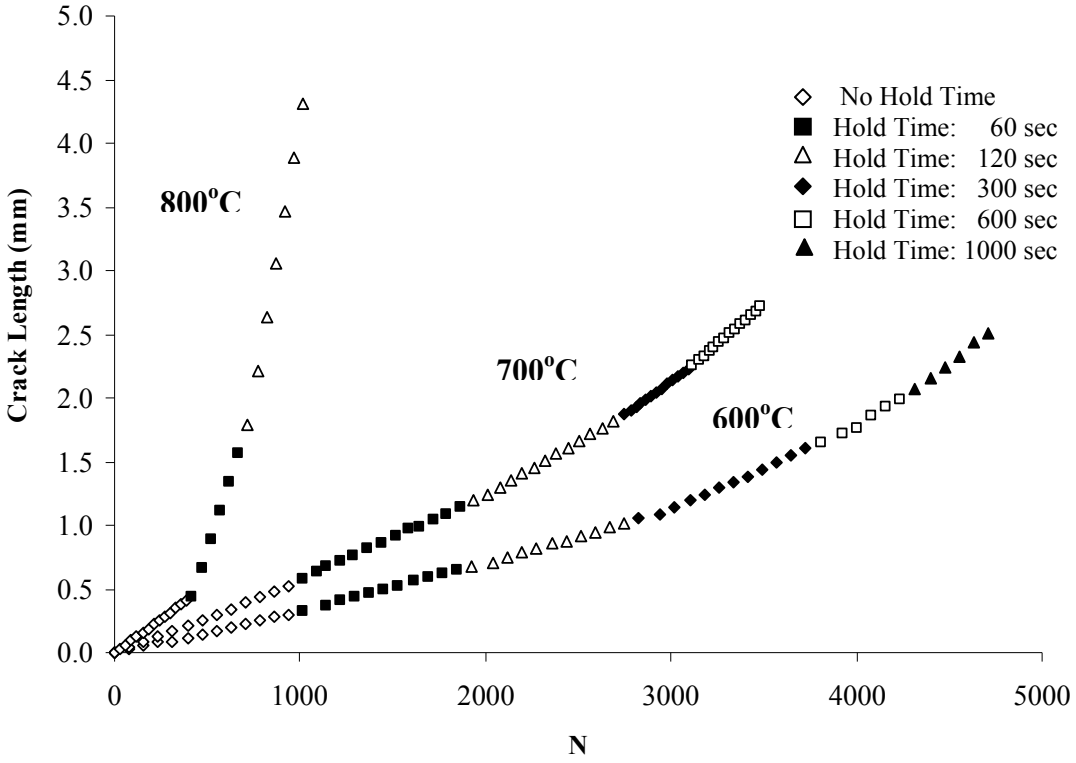

Figure 21 Crack Length vs. N as Functions of Temperature and Hold Time

It is interesting to note that this alloy was capable to withstand a maximum number of loading cycle (N) at 600 ^{o}C even up to the longest hold time of 1000 seconds. However, the magnitude of N was substantially reduced at higher testing temperatures, showing a drastic drop in the N value at 800 ^{o}C. Further, this alloy could not sustain combined creep-fatigue loading cycles for holding times in excess of 120 seconds at this temperature. A similar observation with respect to the combined effects of temperature and hold time on crack-growth behavior of other austenitic superalloys has been reported elsewhere [71]. Thus, it is obvious that the creep-fatigue behavior of Alloy 230 has to be optimized in terms of a synergistic interaction between the temperature-induced loading cycles and the hold time for propagation of cracking.

Efforts have also been made to develop a relationship between the rate of crack propagation (da/dN) and the testing frequency (f), as a function of temperature. The hold time has been converted to 'f' by using Equation 4.1.

$$f = (T + t_h)^{-1} \qquad \text{Equation 4.1}$$

where T is the cyclic time of the baseline triangular waveform (3 second) and t_h is the hold time imposed at P_{max} (60, 120, 300, 600 and 1000 seconds, respectively). The variation of da/dN with 'f' is shown in Figure 4.22 for all three tested temperatures on a log-log scale. All three plots, corresponding to different testing temperatures, exhibited a linear relationship with somewhat different slopes up to certain cyclic frequencies, indicating a time-dependency on da/dN. Negative slopes of 0.017, 0.038 and 0.042 (at 600, 700 and 800 ^{o}C, respectively) were calculated from these three lines, implying that da/dN of Alloy 230 was inversely proportional to the cyclic frequencies at the tested temperatures. Such trend indicates that crack length was a direct function of time, without any dependence on the number of cycles. Further, a relatively steeper slope at 800 ^{o}C indicates a faster CGR at both no hold and shorter hold times (60 and 120 seconds), confirming a detrimental effect of higher temperature on the cracking tendency. Thus, the crack-growth behavior of this alloy at 800 ^{o}C was totally time-dependent for three cyclic frequencies, as shown in Figure 4.22.

At 600 and 700 ^{o}C, the crack-growth behavior was mixed time and cycle-dependent at frequencies ranging from 9 x 10^{-4} to 0.33 Hz. At or slightly below a frequency of 0.33 Hz, CGR was independent of the testing frequency, where the crack length at any time was a function of the number of applied stress cycle, i.e. cycle-dependent. Thus, the transition from the cycle-dependent to mixed time-cycle-dependent CGR at these

temperatures occurred within a lower frequency range of 9 x 10^{-4} to 1.58 x 10^{-2} Hz. The creep-damage zone at the crack-tip was, therefore, time-dependent and grew faster while the fatigue-damage zone was dependent on the ΔK value that did not change much during crack-growth testing. In essence, the overall crack-extension due to the combined creep-fatigue interaction was influenced by both the cyclic frequency and hold time as a function of the tested temperatures.

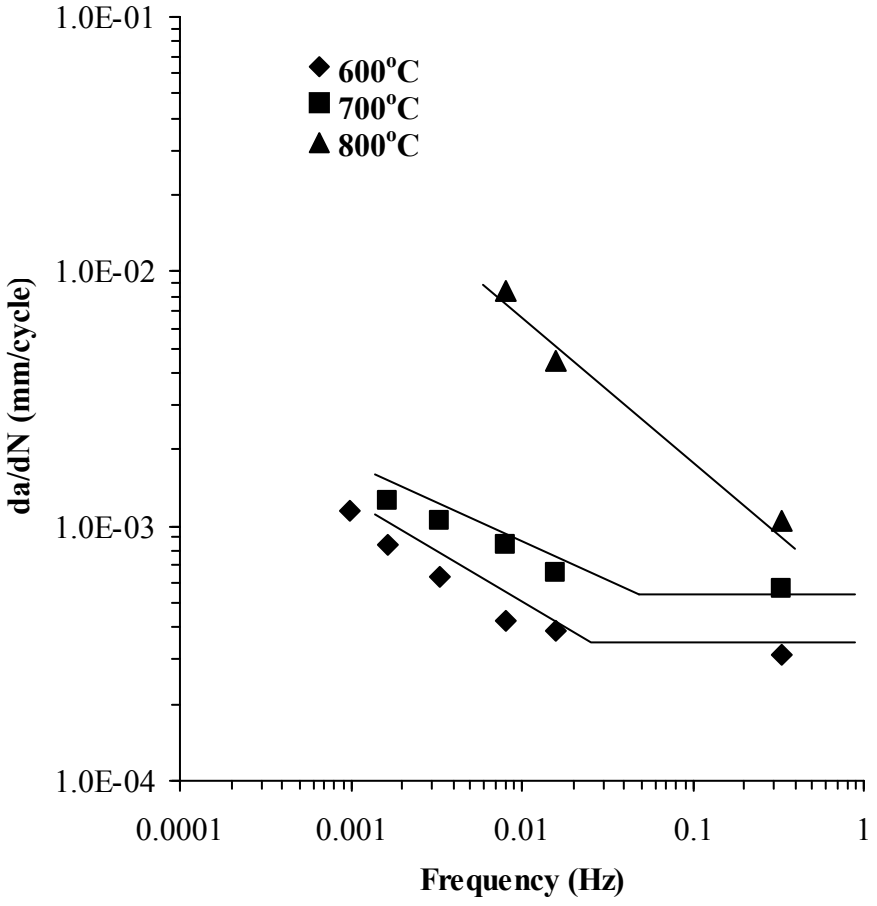

Figure 4.22 da/dN vs. Frequency

The optical micrographs of the cross-sections through the fractured surfaces of Alloy 230 tested at 600 and 800 ^{o}C for different hold times are illustrated in Figures 4.23 and 4.24, respectively. An evaluation of the micrographs shown in Figure 4.23 reveals that at 600 ^{o}C, precipitates were formed both within the austenite grains and along the grain boundaries. However, very little precipitates were observed in the specimen tested solely under cyclic loading without any hold time (Figure 4.23a). The extent of precipitation was gradually enhanced as the hold time was increased from 60 to 1000 seconds, as shown in Figures 4.23b through 4.23d. Further, with longer hold times, significant amount of precipitation occurred along the grain boundaries causing severe intergranular cracking, which is a manifestation of time-dependent deformation or creep at a particular temperature.

A similar observation was made with the specimens tested at higher temperatures, with and without hold time, as illustrated in Figures 4.24a and 4.24b. It should, however, be noted that the extent of intergranular cracking was more pronounced at 800 ^{o}C even at a much shorter hold time of 120 seconds. Thus, once again, the inference is strong that the combined effect of temperature and hold time will have a profound impact on the performance of Alloy 230 under creep-fatigue conditions.

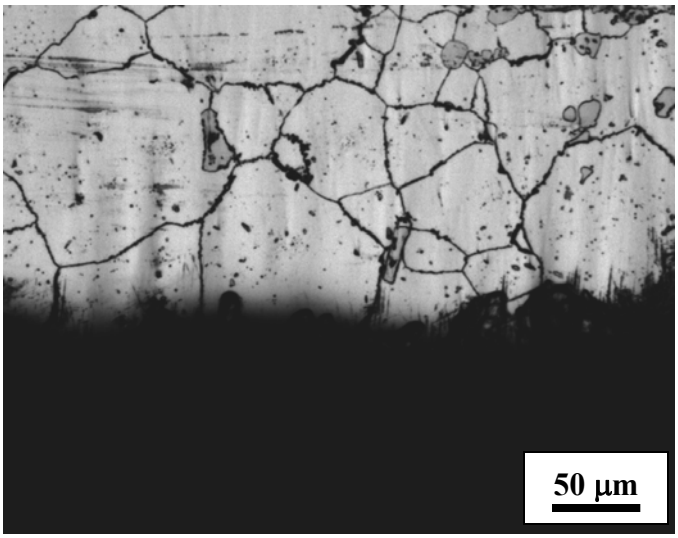

(a) No Hold Time

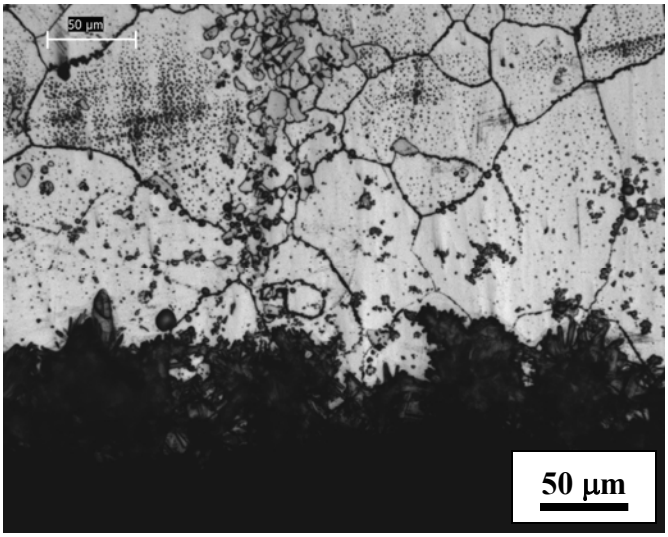

(b) Hold Time: 120 sec

Figure 4.23 Optical Micrographs of Specimen Tested at 600 ^{o}C
….continued to next page

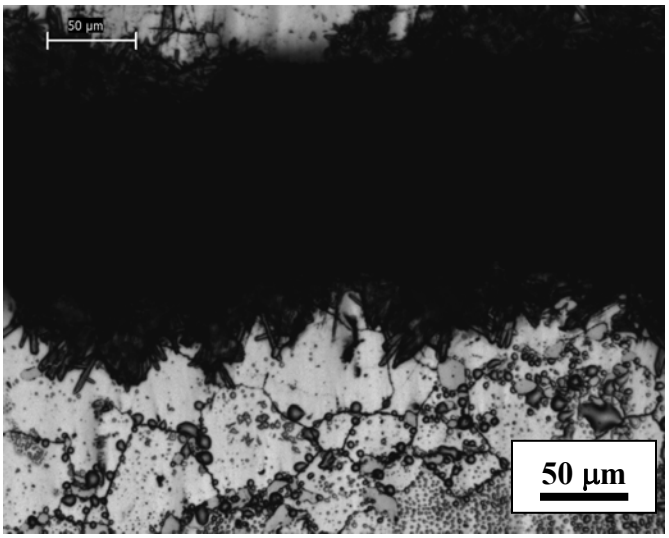

(c) Hold Time: 600 sec

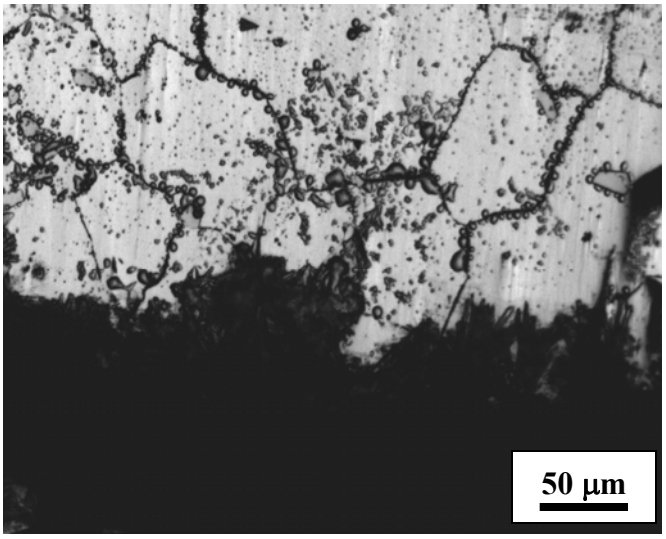

(d) Hold Time: 1000 sec

Figure 4.23 Optical Micrographs of Specimen Tested at 600 ^{o}C (contd….)

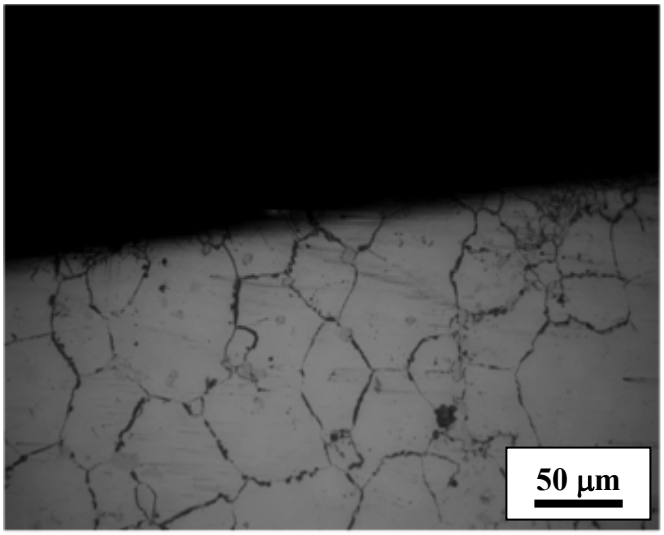

(a) No Hold Time

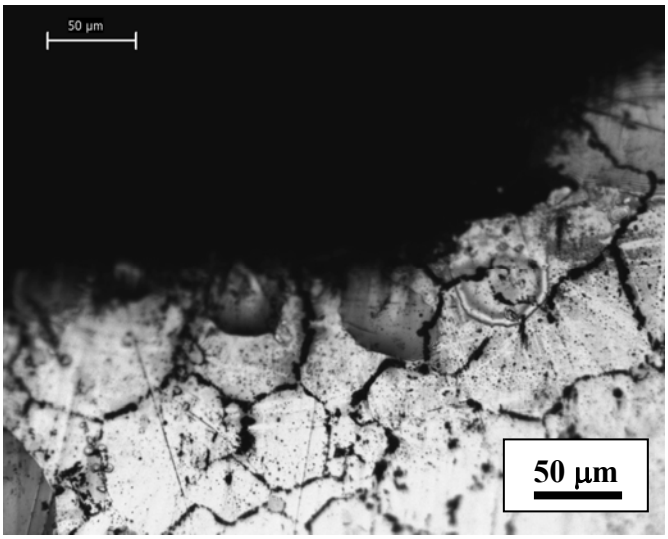

(b) Hold Time: 120 sec

Figure 4.24 Optical Micrographs of Specimen Tested at 800 ^{o}C

Figures 4.25, 4.26 and 4.27 show the SEM micrographs of the fractured surfaces of specimens tested at 600, 700 and 800 ^{o}C, respectively, with and without hold time. Fractures of Alloy 230 at 600 and 700 ^{o}C without any hold time were predominantly characterized by well-defined striations resulting from cyclic loading, as illustrated in Figures 4.25a and 4.26a, respectively. A very few transgranular cracks were also seen in these micrographs. At 600 ^{o}C and 120 second-hold time, this alloy exhibited striations and transgranular cracking, with a very few intergranular cracks (Figure 4.25b). However, the mode of cracking became mostly intergranular at this temperature as the hold time was increased to 600 and 1000 seconds, as shown in Figure 4.25c. Even though a mixed transgranular/intergranular cracking mode was observed when a hold time of 120 second was imposed at 700 ^{o}C, this alloy showed predominantly intergranular cracking at the 600 second hold time (Figures 4.26b and 4.26c, respectively). Finally, the fracture morphology was changed from mixed transgranular/intergranular to solely intergranular cracking mode at 800 ^{o}C due to the introduction of a 120 second hold time at P_{max} , as illustrated in Figures 4.27a and 4.27b, respectively.

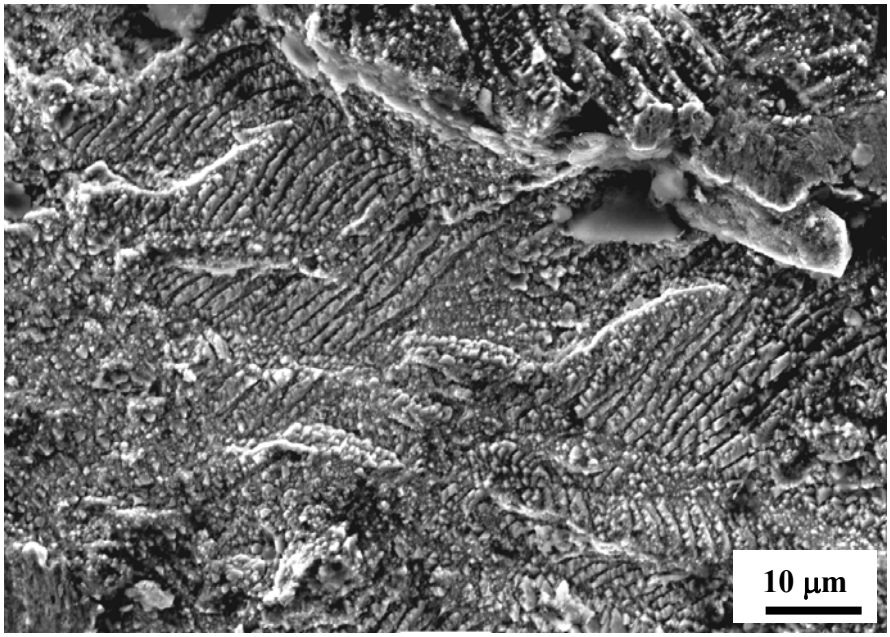

(a) No Hold Time

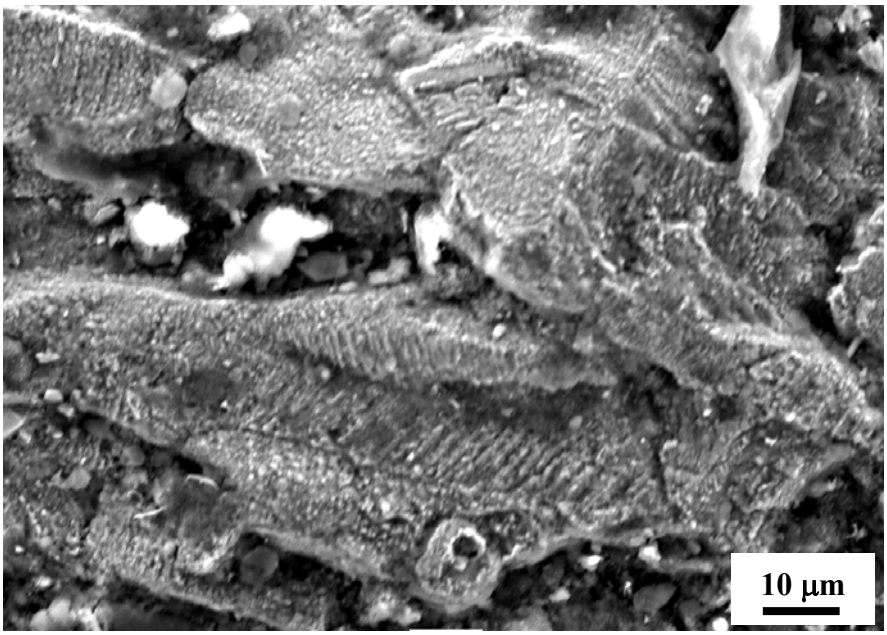

(b) Hold Time: 120 sec

Figure 4.25 SEM Micrographs of Specimen Tested at 600 ^{o}C

….. continued to next page

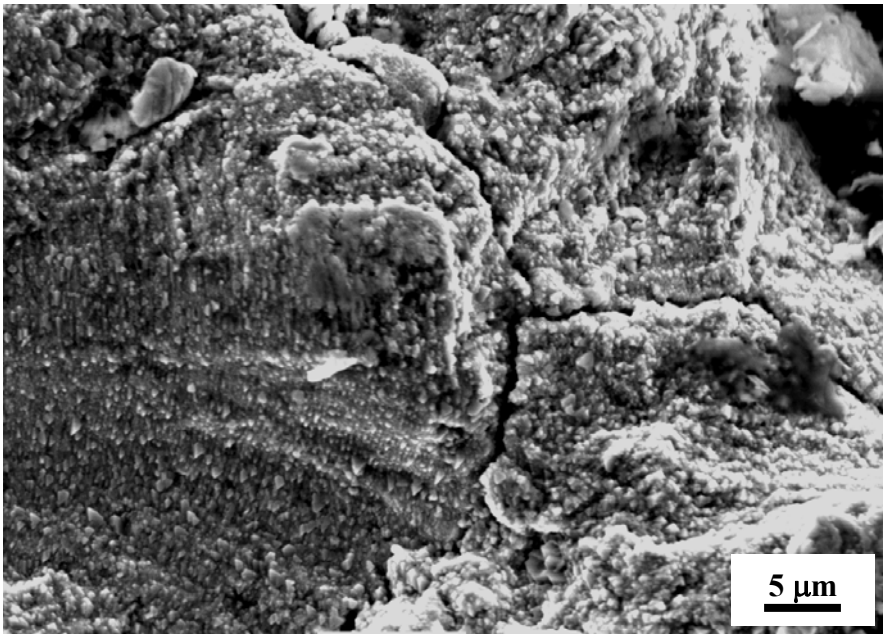

(c) Hold Time: 1000 sec

Figure 4.25 SEM Micrographs of Specimen Tested at 600 ^{o}C (continued…)

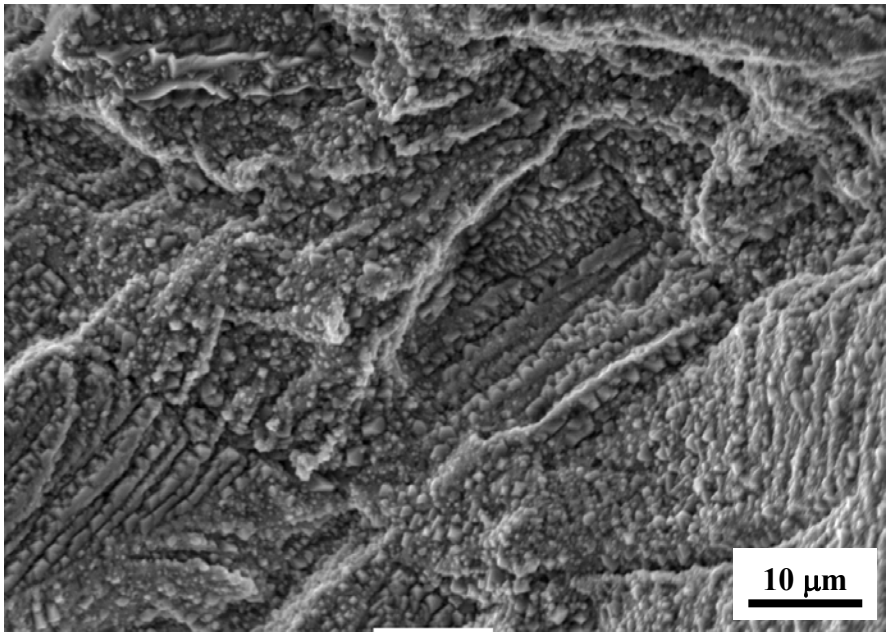

(a) No Hold Time

Figure 4.26 SEM Micrographs of Specimen Tested at 700 ^{o}C

…..continued to next page

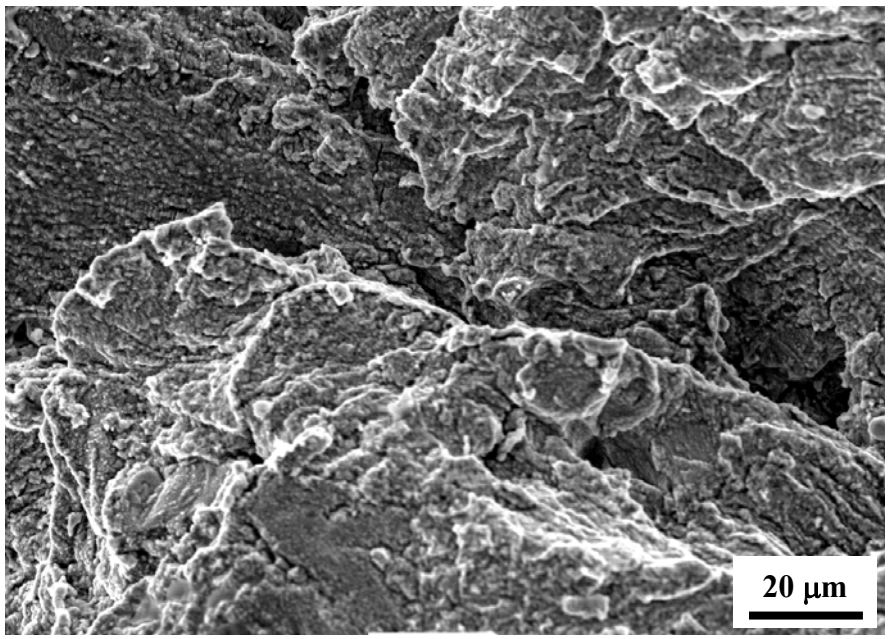

(b) Hold Time: 120 sec

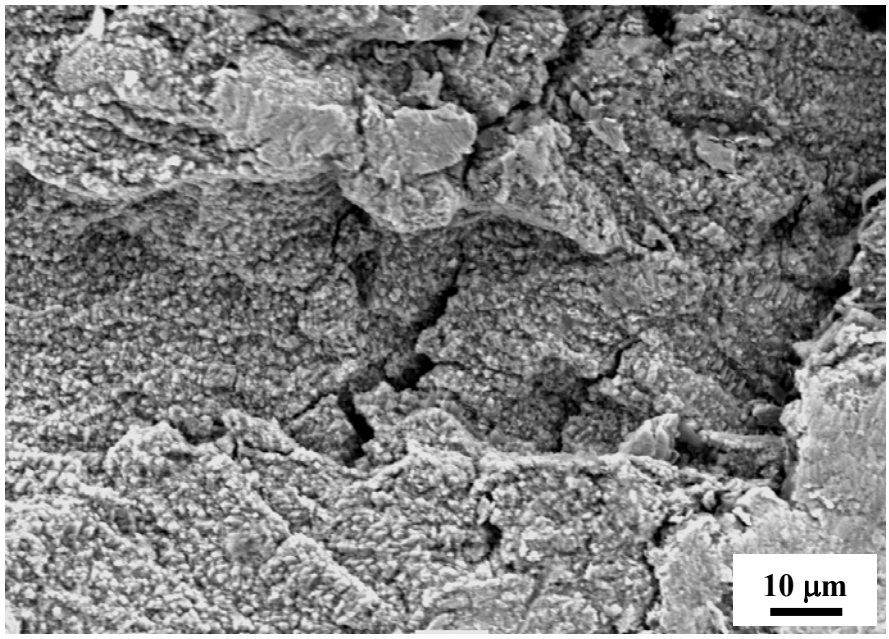

(c) Hold Time: 600 sec

Figure 4.26 SEM Micrographs of Specimen Tested at 700 ^{o}C (continued…)

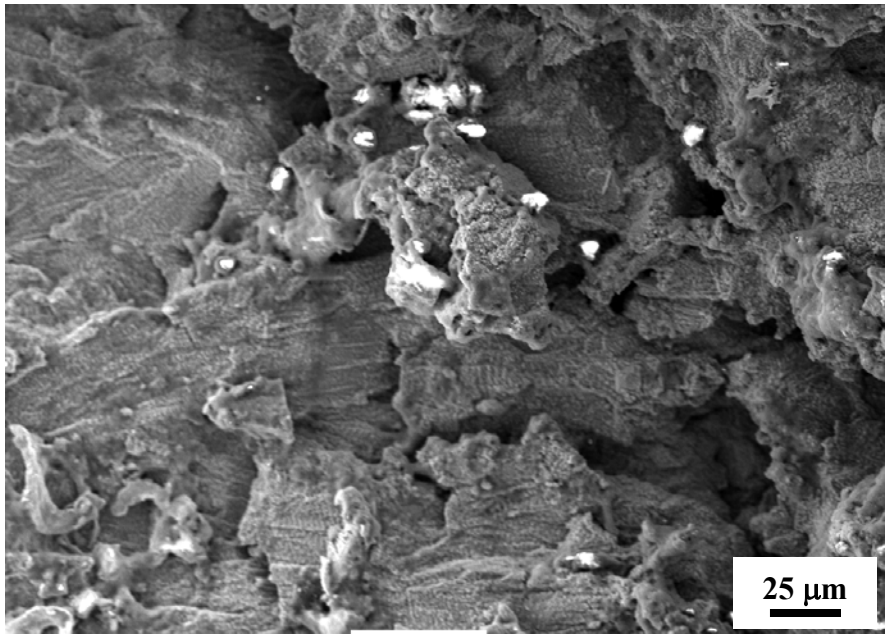

(a) No Hold Time

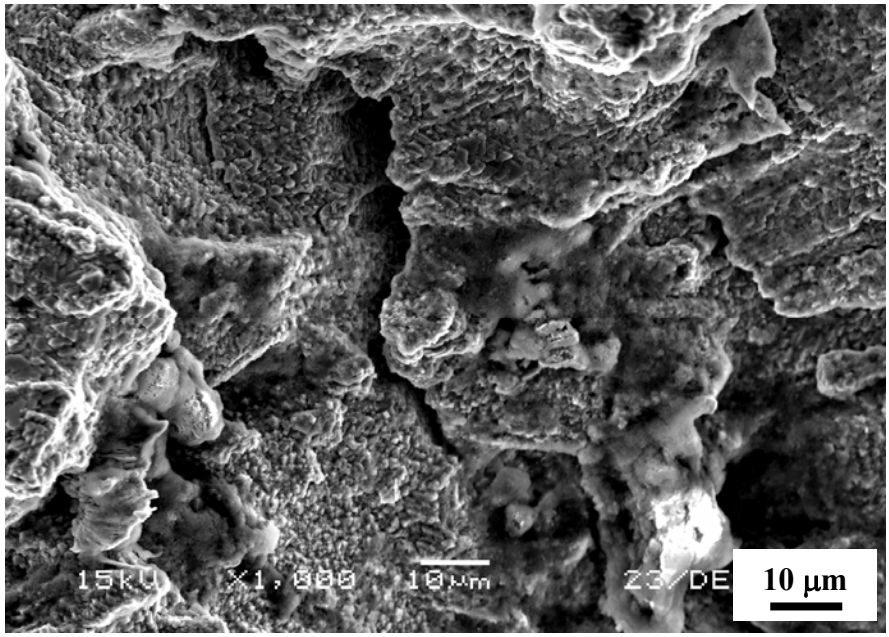

(b) Hold Time: 120 sec

Figure 4.27 SEM Micrographs of Specimen Tested at 800 ^{o}C

CHAPTER 5

DISCUSSION

This investigation was focused on the evaluation of metallurgical and mechanical properties of Alloy 230, in particular, its creep and stress-rupture behavior, fracture toughness, and creep-fatigue interaction under conditions relevant to the NGNP program. The significant results obtained from this work are discussed in separate sections as outlined below.

5.1 Tensile Properties Evaluation

Baseline tensile data were generated for calculating the values of applied stresses used in creep testing. The results of tensile testing, performed at temperatures ranging from ambient to 950 ^{o}C, were presented in superimposed graphical format (s-e diagram), and in a tabular form showing the magnitude of YS, UTS, %El and %RA. As expected, the magnitudes of YS and UTS were gradually reduced with increasing temperature. Serrations of different heights were also seen in the s-e diagrams generated at 300 and 500 ^{o}C that may indicate the occurrence of the DSA phenomenon. However, the characterization of DSA was not performed since it was beyond the scope of this work...

5.2 Fracture Toughness Evaluation

Fracture toughness of this alloy, in terms of J_{1C}, was evaluated only at ambient temperature. Testing at elevated temperatures could not be performed due to a limitation in equipment usage. A J_{1C} value of 98.27 KJ/m^2 was determined that was relatively lower than the fracture toughness values of other Ni-base alloys including Alloys 617 and 276 [6, 65]. The lower J_{1C} value of Alloy 230 could be attributed to the presence of W, causing a greater susceptibility to brittle failure.

5.3 Creep Deformation Evaluation

The results of creep testing involving Alloy 230 indicate that this alloy satisfied a maximum allowable strain criterion of 1% following 1000 hours of loading at applied stresses corresponding to its 0.10YS values at all three tested temperatures. However, this alloy failed to meet this acceptance criterion when tested under applied stresses equivalent to its 0.25YS values at 850 and 950 ^{o}C. Thus, it can be stated that this alloy could be safely used as a heat exchanger material at operating temperatures of up to 950 ^{o}C, when the applied stress levels are maintained within the 0.10YS values.

As anticipated, the steady-state creep rate was enhanced with increasing temperature and applied stress level, verifying that creep is a thermally-activated phenomenon, and the cracking tendency is influenced by the magnitude of the applied stress. However, an anomalous behavior was observed at 750 and 850 ^{o}C, where the steady-state creep rate and total creep strain following 1000 hours of testing were slightly higher at 750 ^{o}C, compared to those at 850 ^{o}C when loaded under an applied stress equivalent to its 0.10YS value at this temperature. Such anomaly in creep deformation behavior of Alloy 230 can be explained by a precipitation hardening mechanism, discussed in the results section.

5.4 Stress Rupture Evaluation

Analytical and empirical techniques were used to predict the long-term creep-rupture behavior of Alloy 230 with a minimum error. Techniques based on Larson-Miller (LM) analysis, Orr-Sherby-Dorn (OSD) analysis, and Manson-Hafred (MH) analysis was applied. The LM analysis proved to be the most efficient approach and exhibited a minimum error in the prediction of rupture time. Nevertheless, all three applied methods were used to develop master plots at temperatures spanning a wide range that could

determine the different stress-rupture parameters for a particular stress level. A major drawback of this method is that its accuracy depends on a large number of testing data. Further, this approach does not consider metallurgical instabilities resulting from changes in temperature and stress level. Thus, for accuracy, it is necessary to conduct a large number of testing over a wide range in temperature and stress level involving different heats of a material for a specific time period. Analyses based on a minimum commitment method (MCM) are, therefore, effective in eliminating the drawbacks associated with the use of LM, OSD, and MH techniques. MCM analyses using a time-temperature-stress equation was very effective in predicting the rupture time of Alloy 230 for specific temperature and stress level combinations without showing any major error.

5.5 Creep-Fatigue Interaction Evaluation

The results of creep-fatigue testing indicate that the cracking susceptibility of Alloy 230 became more pronounced when this alloy was subjected to longer hold times. However, temperature also played an important role in that the crack-growth-rate (CGR), in terms of da/dN, was substantially higher at 800 ^{o}C compared to those at 600 and 700 ^{o}C even at shorter hold times of 60 and 120 seconds. It is interesting to note that this alloy could sustain a maximum number of loading cycle at 600 ^{o}C even up to the longest hold time of 1000 seconds. On the contrary, this alloy was unable to sustain creep-fatigue loading constraint for durations exceeding 120 seconds at 800 ^{o}C. Thus, an optimization has to be made as to the synergistic interaction between the temperature-induced loading cycle and hold time for crack-growth. This observation was consistent with the results cited in the open literature. The results also indicate that CGR of this

alloy was a function of both hold time and applied stress cycle at 600 and 700 ^{o}C. However, at 800 ^{o}C, CGR was totally time-dependent.

The optical micrographs revealed substantial precipitation along the grain boundaries of the tested specimens, leading to intergranular cracking, the extent of cracking being more pronounced at 800 ^{o}C even under a much shorter hold time of 120 seconds. At 600 ^{o}C, the concentration of intergranular precipitates was gradually enhanced with longer hold times. The fracture mode was changed from transgranular to mixed transgranular/ intergranular, then to predominantly intergranular due to the imposition of longer hold times and/or increasing temperatures. Thus, the cracking susceptibility of Alloy 230 was influenced by both hold time and temperature.

CHAPTER 6

SUMMARY AND CONCLUSIONS

Alloy 230 has been extensively studied for evaluation of its metallurgical and mechanical properties under conditions relevant to the NGNP application. The key results and the significant conclusions drawn from this investigation are summarized below.

- Alloy 230 showed serrations in the s-e diagrams at 300 and 500 ^{o}C that could be the result of the DSA phenomenon. Both YS and UTS were gradually reduced with increasing temperature. However, the ductility was enhanced due to increased plastic flow at elevated temperatures.
- A J_{1C} value of 98.27 KJ/m^2 was determined for this alloy, which was lower than that of other Ni-base alloys considered for NGNP application.
- Alloy 230 exhibited a significant resistance to creep deformation under applied stresses equivalent to its 0.10YS values at 750, 850 and 950 ^{o}C. The total creep strain did not exceed 1% following 1000 hours of loading under these experimental conditions, thus satisfying the maximum strain acceptance criterion.
- The steady state creep rate was enhanced with increasing temperature and applied stress level. The activation energy for creep deformation of this alloy was calculated to be 195 and 90 KJ/mol-K, respectively for applied stresses equivalent to its 0.10YS and 0.25YS values. However, these values could not be compared due to a lack of literature data.
- Dislocation creep was the dominant mechanism of creep deformation of Alloy 230. The mobility of dislocations was found to be influenced by the morphology of second phase particles such as Ni_2 (Cr, W) superstructures, and carbide

precipitates including Ni_3W_3C and $Cr_{23}C_6$. While the formation of superstructures is favored at lower temperatures and stress levels, carbide precipitates can form at higher temperatures.

- The results of stress rupture testing indicate that the rupture time was enhanced with a reduction in temperature and applied stress level.
- Of all applied analytical methods, the LM approach appeared to be most effective in predicting the rupture time of Alloy 230, showing a minimum error.
- The MCM analysis, based on a time-temperature-stress equation, proved to be very useful in predicting the creep-rupture properties of Alloy 230 with a highest accuracy.
- An enhanced cracking tendency of Alloy 230, due to the synergistic effect of creep and fatigue, was observed at elevated temperatures. The number of cycles to failure was reduced at higher temperatures even after shorter hold times. While failure of this alloy was totally time-dependent at 800 ^{o}C, a mixed time and cycle dependency on cracking was noted at 600 and 700 ^{o}C.
- The increased CGR at higher temperatures and longer hold times was characterized by grain-boundary precipitation in the tested specimens, leading to intergranular cracking. The extent of intergranular precipitation was more pronounced at 800 ^{o}C even after a very short hold time of 120 seconds. Simultaneously, the concentration of intergranular precipitates was enhanced with longer hold times at 600 ^{o}C.
- The morphology of failure was changed from transgranular to mixed transgranular / intergranular, then to predominantly intergranular due to the

imposition of longer hold times and/or increasing temperatures. Thus, the cracking susceptibility of Alloy 230 was influenced by both hold time and temperature.

CHAPTER 7

SUGGESTED FUTURE WORK

- Fracture toughness evaluation using J_{1C} Testing at elevated temperatures can depict the resistance to fracture of Alloy 230 in presence of flaw at temperatures relevant to NGNP applications.

APPENDIX A

TEST MATRIX- MATERIAL CONSORTIUM

Team Member	High Temp.*	Int.- High Temp.**	Int. Temp.***	Creep (Air)	Creep [f(PO_2)]	Creep Crack Growth (Air)	Creep Crack Growth [f(PO_2)]	Creep-Fatigue (Air)	Creep-Fatigue [f(PO_2)]	Fatigue/ Static (SCC) (Air)	Fatigue/ Static (SCC) [f(PO_2)]	Microstructure Modeling Microstructure Evolution	Cracking Modeling	Constitutive Modeling
MIT		X[4]	X	P[3]	P	C[2]	L[1]	P	P	C	L	C	L	C
BSU	X	X	X	P	P	L	P	P	P	L	P	L	C	C
UNLV	X	X		L	C	C	P	L	P	P	P	C	P	C
Illinois	X	X		C	L	C	C	C	L	P	P	C	C	L
INL	X	X		P	P	C	C	C	C	C	C	C	C	C
ORNL	X	X		C	C	C	C	P	P	P	P	C	P	C

* 800-1000°C

** 700-850°C

***600-750°C

MIT: Massachusetts Institute of Technology

BSU: Boise State University

UNLV: University of Nevada Las Vegas

INL: Idaho National laboratory

ORNL: Oak-Ridge National laboratory

- L indicates lead organization with primary responsibility in area-responsible for coordinating the overall effort in an area and production of deliverables.
- C indicated collaborator in an area who, while not the "Lead" will still do significant work in an area although the level of effort will not be as high as the Lead organization.
- P indicates that the organization will participate in the overall integrated process but will not have active work in an area-no funded scope.
- X indicates temperature regime of area

APPENDIX B

REACTOR SYSTEMS PROPOSED FOR NGNP PROGRAM

B1. Gas Cooled Fast Reactor (GFR) System [2]

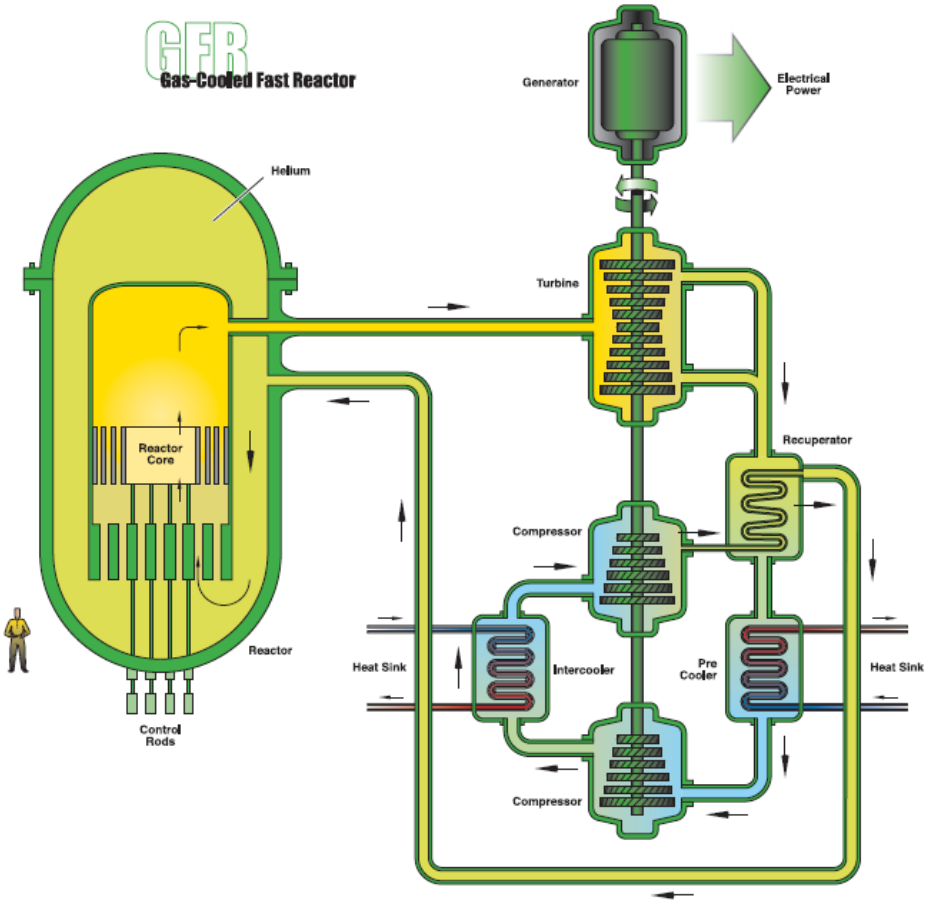

Reactor Parameters	Reference Value
Reactor power	600 MWth
Net plant efficiency (direct cycle helium)	48%
Coolant inlet/outlet temperature and pressure	490°C/850°C at 90 bar
Average power density	100 MWth/m3
Reference fuel compound	UPuC/SiC (70/30%) with about 20% Pu content
Volume fraction, Fuel/Gas/SiC	50/40/10%
Conversion ratio	Self-sufficient
Burnup, Damage	5% FIMA; 60 dpa

B2. Lead Cooled Fast Reactor (LFR) System [2]

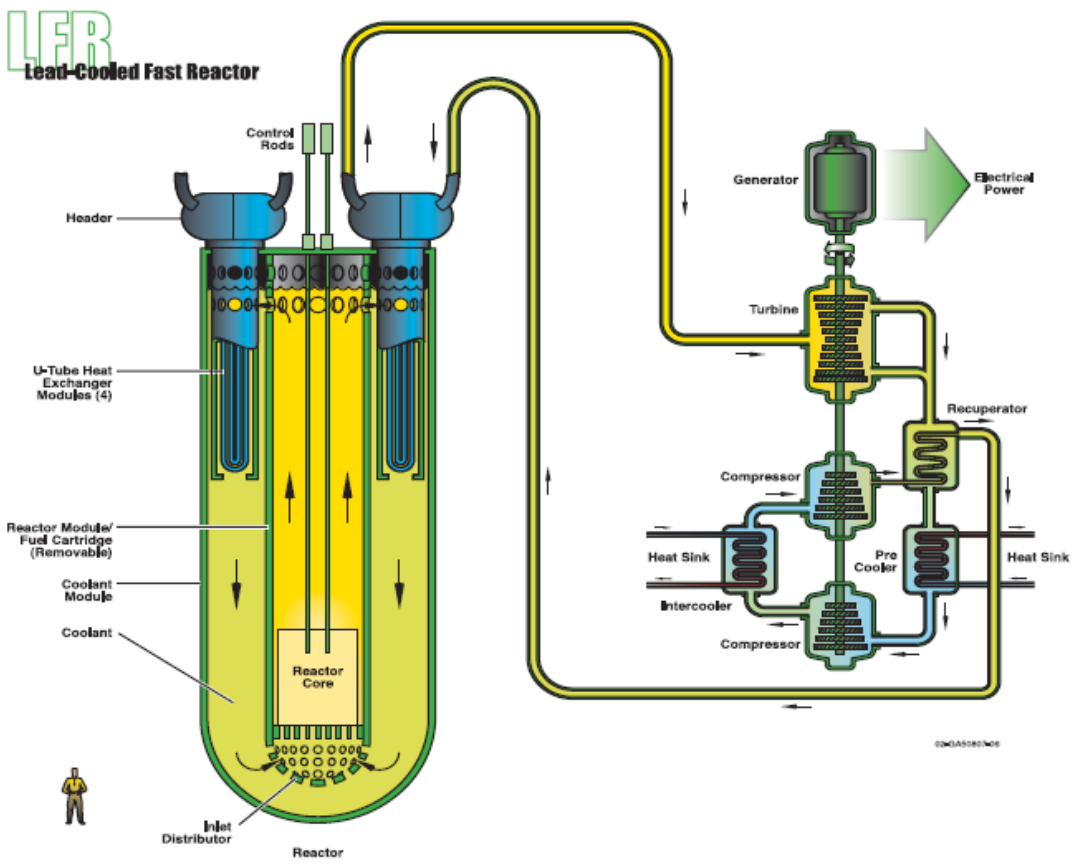

Reactor Parameters	Reference Value			
	Pb-Bi Battery (nearer-term)	Pb-Bi Module (nearer-term)	Pb Large (nearer-term)	Pb Battery (far-term)
Coolant	Pb-Bi	Pb-Bi	Pb	Pb
Outlet Temperature (°C)	~550	~550	~550	750–800
Pressure (Atmospheres)	1	1	1	1
Rating (MWth)	125–400	~1000	3600	400
Fuel	Metal Alloy or Nitride	Metal Alloy	Nitride	Nitride
Cladding	Ferritic	Ferritic	Ferritic	Ceramic coatings or refractory alloys
Average Burnup (GWD/MTHM)	~100	~100–150	100–150	100
Conversion Ratio	1.0	d≥1.0	1.0–1.02	1.0
Lattice	Open	Open	Mixed	Open
Primary Flow	Natural	Forced	Forced	Natural
Pin Linear Heat Rate	Derated	Nominal	Nominal	Drated

B3. Molten Salt Reactor (MSR) System [2]

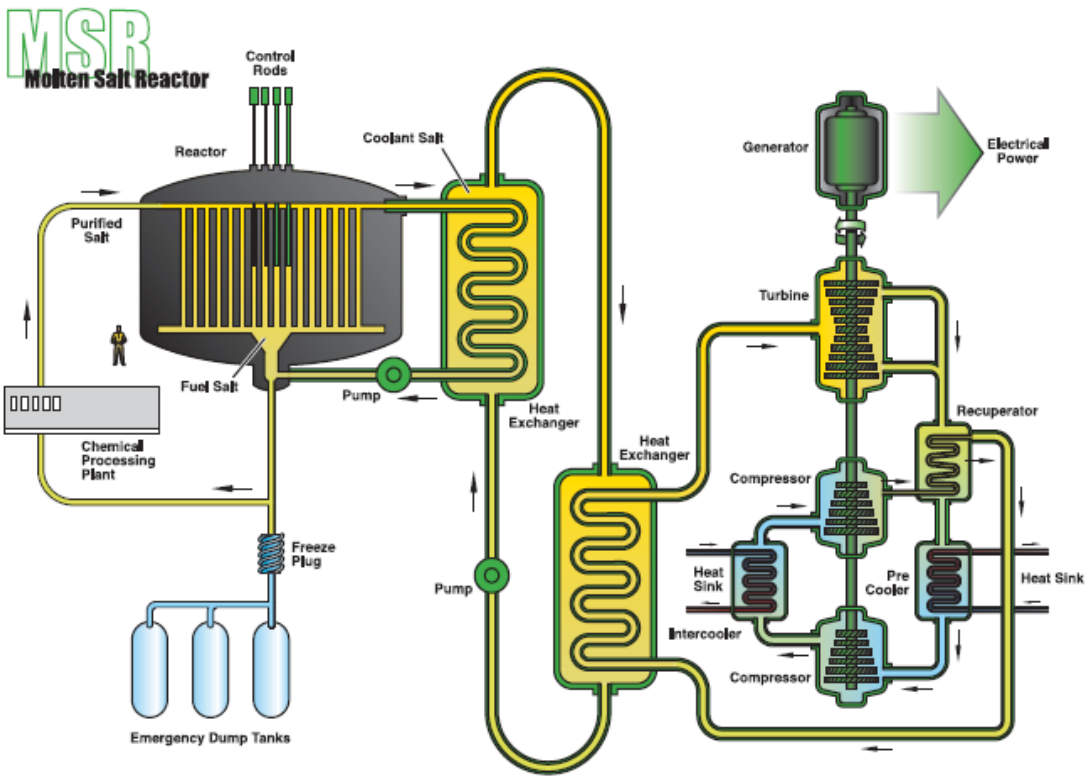

Reactor Parameters	Reference Value
Net power	1000 MWe
Power density	22 MWth/m^3
Net thermal efficiency	44 to 50%
Fuel-salt – inlet temperature	565°C
– outlet temperature	700°C (850°C for hydrogen production)
– vapor pressure	<0.1 psi
Moderator	Graphite
Power Cycle	Multi-reheat recuperative helium Brayton cycle
Neutron spectrum burner	Thermal–actinide

B4. Sodium-Cooled Fast Reactor (SFR) System [2]

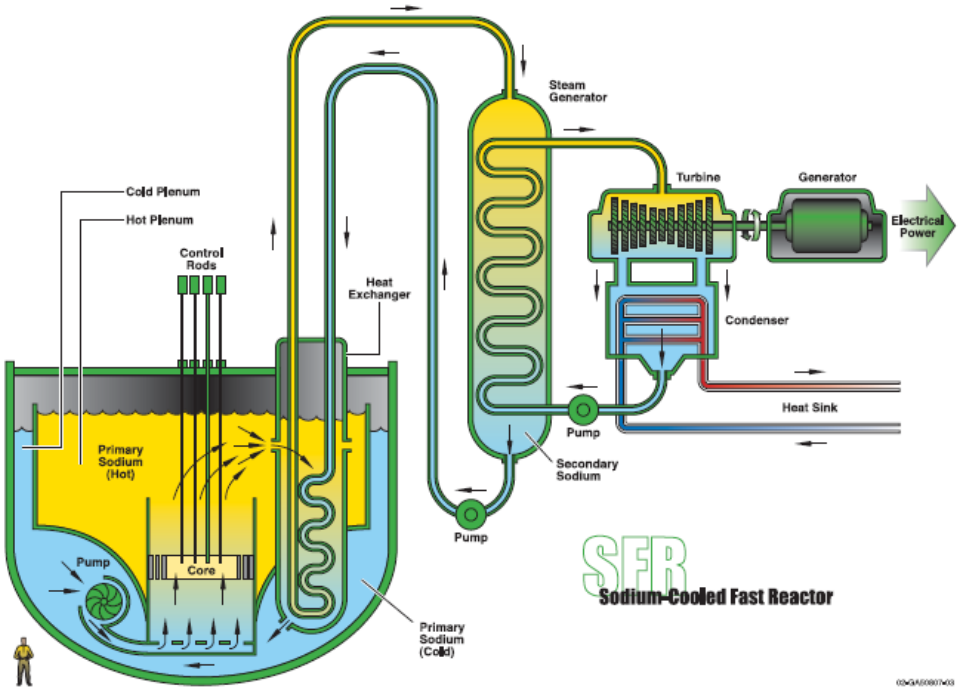

Reactor Parameters	Reference Value
Outlet Temperature	530-550 °C
Pressure	~1 Atmospheres
Rating	1000-5000 MWth
Fuel	Oxide or metal alloy
Cladding	Ferritic or ODS ferritic
Average Burnup	~150-200 GWD/MTHM
Conversion Ratio	0.5-1.30
Average Power Density	350 MWth/m^3

B5. Supercritical-Water-Cooled Reactor (SCWR) System [2]

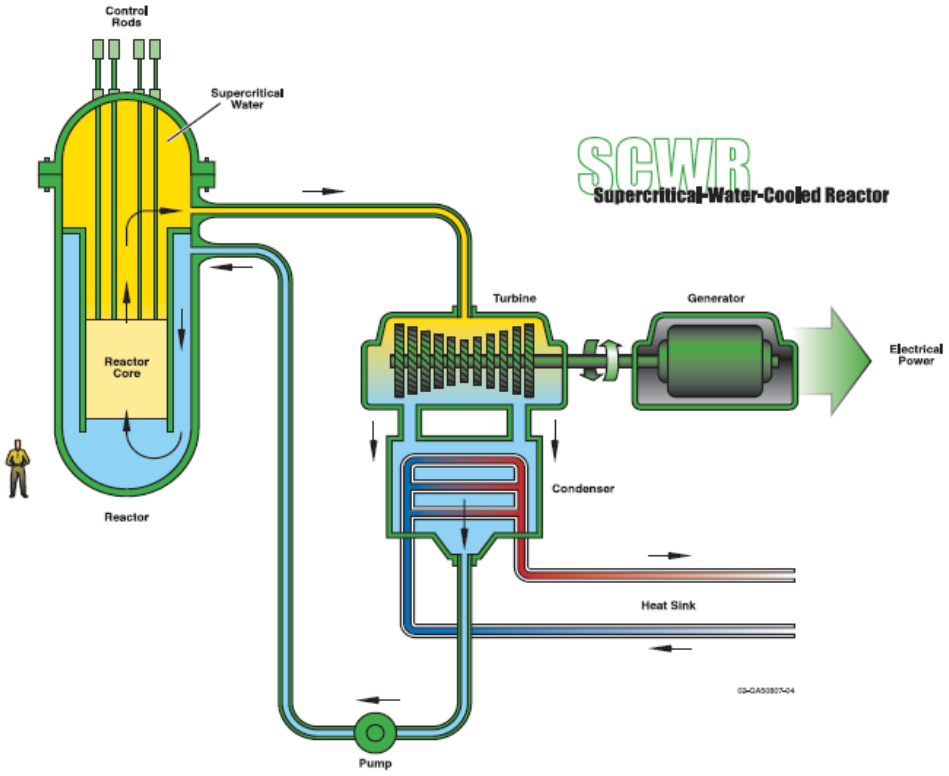

Reactor Parameters	Reference Value
Plant capital cost	$900/KW
Unit power and neutron spectrum	1700 MWe, thermal spectrum
Net efficiency	44%
Coolant inlet and outlet temperatures and pressure	280°C/510°C/25 MPa
Average power density	~100 MWth/m^3
Reference fuel	UO_2 with austenitic or ferritic-martensitic stainless steel, or Ni-alloy cladding
Fuel structural materials cladding structural materials	Advanced high-strength metal alloys are needed
Burnup / Damage	~45 GWD/MTHM; 10–30 dpa
Safety approach	Similar to ALWRs

B6. Very-High-Temperature-Reactor (VHTR) System [2, 3]

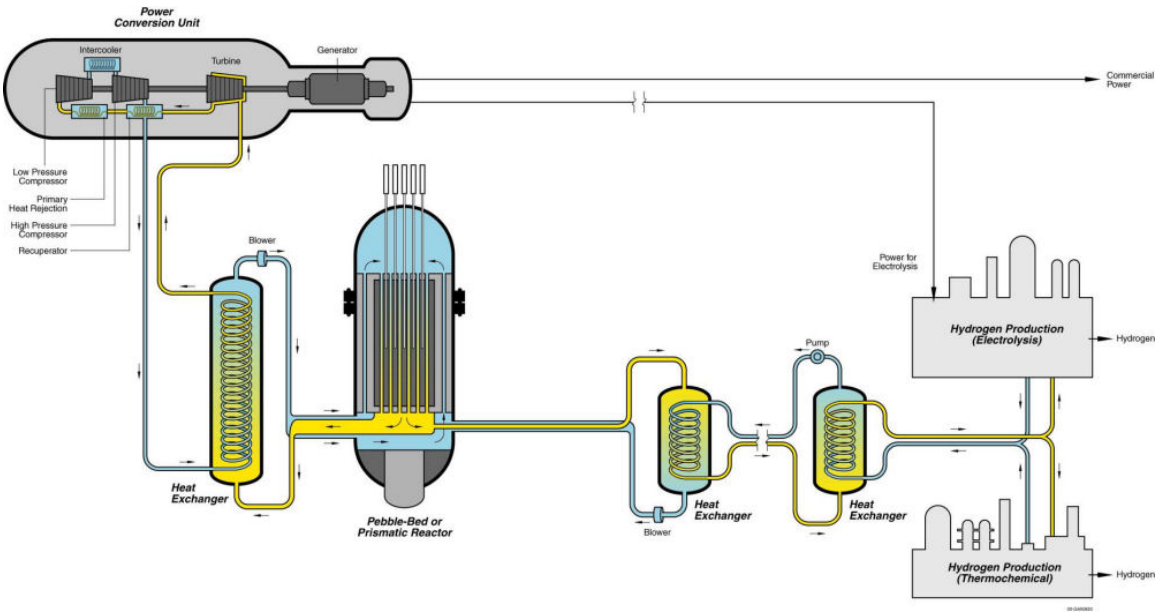

Reactor Parameters	Reference Value
Reactor power	600 MWth
Coolant inlet/outlet temperature	640/1000°C
Core inlet/outlet pressure	Dependent on process
Helium mass flow rate	320 kg/s
Average power density	6–10 MWth/m^3
Reference fuel compound	ZrC-coated particles in blocks, pins or pebbles
Net plant efficiency	>50%

APPENDIX C

CANDIDATE MATERIALS –NGNP PROGRAM

C1. Summary of materials considered for NGNP applications [2]

				Structural Materials	
System	**Spectrum, T_{outlet}**	**Fuel**	**Cladding**	**In-core**	**Out-of-core**
GFR	Fast, 850°C	MC/SiC	Ceramic	Refractory metals and alloys, Ceramics, ODSVessel: F-M	Primary Circuit: Ni-based superalloys 32Ni-25Cr-20 Fe-12.5W-0.05C Ni-23Cr-18W-0.2 CF-M w/ thermal barriersTurbine: Ni-based alloys or ODS
LFR	Fast, 550°C and Fast, 800°C	MN	High-Si F-M, Ceramics, or refractory alloys		High-Si austenitics, ceramics, or refractory alloys
MSR	Thermal, 700–800°C	Salt	Not Applicable	Ceramics, refractory metals, High-Mo Ni-base alloys (e.g., INOR-8), Graphite, Hastelloy N	High-Mo Ni-base alloys (e.g., INOR-8)
SFR (Metal)	Fast, 520°C	U-Pu-Zr	F-M (HT9 or ODS)	F-M ducts 316SS grid plate	Ferritics, austenitics
SFR (MOX)	Fast, 550°C	MOX	ODS	F-M ducts 316SS grid plate	Ferritics, austenitics
SCWR-Thermal	Thermal, 550°C	UO_2	F-M(12Cr, 9Cr, etc.) (Fe-35Ni-25Cr-0.3Ti) Incoloy 800, ODS Inconel 690, 625, & 718	Same as cladding options	F-M
SCWR -Fast	Fast, 550°C	MOX, Dispersion	F-M (12Cr, 9Cr, etc.) (Fe-35Ni-25Cr-0.3Ti) Incoloy 800, ODS Inconel 690 & 625	Same as cladding options	F-M
VHTR	Thermal, 1000°C	TRISO UOC in Graphite Compacts; ZrC coating	ZrC coating and surrounding graphite	Graphites PyC, SiC, ZrC Vessel: F-M	Primary Circuit: Ni-based superalloys 32Ni-25Cr-20Fe-12.5 W-0.05CNi-23Cr-18 W-0.2CF-M w/ thermal barriers Turbine: Ni-based alloys or ODS

Abbreviations:
F-M: Ferritic-martensitic stainless steels (typically 9 to 12 wt% Cr)
ODS: Oxide dispersion-strengthened steels (typically ferritic-martensitic)
MN: (U,Pu)
MC: (U,Pu)C
MOX: $(U,Pu)O_2$

APPENDIX D

PROPERTIES OF NICKEL-BASE SUPERALLOYS FOR NGNP PROGRAM

D1. Chemical Composition [72-74]

Alloy	Ni[a]	Cr	Mo	W	Co	Fe	C	Mn	Al	B	Ti
230	57	22	2	14	5*	3	0.1	0.5	0.3	0.015	----
617	54	22	9	---	12.5	1	0.07	---	1.2	---	0.3
800H	35	23	---	----	---	bal	0.10	1.5	0.6	---	0.6

[a]Balance, * Maximum

D2. Physical Properties [72-74]

Property	Alloy 230	Alloy 617	Alloy 800H
Density (g/cc)	8.97	8.36	8
Melting Range (^{o}C)	1290-1375	1332-1377	1350-1400
Electrical Resistivity (μohm-cm)	125	122	93
Modulus of Elasticity (GPa)	211	211	197
Thermal Conductivity (W/m-K)	8.9	16.1	11.6
Specific Heat (J/kg-K)	397	419	500

D3. Mechanical Properties [72-74]

Test Temperature (^{o}C)	0.2% Offset YS (MPa)			UTS (MPa)			%Elongation		
	Alloy 230	Alloy 617	Alloy 800H	Alloy 230	Alloy 617	Alloy 800H	Alloy 230	Alloy 617	Alloy 800H
Room	395	367	200	860	779	531	50	52	52
540	275	254	114	705	618	438	53	67	51
650	275	239	102	675	627	384	55	67	50
760	275	245	99	605	483	223	53	92	78
870	255	207	80	435	286	128	65	99	120
980	145	111	61	240	155	70	83	93	120

APPENDIX E

TENSILE PROPERTIES DATA

E1. Data for Specimens Set 1

Temperature (^{o}C)	YS, ksi (MPa)	UTS, ksi (MPa)	%El	%RA
Room Temperature	62 (434)	131 (896)	15.1	40.7
150	44 (317)	112 (765)	15.6	43.0
300	41 (283)	108 (751)	16.5	44.0
500	40 (276)	103 (710)	17.3	53.2
750	40 (276)	71 (489)	18.5	61.4
850	36 (255)	43 (296)	20.0	76.1
950	20 (145)	25 (172)	23.0	83.8

E2. Data for Specimens Set 2

Temperature (^{o}C)	YS, ksi (MPa)	UTS, ksi (MPa)	%El	%RA
Room Temperature	63 (434)	132 (896)	15.0	40.6
150	47 (317)	111 (765)	15.7	42.9
300	41 (283)	109 (751)	16.4	44.0
500	40 (276)	105 (710)	17.2	53.4
750	40 (276)	72 (489)	18.4	61.4
850	39 (255)	43 (296)	20.1	76.0
950	22 (145)	25 (172)	23.0	83.7

APPENDIX F

CREEP TESTING- ADDITIONAL INFORMATION

F1. WinCCS Data Acquisition System

The WinCCS data acquisition system is a state-of-the-art system that offers a number of unique features for enhanced control and monitoring of long-term creep, creep-rupture,and stress-rupture testing. WinCCS delivers an industry-leading array of test control, data acquisition, archiving, analysis, and reporting features. From frame setup, accessory calibration, and specification creation to report generation and data graphing, menu-driven displays lead the operator through easy-to-follow steps that add up to accurate, repeatable, and fully-documented test results.

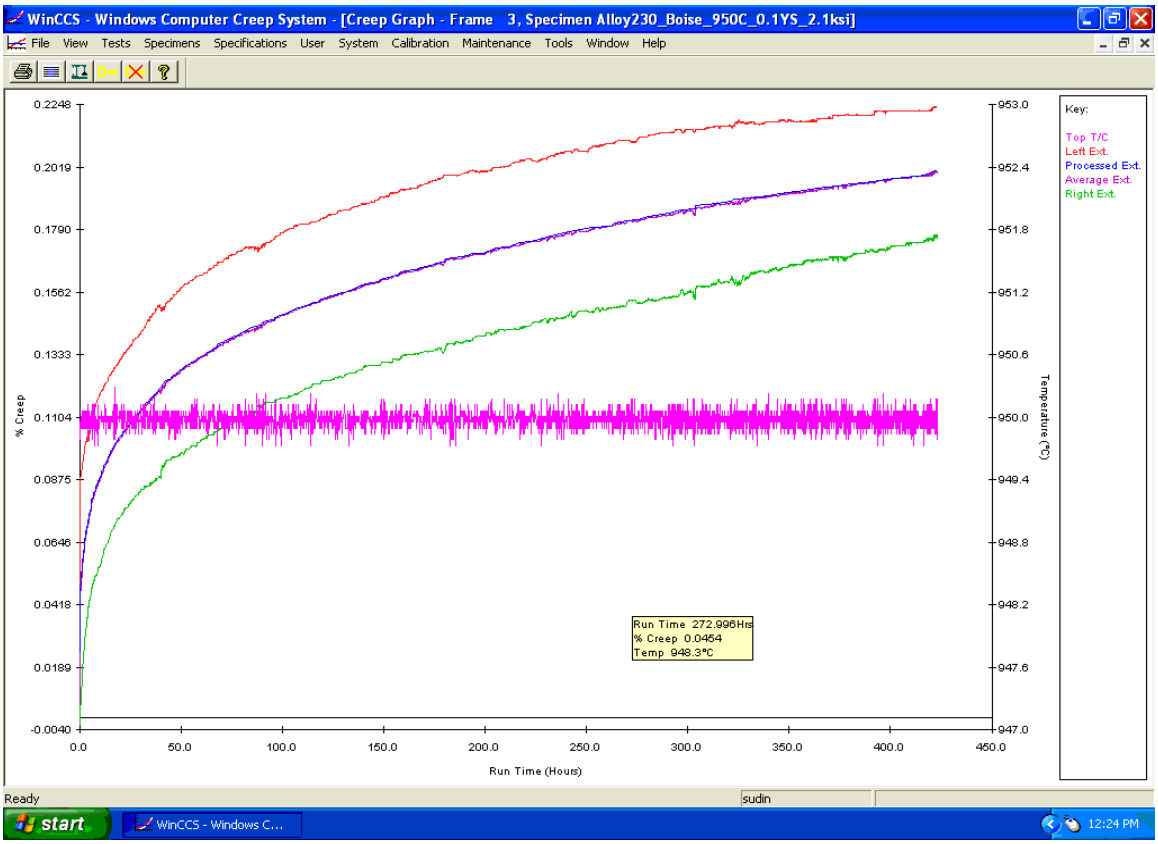

F2. Duplicate Creep Curves – 0.10YS Applied Stress

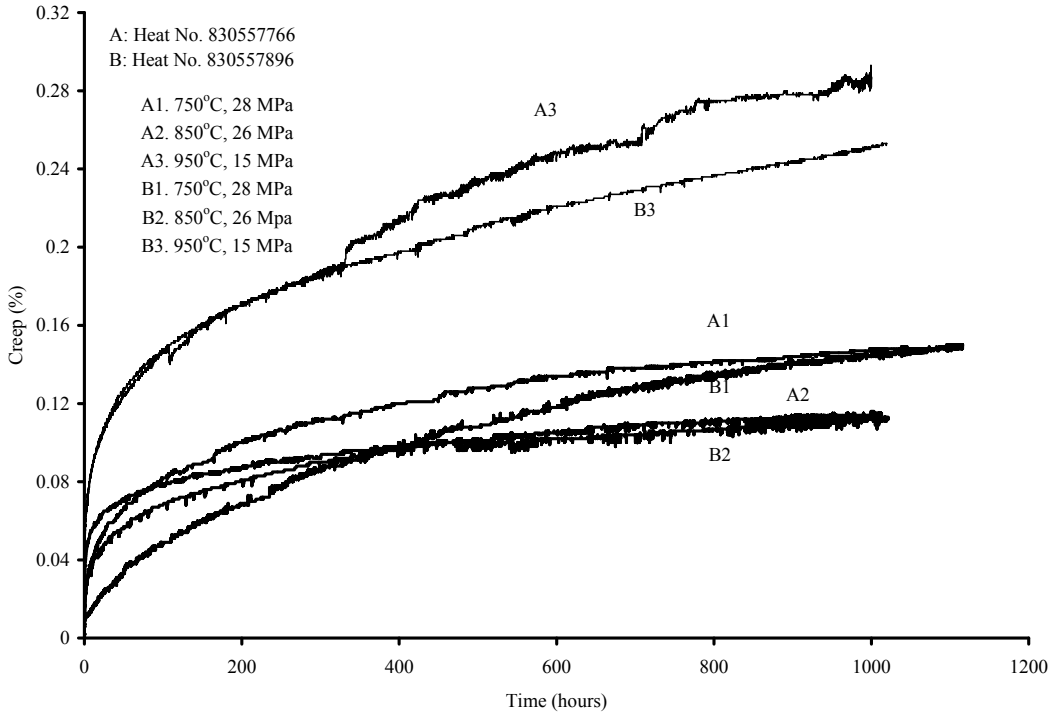

F3. Duplicate Creep Curves – 0.25YS Applied Stress

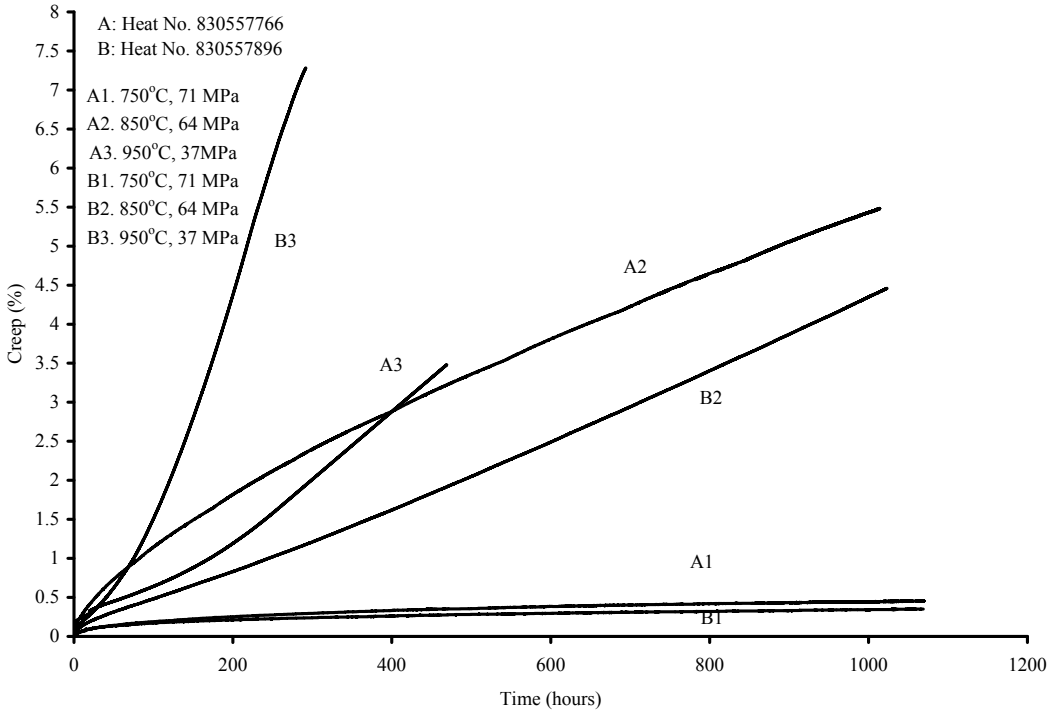

APPENDIX G

STRESS RUPTURE TESTING- ADDITIONAL INFORMATION

G1. WinCCS Stress Monitoring Window

The stress rupture testing aims at maintaining a constant stress during testing. The WinCCs system allows monitoring the stress condition during testing through the following window.

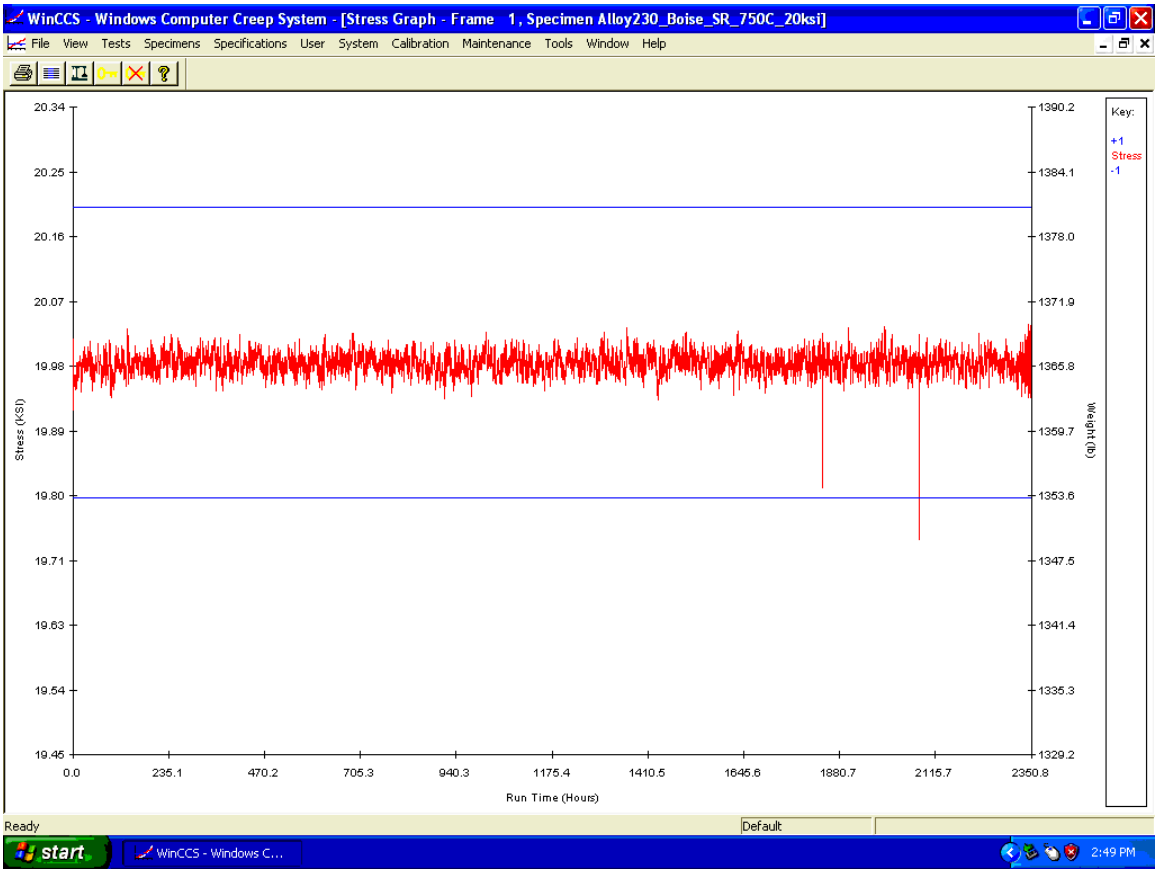

G2. Raw Data – Stress Rupture Testing

Temperature (K)	Stress (ksi)	Rupture Time (Hours)
1023	20	2180
1023	20	2165
1023	20	2170
1023	25	495
1023	25	505
1023	25	496
1023	30	120
1023	30	115
1023	30	119
1073	20	260
1073	20	262
1073	20	261
1073	25	60
1073	25	57
1073	25	58
1073	30	23
1073	30	22
1073	30	22
1123	20	45
1123	20	48
1123	20	48
1123	25	15
1123	25	14
1123	25	14
1123	30	3
1123	30	3
1123	30	4

G3. Multiple Linear Regression (MLR) using MS-EXCEL LINEST Function

The LINEST function in MS-EXCEL calculates the statistics for a straight line by using the "least squares" method that best fits a set of data. The LINEST function can also be combined with other functions to calculate the statistics for other types of models

that are linear in the unknown parameters, including polynomial, logarithmic, exponential, and power series. Because this function returns an array of values, it must be entered as an array formula.

The equation for a line is:

y = mx + b or

y = m1x1 + m2x2 + ... + b (if there are multiple ranges of x-values)

where the dependent y-value is a function of the independent x-values. The m-values are coefficients corresponding to each x-value, and b is a constant value. Note that y, x, and m can be vectors. The array that LINEST returns is {mn, mn-1,..., m1, b}. LINEST can also return additional regression statistics.

Syntax: LINEST(known_y's, known_x's, const, stats)

Known_y's is the set of y-values you already know in the relationship y = mx + b. If the array known_y's is in a single column, then each column of known_x's is interpreted as a separate variable. If the array known_y's is in a single row, then each row of known_x's is interpreted as a separate variable. Known_x's is an optional set of x-values that you may already know in the relationship y = mx + b. The array known_x's can include one or more sets of variables. If only one variable is used, known_y's and known_x's can be ranges of any shape, as long as they have equal dimensions. If more than one variable is used, known_y's must be a vector (that is, a range with a height of one row or a width of one column). If known_x's is omitted, it is assumed to be the array {1, 2, 3, ...} that is the same size as known_y's. Const is a logical value specifying whether to force the constant b to equal 0. If const is TRUE or omitted, b is calculated normally. If const is FALSE, b is set equal to 0 and the m-values are adjusted to fit y = mx.

Stats is a logical value specifying whether to return additional regression statistics. If stats is TRUE, LINEST returns the additional regression statistics, so the returned array is $\{m_n,m_{n-1},...,m_1,b;se_n,se_{n-1},...,se_1,se_b;r_2,se_y;F,df;ss_{reg},ss_{resid}\}$. If stats is FALSE or omitted, LINEST returns only the m-coefficients and the constant b.

The following illustration shows the order in which the additional regression statistics are returned.

	A	B	C	D	E	F
1	m_n	m_{n-1}	.....	m_2	m_1	b
2	se_n	se_{n-1}	.....	se_2	se_1	se_b
3	r_2	se_v				
4	F	d_f				
5	ss_{reg}	ss_{resid}				

The additional regression statistics are as follows.

Statistic	Description
$se_1,se_2,...,se_n$	The standard error values for the coefficients m_1, m_2... m_n.
se_b	The standard error value for the constant b (seb = #N/A when const is FALSE).
r_2	The coefficient of determination. Compares estimated and actual y-values, and ranges in value from 0 to 1. If it is 1, there is a perfect correlation in the sample — there is no difference between the estimated y-value and the actual y-value. At the other extreme, if the coefficient of determination is 0, the regression equation is not helpful in predicting a y-value. For information about how r2 is calculated, see "Remarks" later in this topic.
se_y	The standard error for the y estimate.
F	The F statistics or the F-observed value. Use the F statistic to determine whether the observed relationship between the dependent and independent

	variables occurs by chance.
df	The degrees of freedom. Use the degrees of freedom to help you find F-critical values in a statistical table. Compare the values you find in the table to the F statistic returned by LINEST to determine a confidence level for the model. For information about how df is calculated, see "Remarks" later in this topic. Example 4 below shows use of F and df.
ss_{reg}	The regression sum of squares.
ss_{resid}	The residual sum of squares. For information about how ss_{reg} and ss_{resid} are calculated, see "Remarks" later in this topic.

G4. Regression Statistics for MLR Performed for MCM Analysis with A = 0.0278

	E	D	C	B	R2	R1
1	0.00183	-0.3585	0	-31418	0.00515	12.0288
2	0.00204	0.10241	0	22505.5	0.01965	1.25342
3	0.99628	0.12521	#N/A	#N/A	#N/A	#N/A
4	1474.36	22	#N/A	#N/A	#N/A	#N/A
5	92.4624	0.34492	#N/A	#N/A	#N/A	#N/A

G5. Regression Statistics for MLR Performed for MCM Analysis with A = 0

	E	D	C	B	R2	R1
1	0.00192	-0.3637	0	-73901	-0.0278	12.1044
2	0.00218	0.10909	0	26850.2	0.02338	1.33509
3	0.99578	0.13339	#N/A	#N/A	#N/A	#N/A
4	1298.59	22	#N/A	#N/A	#N/A	#N/A
5	92.4159	0.39142	#N/A	#N/A	#N/A	#N/A

G6. Regression Statistics for MLR Performed for MCM Analysis with A = -0.036

	E	D	C	B	R2	R1
1	0.00207	-0.3738	0	-165629	-0.1004	12.271
2	0.00296	0.14846	0	43650.4	0.03783	1.81657
3	0.99219	0.18152	#N/A	#N/A	#N/A	#N/A
4	698.684	22	#N/A	#N/A	#N/A	#N/A
5	92.0824	0.72487	#N/A	#N/A	#N/A	#N/A

APPENDIX H

CREEP-FATIGUE TESTING – ADDITIONAL INFORMATIONS

H1. Pure Fatigue Triangular Waveform

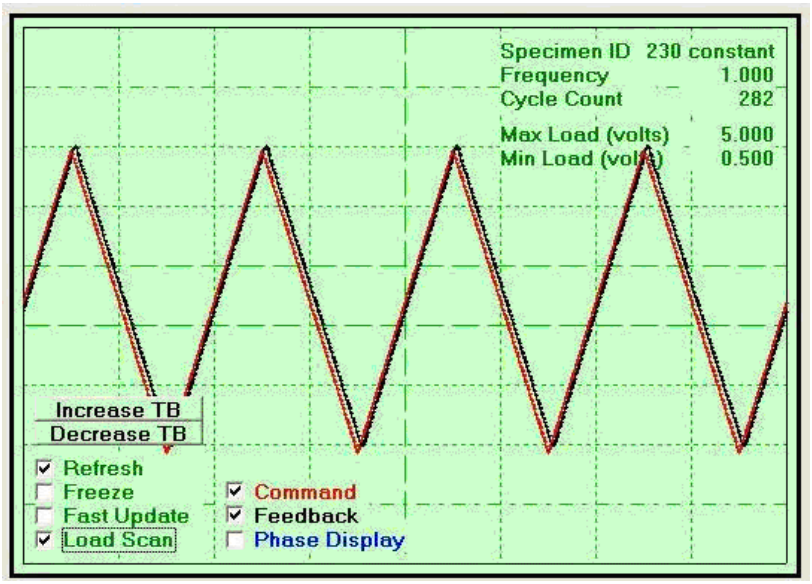

H2. Hold Time Imposed on the Pure Fatigue Triangular Waveform

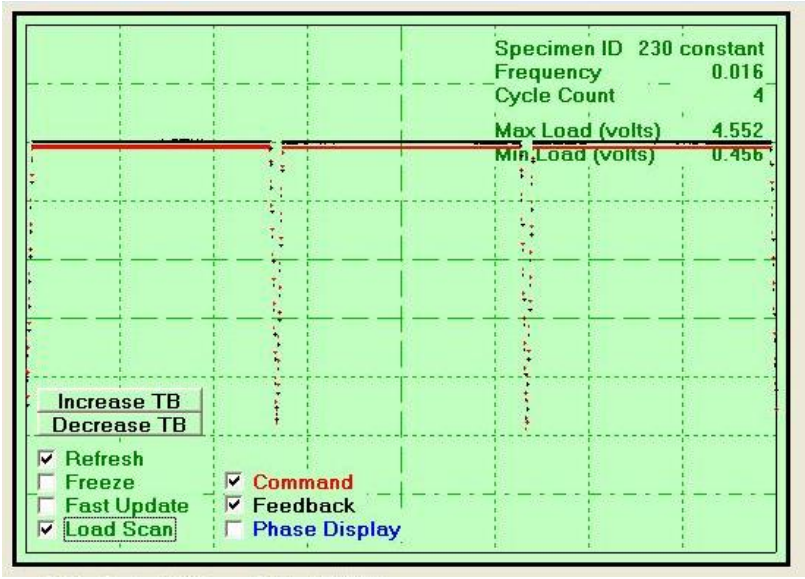

APPENDIX I

ADDITIONAL MICROGRAPHS – OPTICAL

I1 Optical Micrographs of Creep-Fatigue Tested Specimens at 700 ^{o}C.

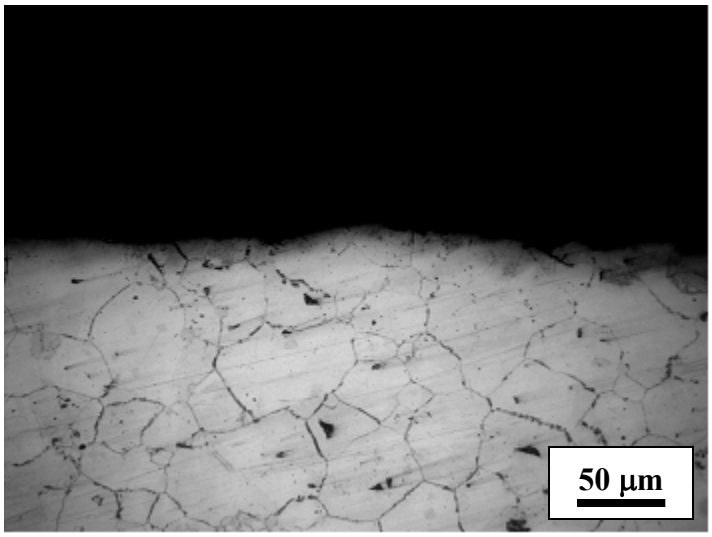

I1 (a) 700^{o}C, No Hold

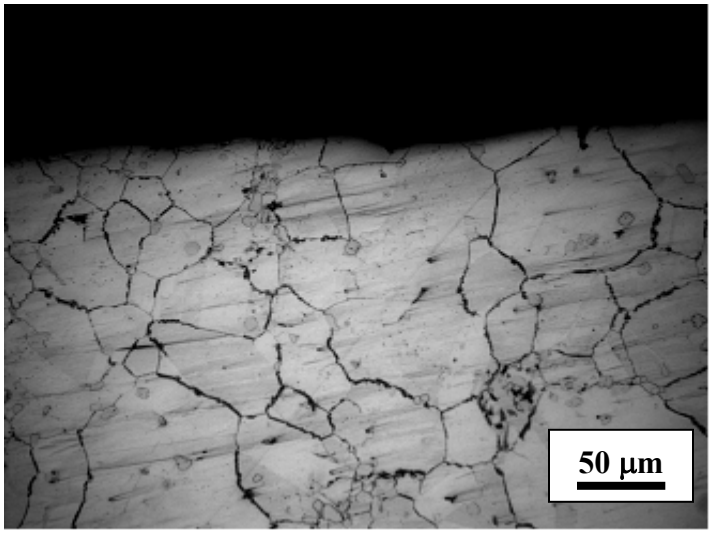

I1 (b) 700^{o}C, Hold Time = 60 sec

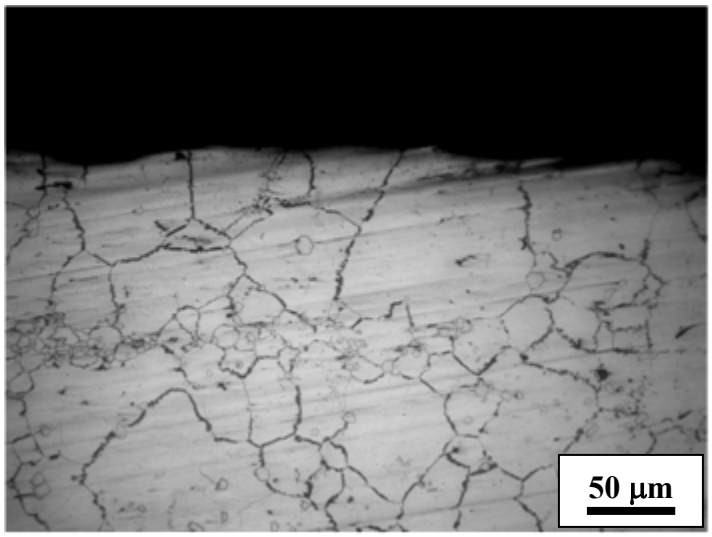

I1(c) 700^{o}C, Hold Time = 120 sec

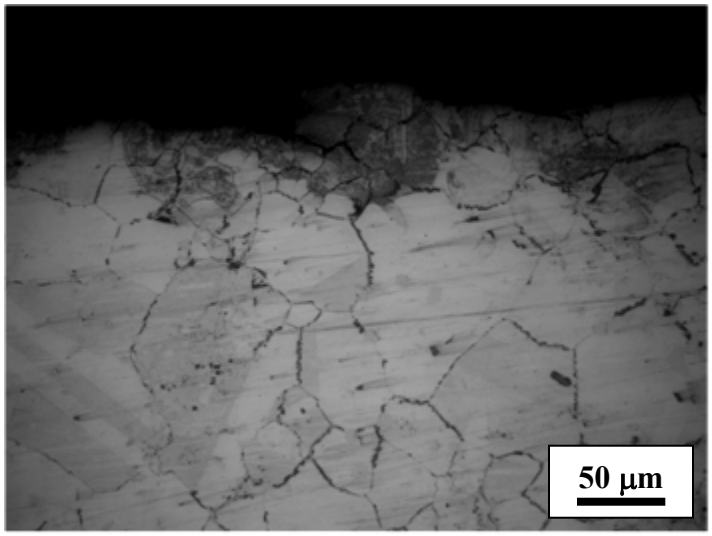

I1 (d) 700^{o}C, Hold Time = 600 sec

I2 Optical Micrographs of Creep-Fatigue Tested Specimens at 800 ^{o}C.

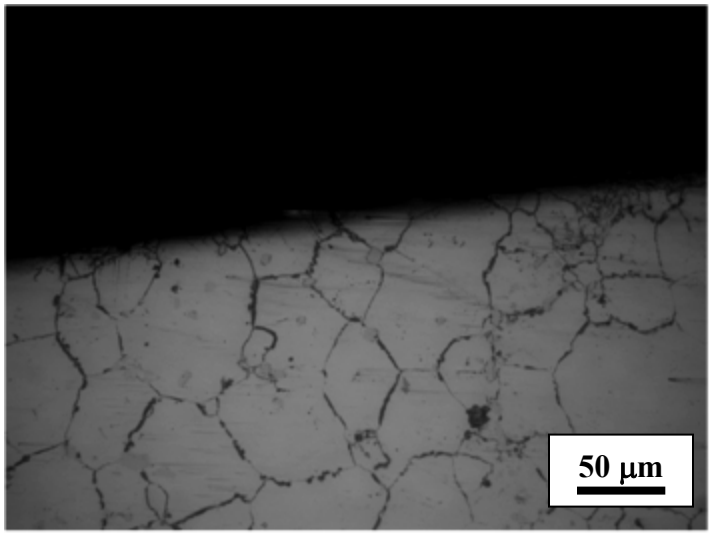

I2 (a) 800^{o}C, No Hold

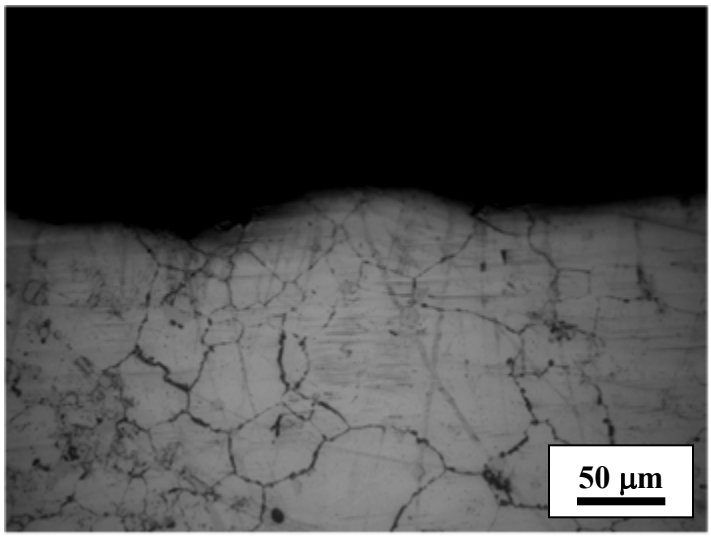

I2 (b) 800^{o}C, Hold Time = 60 sec

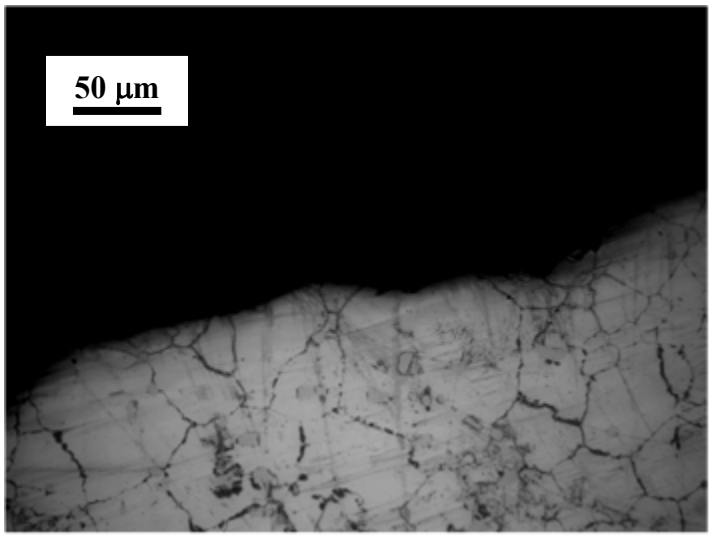

I2 (c) 800^{o}C, Hold Time = 120 sec

APPENDIX J

ADDITIONAL MICROGRAPHS – TEM

J1. TEM Image of Creep Tested Specimens at 750 ^{o}C-0.10YS

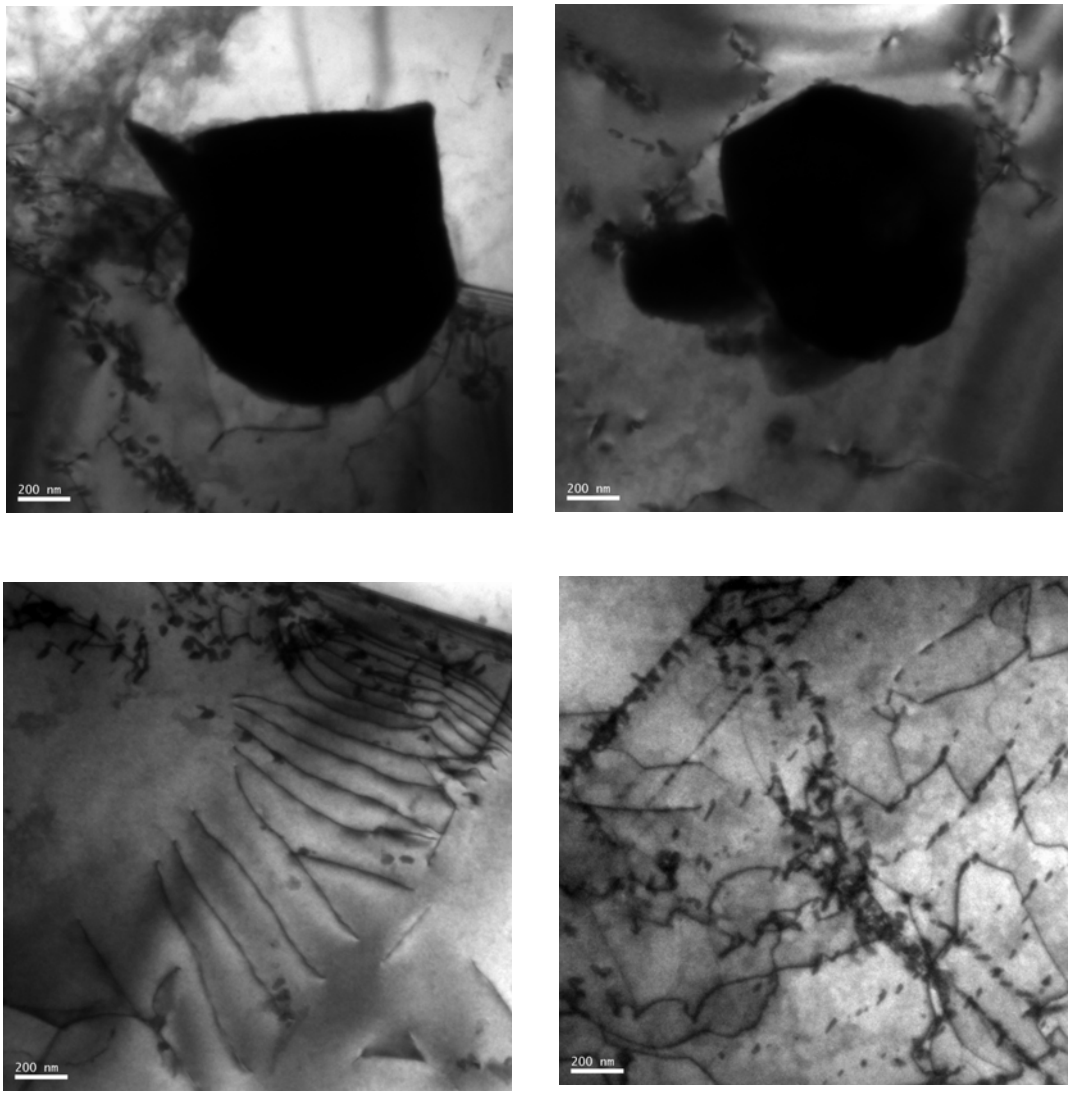

J2. STEM Image and EDX Spectra of Creep tested Specimens at 750 ^{o}C-0.10YS

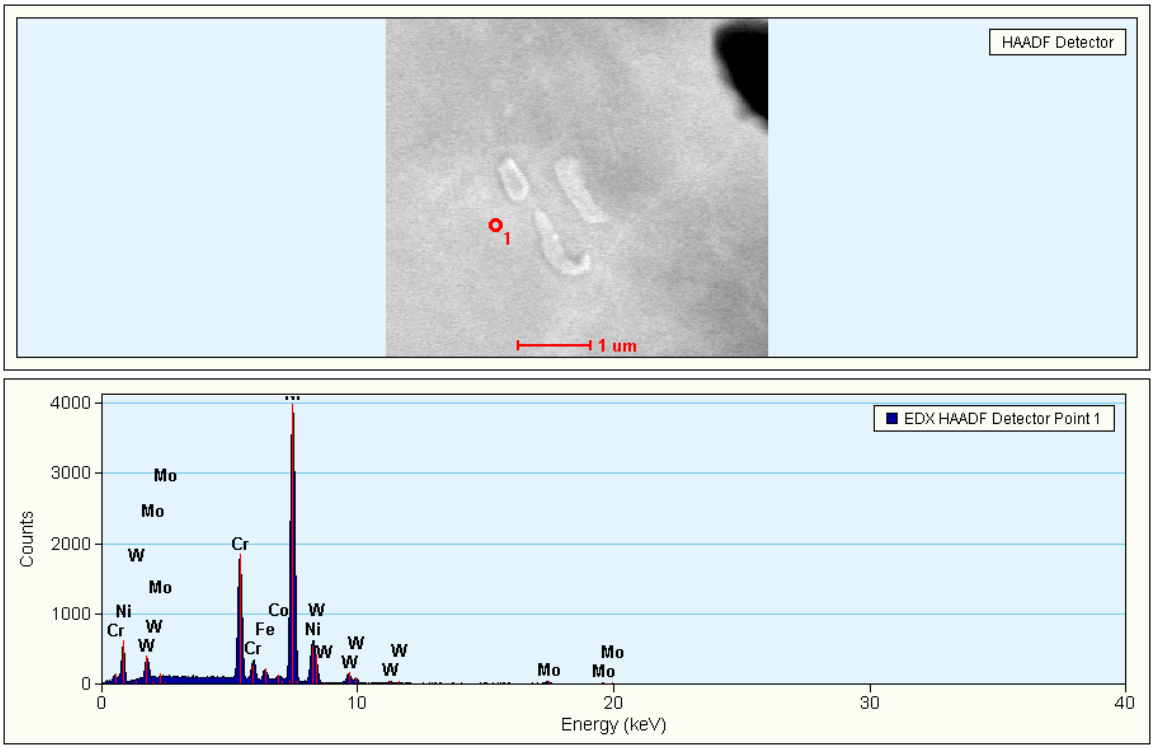

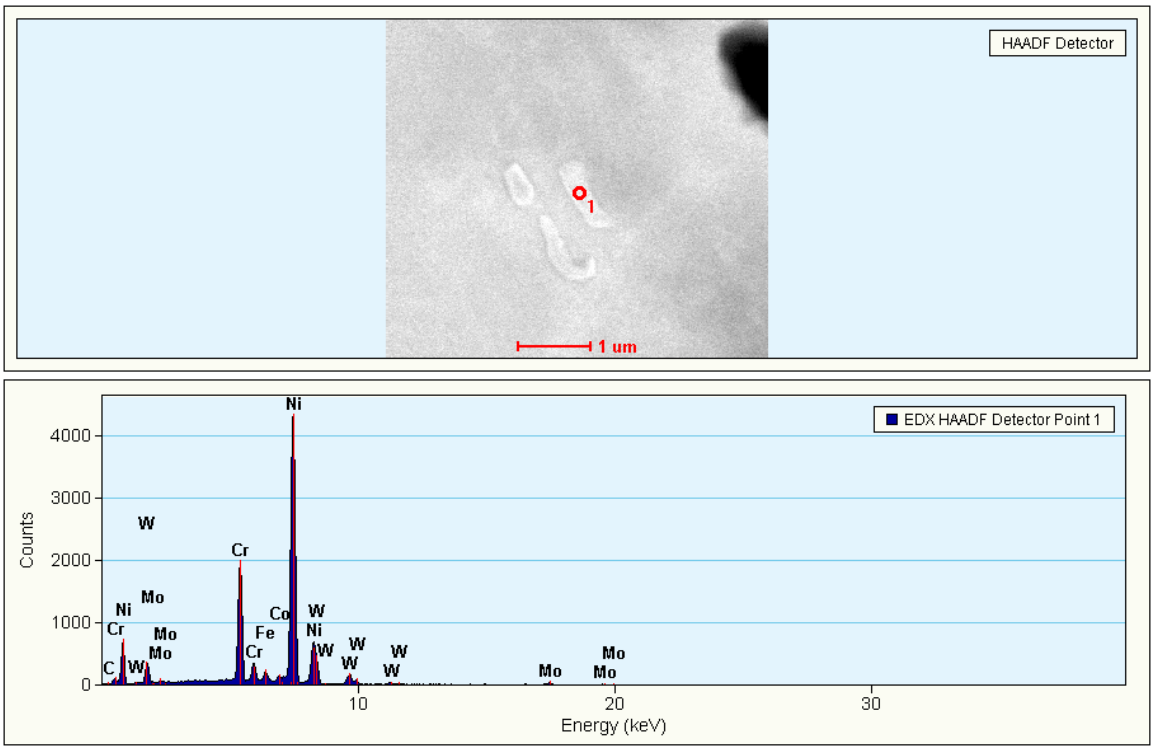

J3. TEM Image of Creep Tested Specimens at 850 ^{o}C-0.10YS

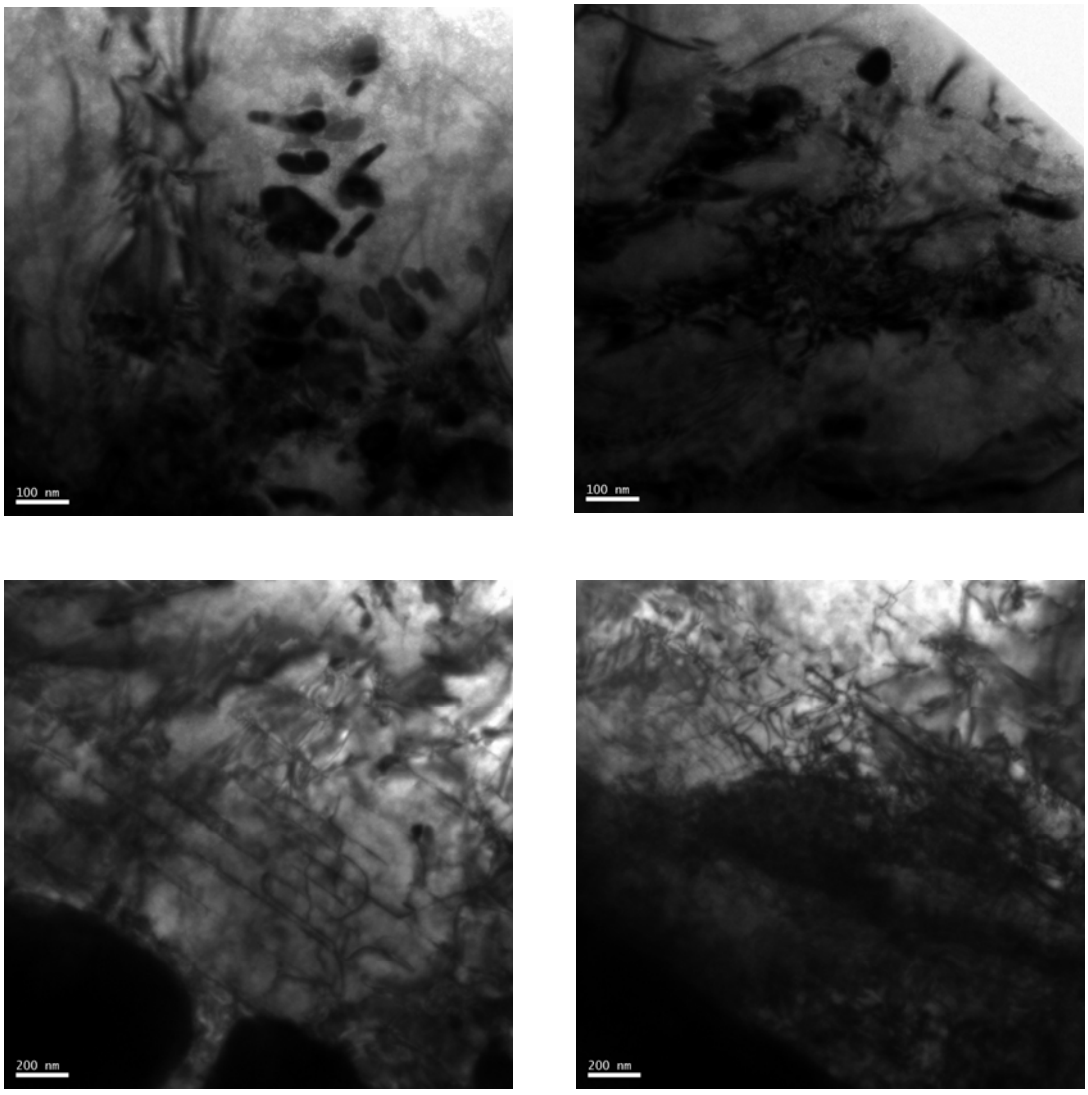

J4. STEM Image and EDX Spectra of Creep tested Specimens at 850 ^{o}C-0.10YS

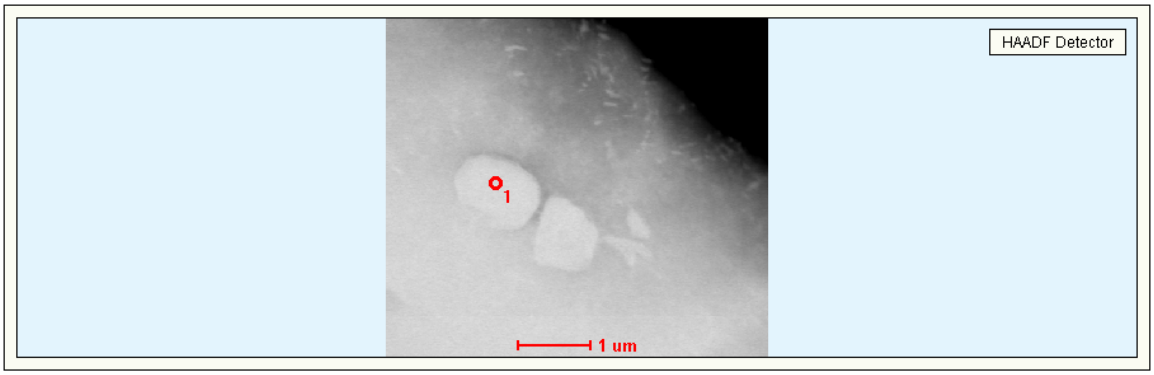

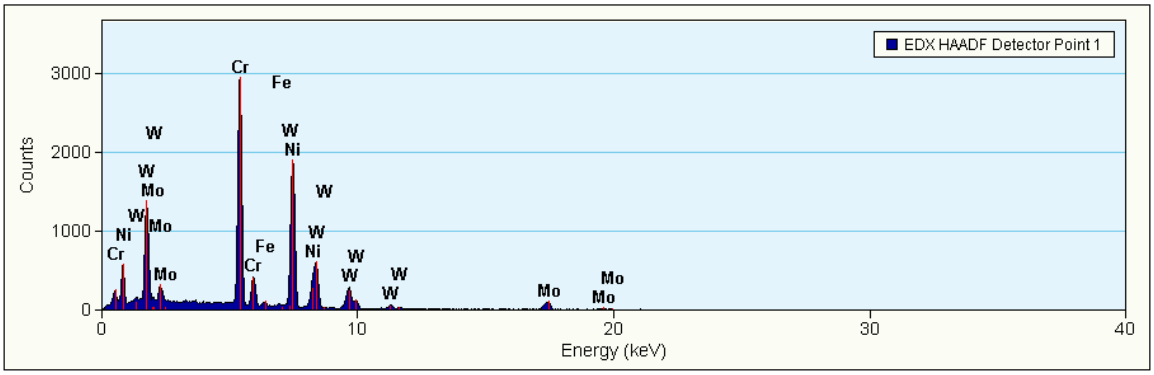

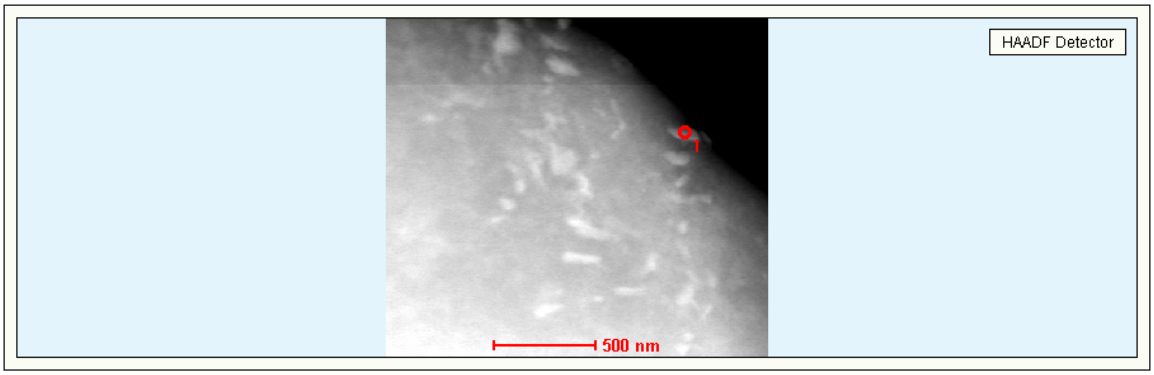

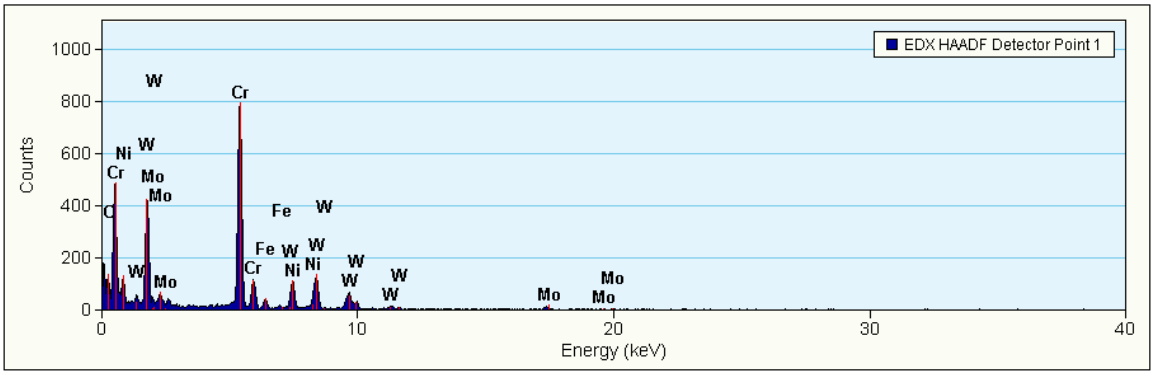

J5. TEM Image of Creep Tested Specimens at 950 ^{o}C-0.10YS

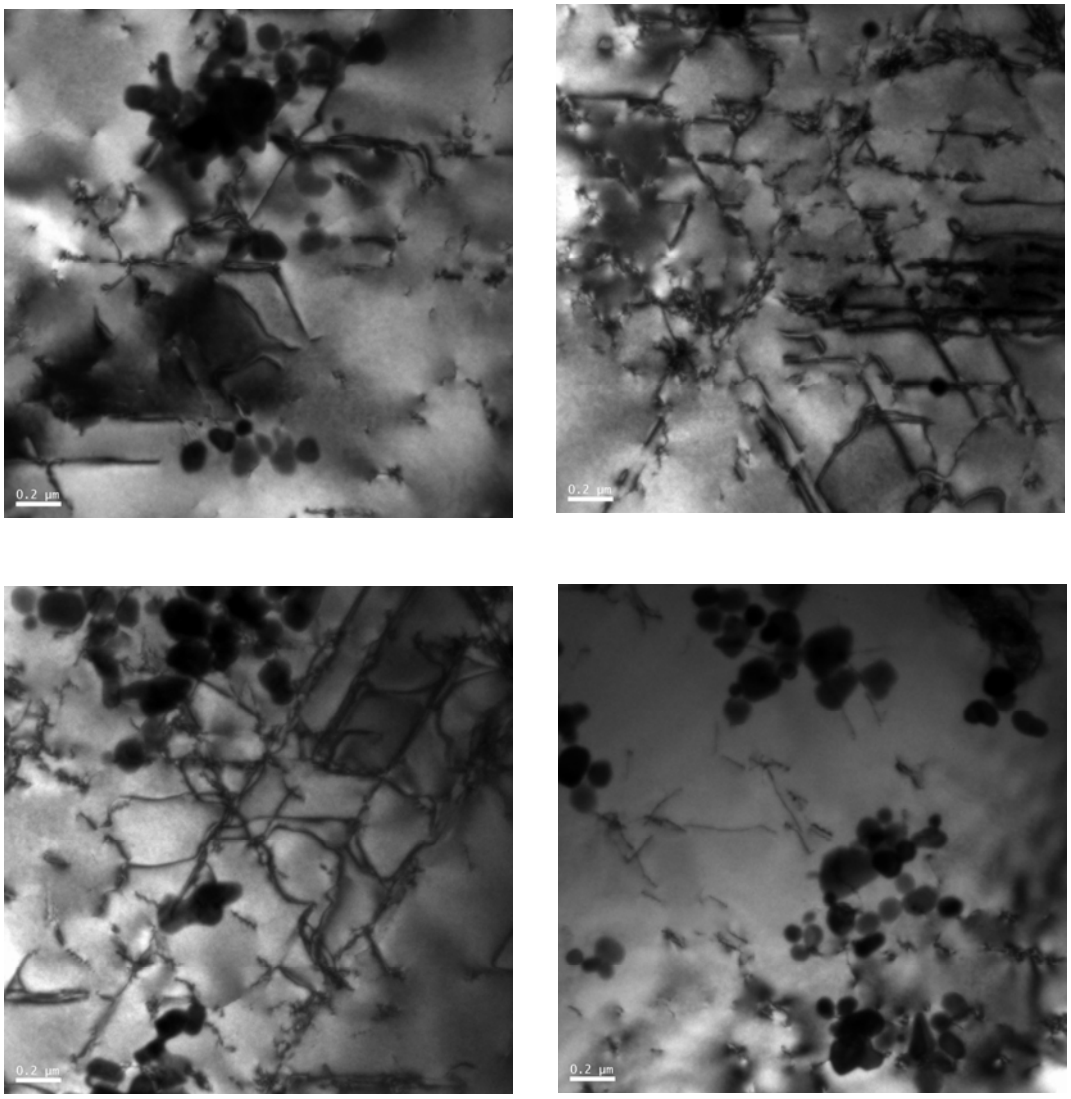

J6. STEM Image and EDX Spectra of Creep tested Specimens at 950 ^{o}C-0.10YS

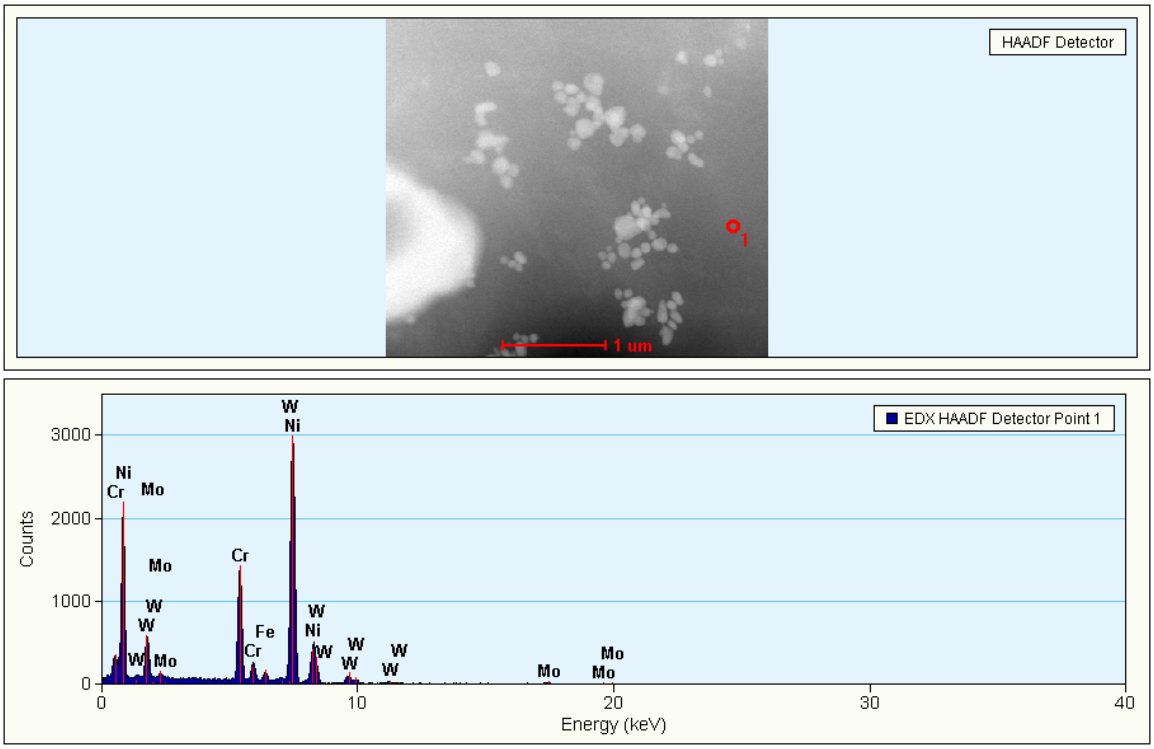

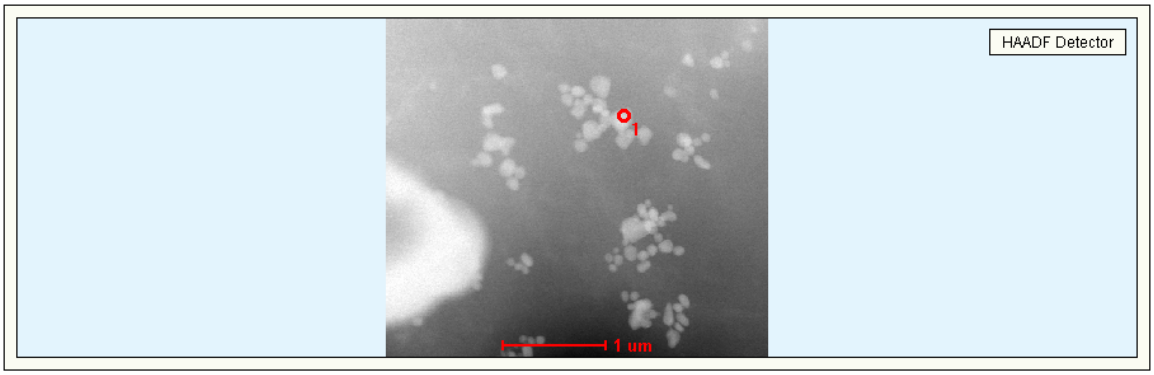

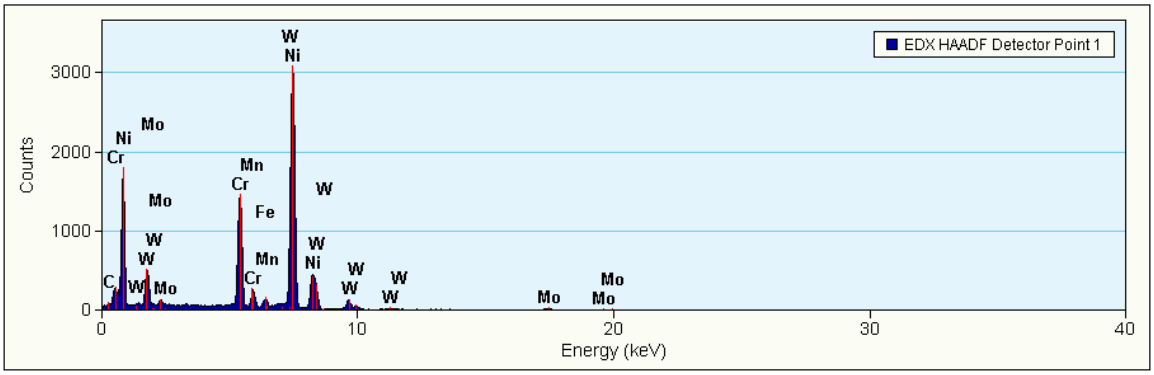

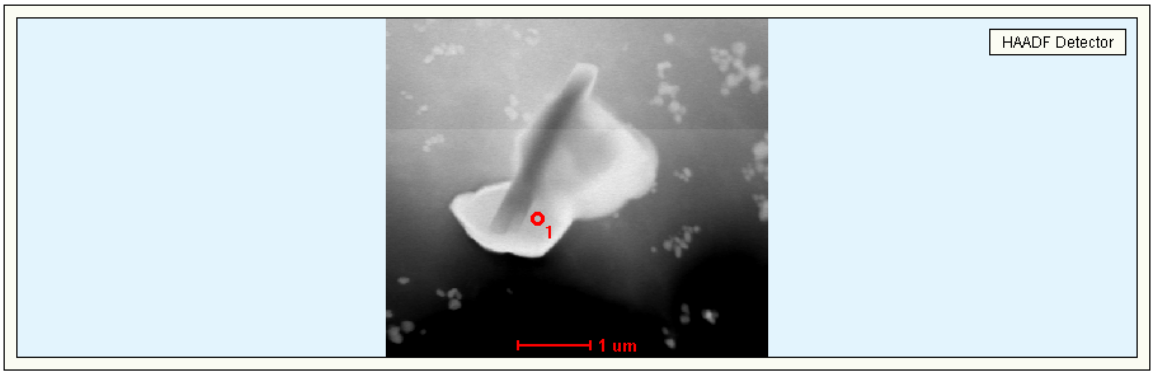
HAADF Detector
1
1 um

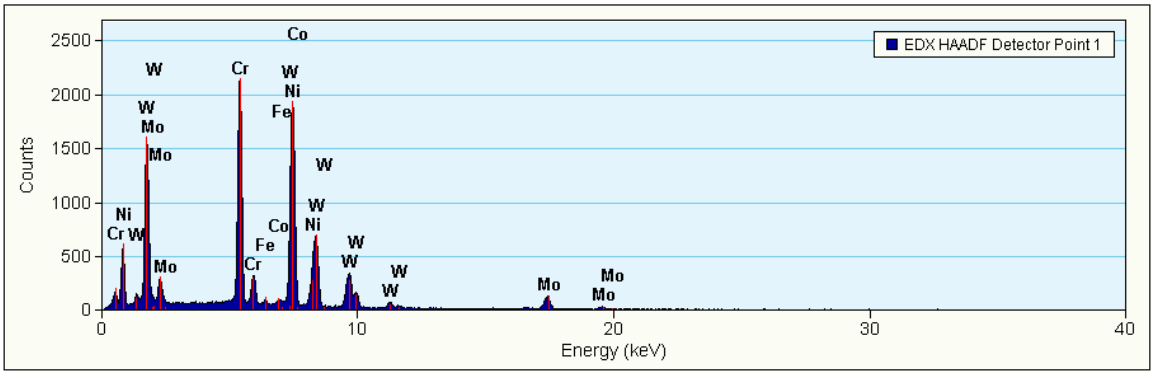
EDX HAADF Detector Point 1
Counts
Energy (keV)
0
500
1000
1500
2000
2500
10
20
30
40
Co
W
Cr
W
Ni
Fe
W
Mo
Mo
W
Ni
Cr
W
Co
Fe
Cr
Mo
W
W
W
Mo
Mo
Mo

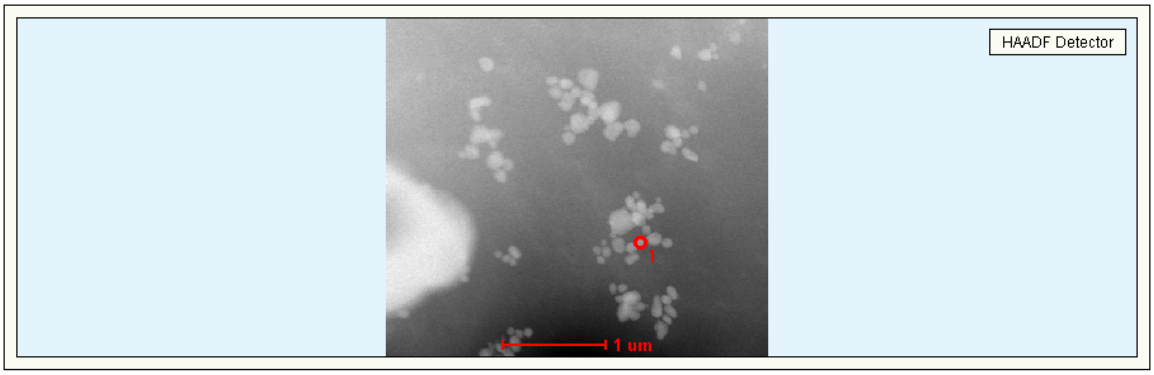
HAADF Detector
1
1 um

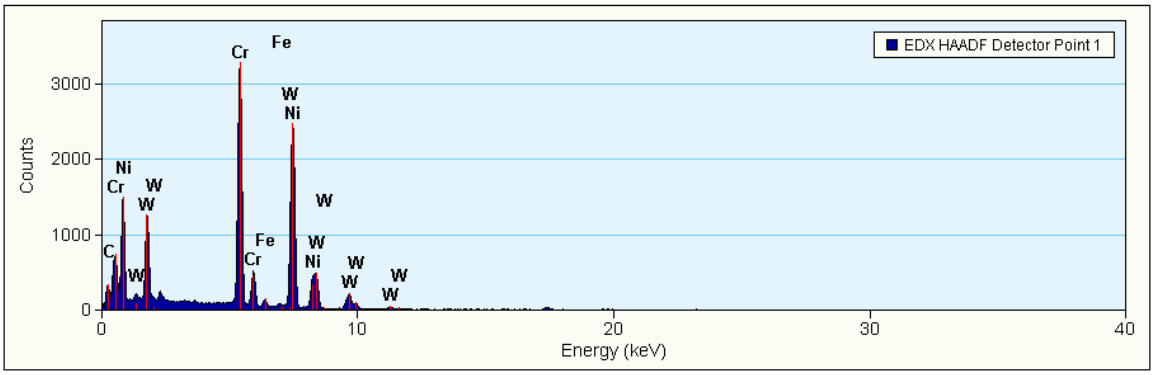
EDX HAADF Detector Point 1
Counts
Energy (keV)
0
1000
2000
3000
10
20
30
40
Cr
Fe
W
Ni
Ni
Cr
W
W
W
C
W
Fe
Cr
W
Ni
W
W
W
W

J7. TEM Image of Creep Tested Specimens at 750 ^{o}C-0.25YS

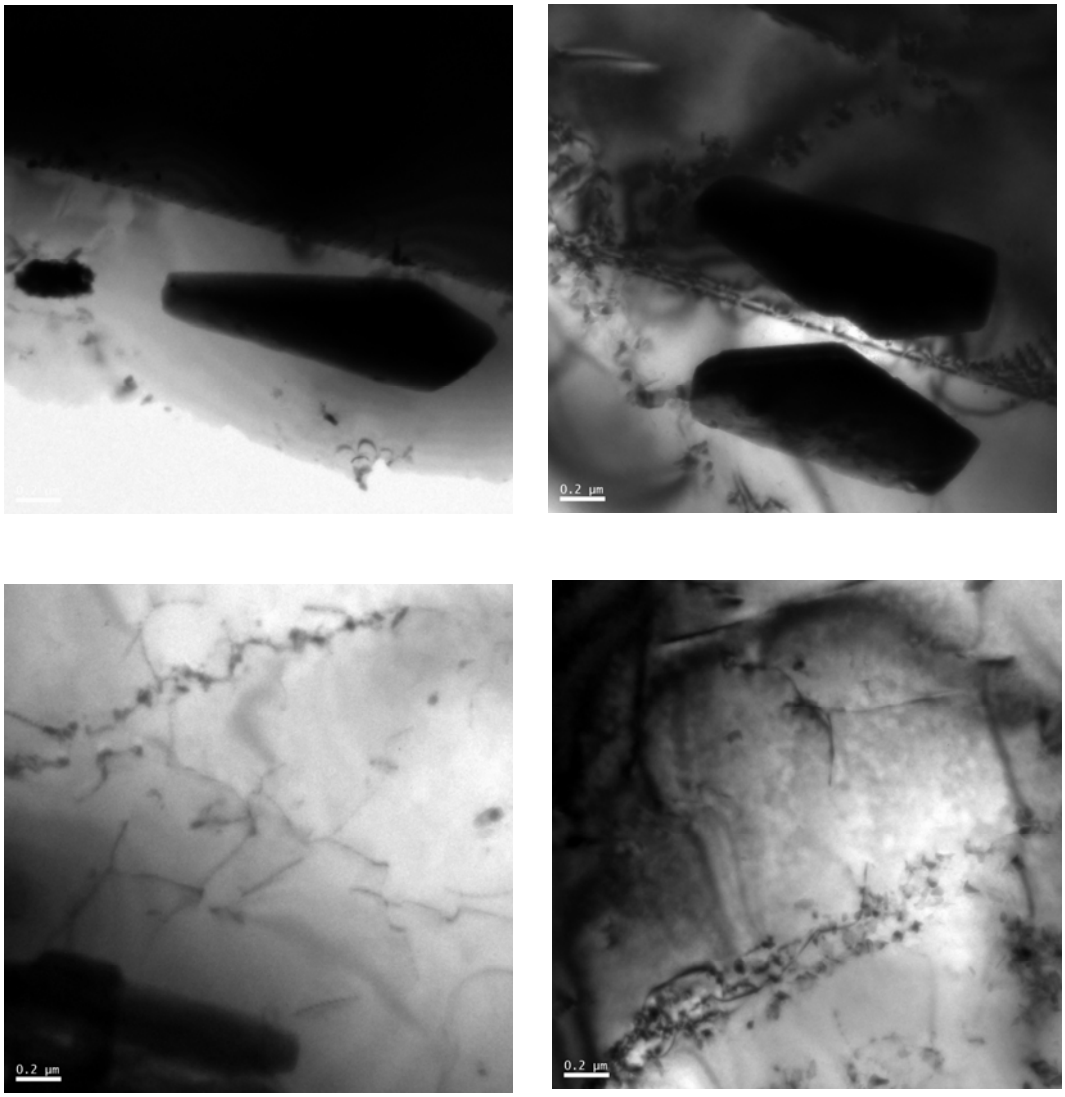

J8. STEM Image and EDX Spectra of Creep tested Specimens at 750 ^{o}C-0.25YS

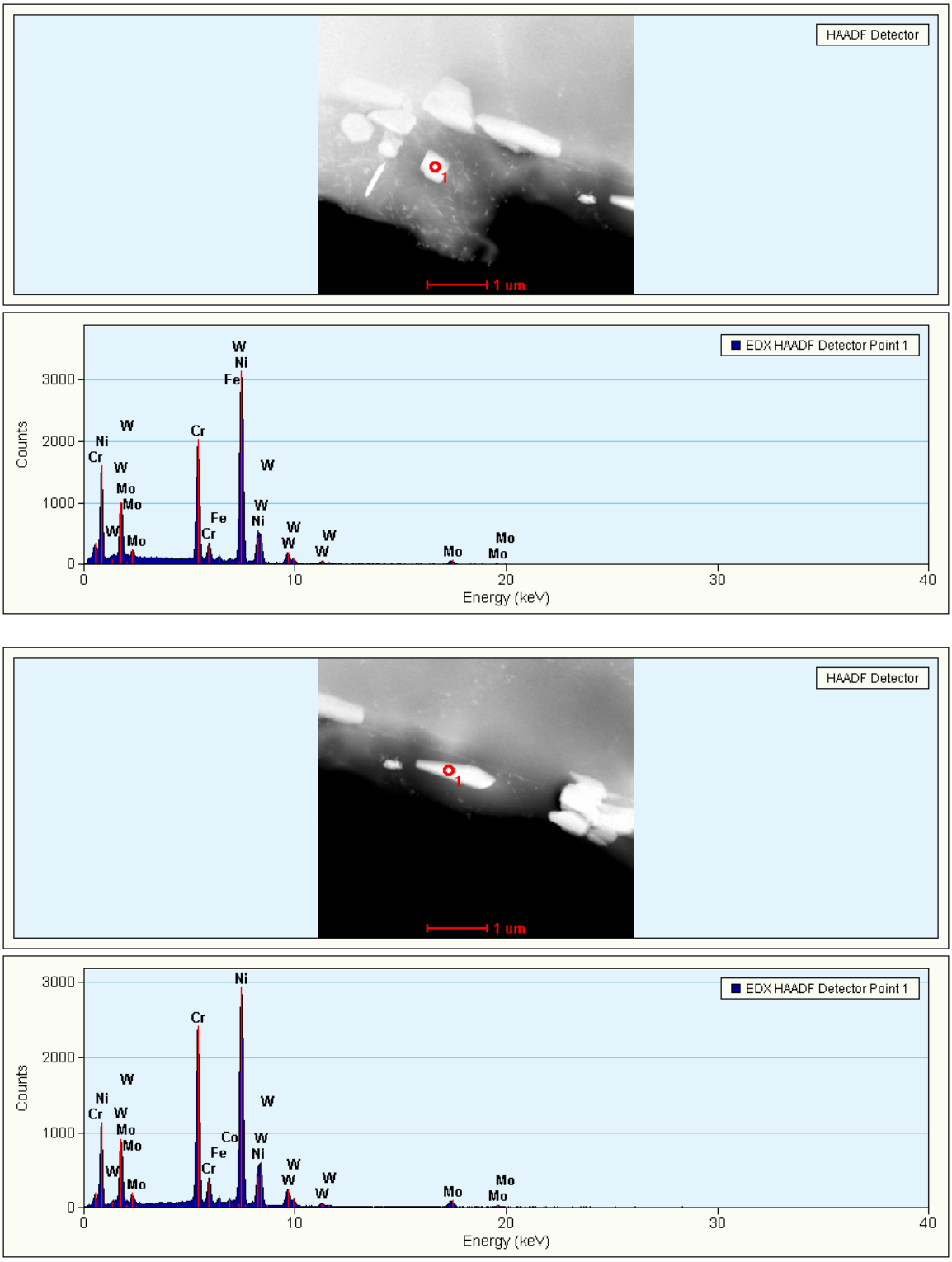

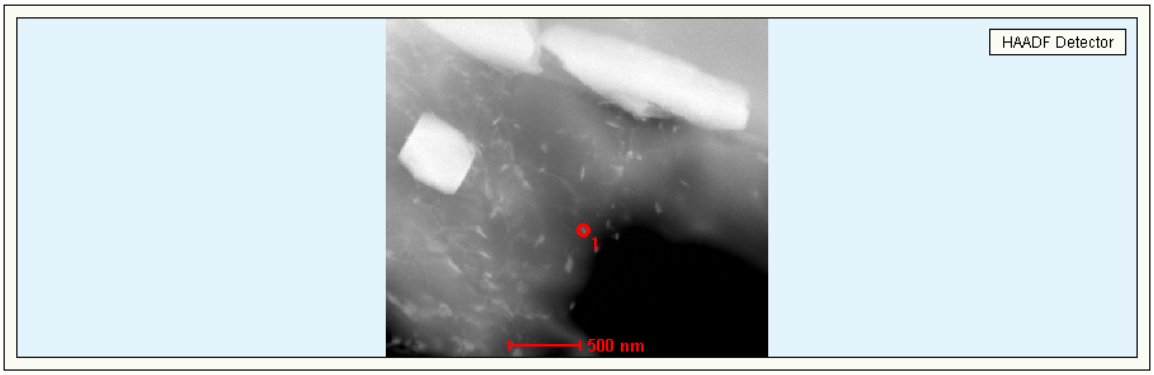
HAADF Detector
1
500 nm

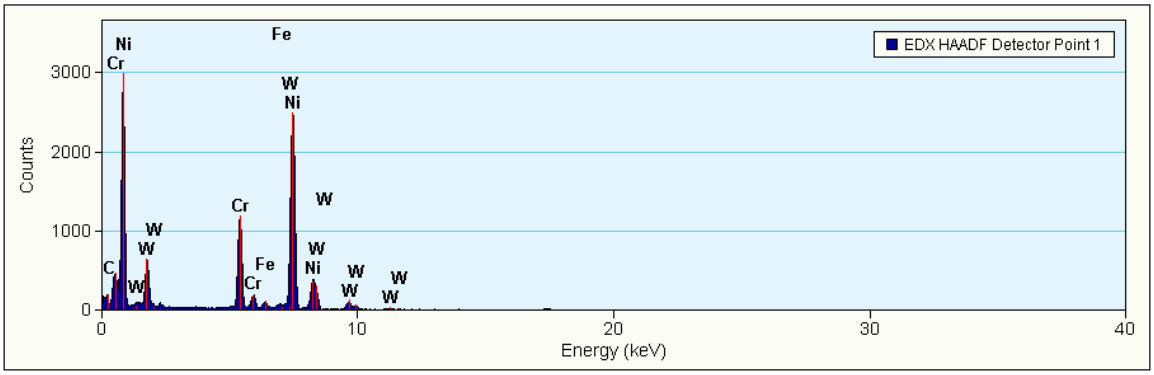
EDX HAADF Detector Point 1
Counts
Energy (keV)
Ni
Cr
Fe
W
C

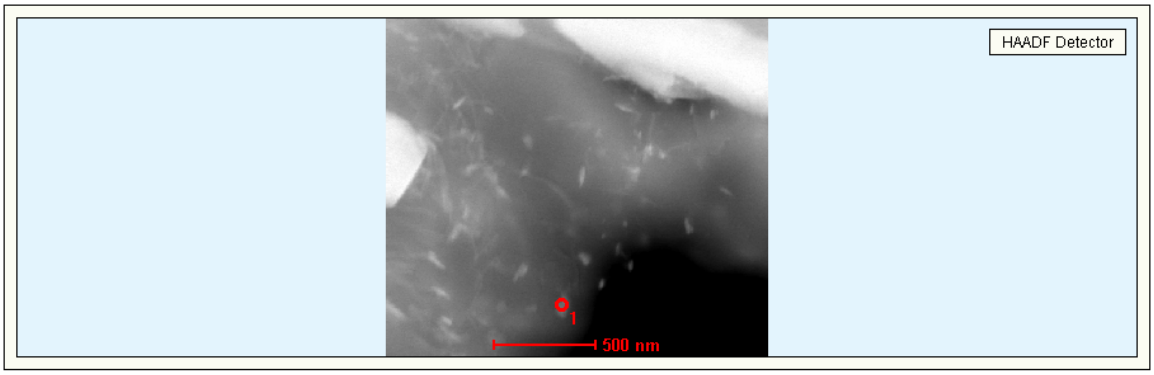
HAADF Detector
1
500 nm

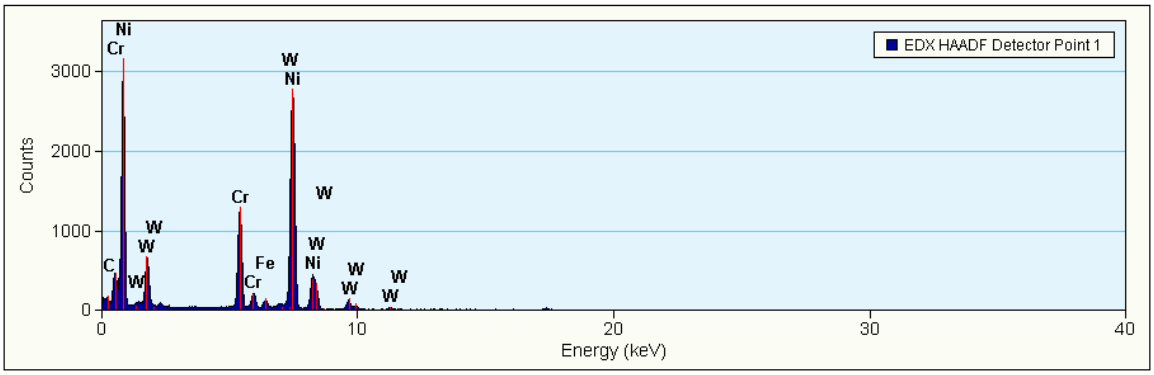
EDX HAADF Detector Point 1
Counts
Energy (keV)
Ni
Cr
W
Fe
C

J9. TEM Image of Creep Tested Specimens at 850 ^{o}C-0.25YS

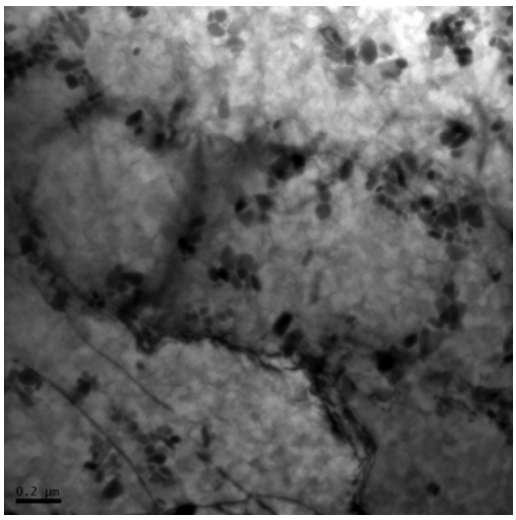

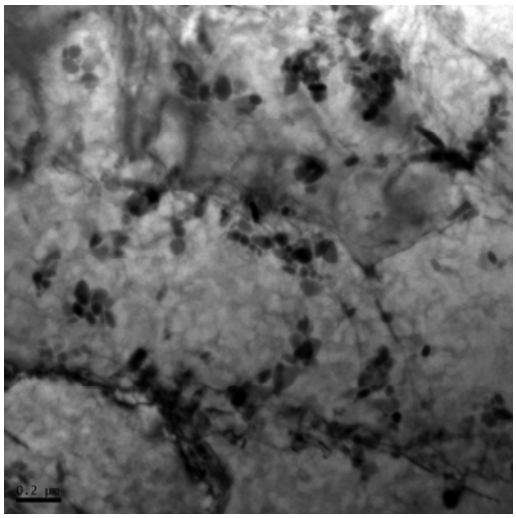

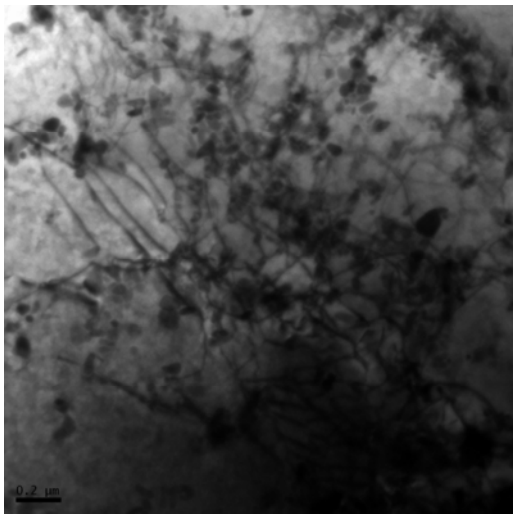

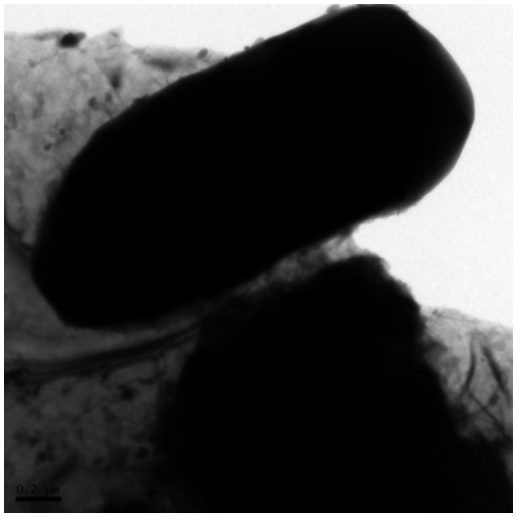

J10. STEM Image and EDX Spectra of Creep tested Specimens at 850 ^{o}C-0.25YS

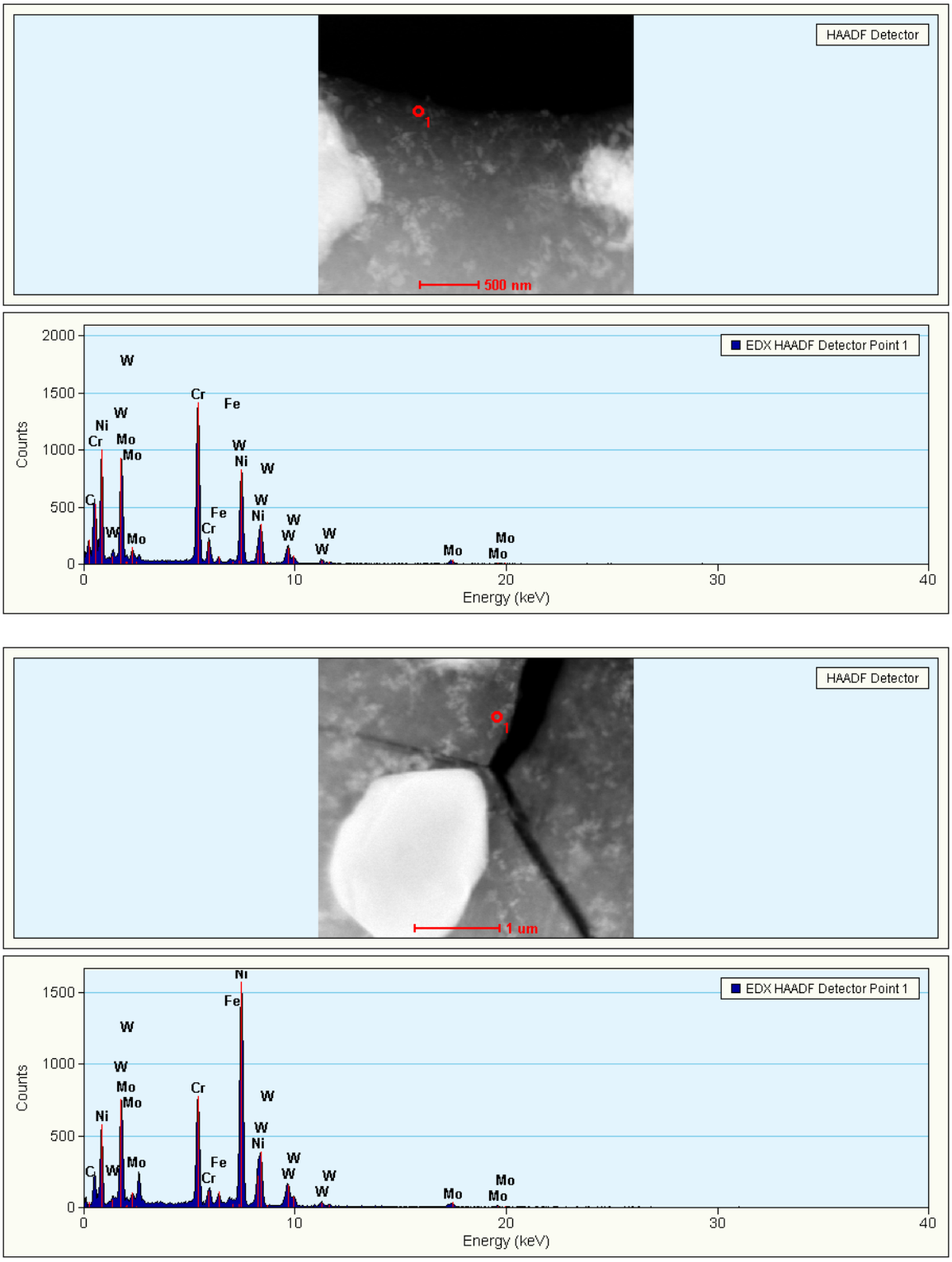

J11. TEM Image of Creep Tested Specimens at 950 ^{o}C-0.25YS

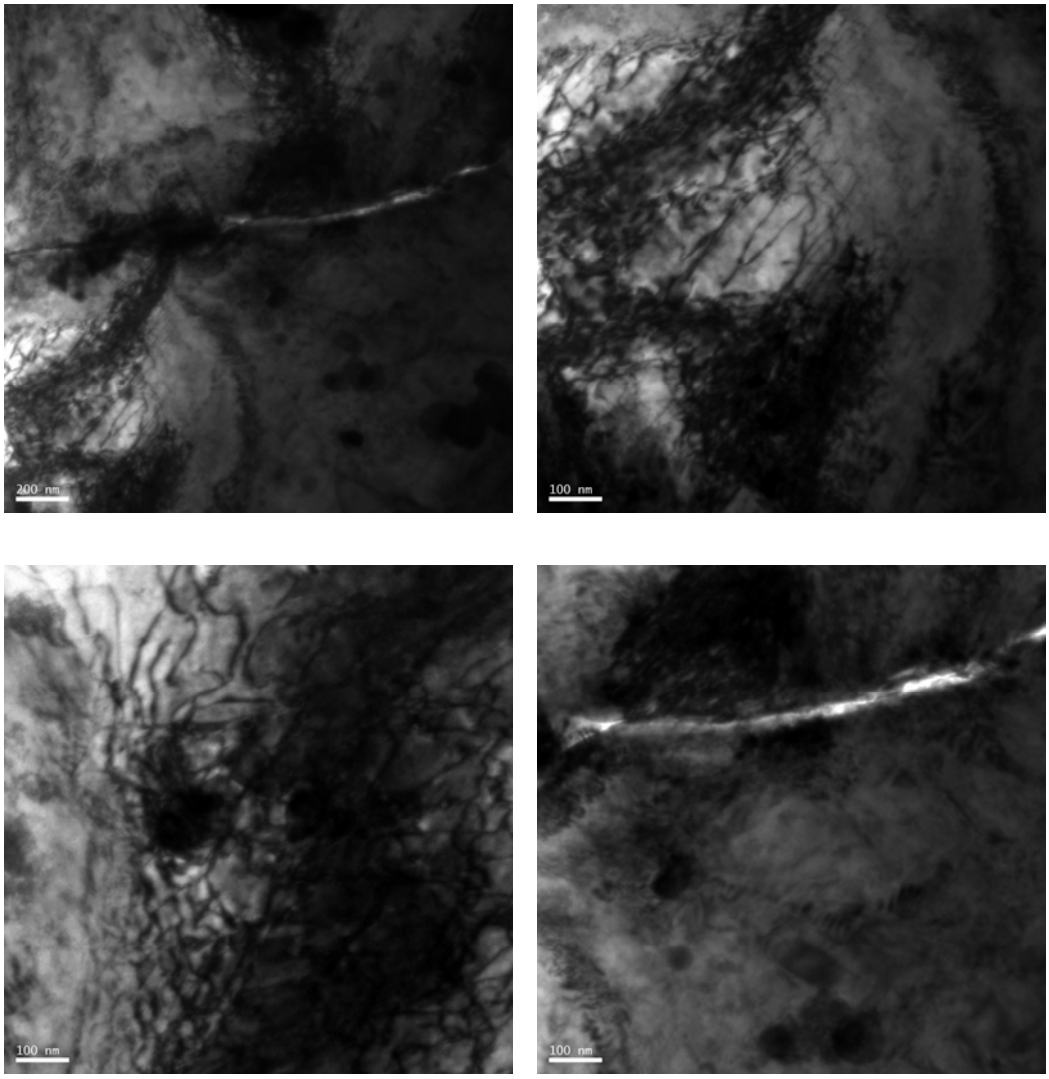

J10. STEM Image and EDX Spectra of Creep tested Specimens at 950 ^{o}C-0.25YS

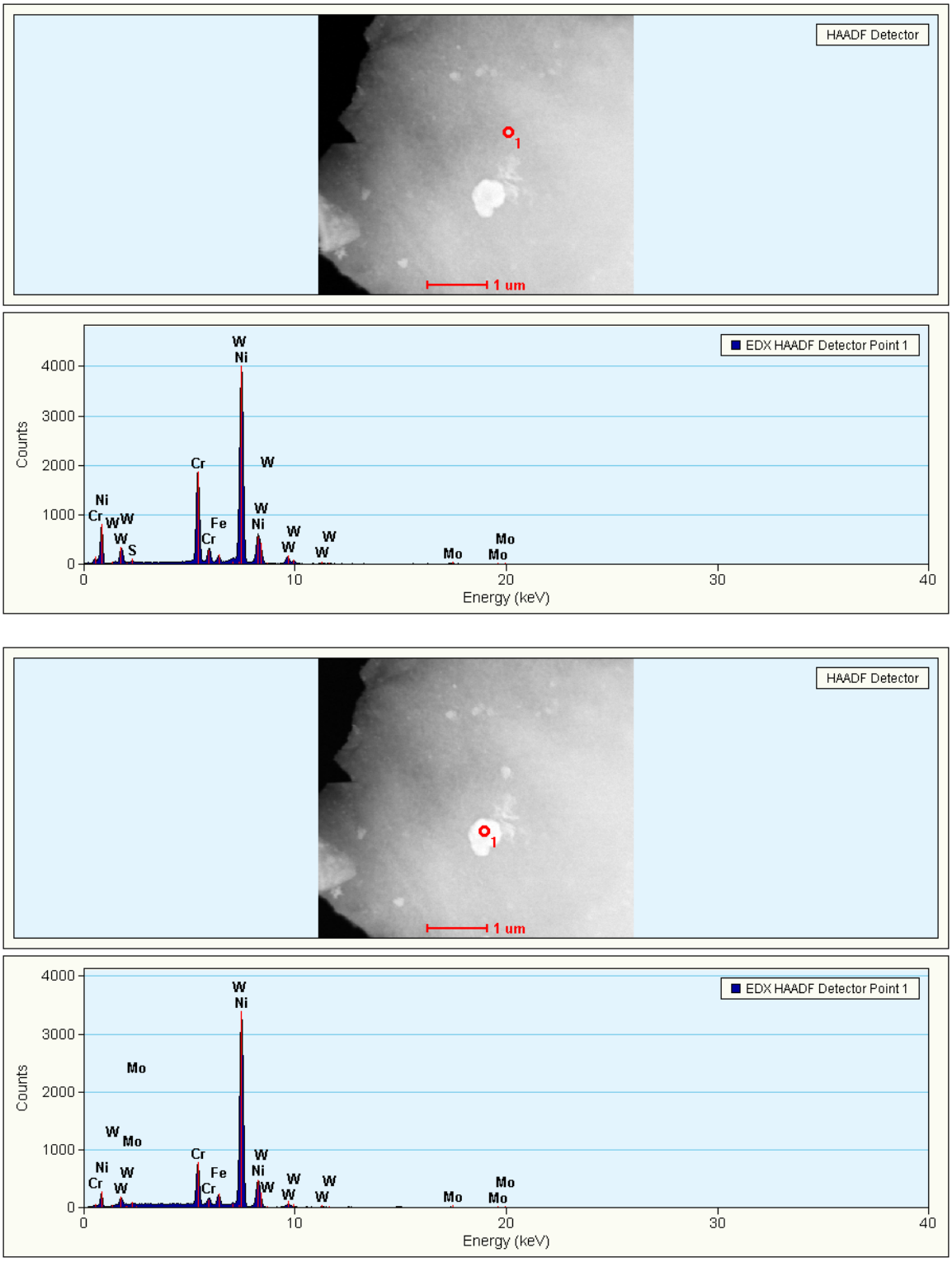

APPENDIX K

UNCERTAINITY ANALYSIS

A precise method of estimating uncertainty in experimental results of CGR testing has been presented by Georgsson [refs]. This method is applicable to tests conducted in load control mode at constant-amplitude (using the DCPD technique) and performed under uniaxial loading at ambient temperature.

The combined uncertainty in the results of this investigation was calculated by using the root sum squares equation, given below [75]. This uncertainty corresponds to plus or minus one standard deviation on the normal distribution law representing the studied quantity. This combined uncertainty has an associated confidence level of 68.27%.

$$U_c(y) = \sqrt{\sum_{i=1}^{N}\left[c_i u(x_i)\right]^2} \qquad \text{Equation K-1}$$

Where $U_c(y)$ = Combined uncertainty in the results

c_i = Sensitivity coefficient associated with x_i, usually = 1

The expanded uncertainty (U) was obtained by multiplying the combined uncertainty (U_c) by a coverage factor (k), the value of which was taken as 2 that corresponds to a confidence interval of 95.4% [75, 76]. It is to be noted that all uncertainty calculations in this section are based on a crack length of 0.9 mm for a CT specimen tested at ambient temperature and a load ratio of 0.1. However, this analysis can be applied to all other crack lengths.

K1 Uncertainty in Crack Length [U(a)]

Sample Calculation:

Standard deviation in crack length error due to PD-variation = S_{ea} = ±1.08 μm (S_{ea} value was determined from the ‘ea’ versus ‘a’ plot, as illustrated in Figure F-1).

Error in crack length = ea = $\left(a_{N+\Delta N} - a_N\right) - \left[\left(\frac{da}{dN}\right) \times \Delta N\right]$

Uncertainty in crack length due to PD variation =

$$u(a)_{PD} = \left(\frac{\delta a}{a}\right)_{PD} = S_{ea} \times d_v = \pm 1.08 \times 1 = \pm 1.08 \text{ μm}$$

Combined uncertainty in crack length =

$$U_c(a) = \sqrt{\sum_{i=1}^{N}\left[c_i u(x_i)\right]^2} = \sqrt{\left[c_{PD} u(a)_{PD}\right]^2} = \sqrt{\left[1 \times 1.08\right]^2} = \pm 1.08 \text{ μm}$$

Expanded uncertainty in crack length =

$U(a) = U_c(a) \times k$

$= \pm 1.08 \times 2$

$= \pm 2.16$ μm

$= \pm$<u>0.00216 mm</u>

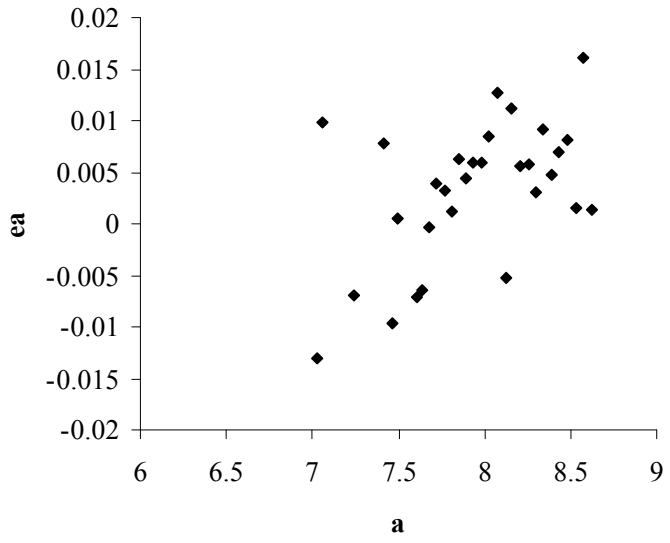

Figure K-1 ea vs. a

K2 Uncertainty in Stress-intensity-factor-range [U(ΔK)]

Sample Calculation:

Following analysis is based on ΔK = 25 MPa√m, corresponding to crack length of 0.9 mm.

K2.1 Uncertainty due to Alignment [$u(\Delta K)_a$]

Uncertainty in Instron alignment = ea = ±5% = ±0.05

$$u(\Delta K)_a = \left(\frac{\delta \Delta K}{K}\right)_a = \Delta K \times ea \times d_v = 25 \times \pm 0.05 \times 0.5 = \pm 0.625 \text{ MPa}\sqrt{m}$$

K2.2 Uncertainty due to Load Cell [$u(\Delta K)_l$]

Uncertainty in Instron load cell = ea = ±0.25% = ±0.0025

$$u(\Delta K)_l = \left(\frac{\delta \Delta K}{K}\right)_l = \Delta K \times ea \times d_v = 25 \times \pm 0.0025 \times 0.5 = \pm 0.03125 \text{ MPa}\sqrt{m}$$

Combined uncertainty in ΔK =

$$U_c(\Delta K) = \sqrt{\sum_{i=1}^{N}\left[c_i u(x_i)\right]^2} = \sqrt{\left[c_a u(\Delta K)_a\right]^2 + \left[c_l u(\Delta K)_l\right]^2}$$

$$= \sqrt{\left[1 \times 0.625\right]^2 + \left[1 \times 0.03125\right]^2} = \pm 0.488 \text{ MPa}\sqrt{m}$$

Expanded uncertainty in ΔK =

$U(\Delta K) = U_c(\Delta K) \times k$

$= \pm 0.488 \times 2$

$= \pm$<u>0.976 MPa√m</u>

K3 Uncertainty in da/dN [U(da/dN)]

Sample Calculation:

$$\frac{da}{dN} = \frac{\Delta a}{\Delta N} = \frac{\Delta a}{N_{average,(a=0.9mm)} - N_{average,(a=0.83mm)}} = \frac{0.9 - 0.83}{100472.8 - 97881} = 2.7 \times 10^{-5} \text{ mm/cycle}$$

$$\left(\frac{da}{dN}\right)_{S_N} = \frac{\Delta a}{\Delta N - S_N} = \frac{0.9 - 0.83}{(100472.8 - 97881) - 10145.445} = -9.3 \times 10^{-6} \text{ mm/cycle}$$

Error in da/dN =

$$u\left(\frac{da}{dN}\right) = \delta\left(\frac{da}{dN}\right) = \left[\left(\frac{da}{dN}\right)_{S_N} - \left(\frac{da}{dN}\right)\right] \times d_v$$

$$= \left[\left(-9.3 \times 10^{-6}\right) - \left(2.7 \times 10^{-5}\right)\right] \times 0.5$$

$$= \pm 1.815 \times 10^{-5} \text{ mm / cycle}$$

Combined uncertainty in da/dN =

$$U_c\left(\frac{da}{dN}\right) = \sqrt{\sum_{i=1}^{N}\left[c_i u(x_i)\right]^2} = \sqrt{\left[c \times u\left(\frac{da}{dN}\right)_a\right]^2}$$

$$= \sqrt{\left[1 \times (1.815 \times 10^{-5})\right]^2}$$

$$= \pm 1.815 \times 10^{-5} \text{ mm/cycle}$$

Expanded uncertainty in da/dN =

$U(da/dN) = U_c(da/dN) \times k$

$= \pm(1.815 \times 10^{-5}) \times 2$

$= \pm 3.63 \times 10^{-5}$ mm/cycle

BIBLIOGRAPHY

1. www.nuclear.energy.gov
2. A Technology Roadmap for Generation IV Nuclear Energy Systems, USDOE Nuclear Energy Research Advisory Committee and the Generation IV International Forum, December 2002
3. Time for next generation nuclear plants in USA, EIR Science and Technology, August 10, 2007, pp. 54-56
4. P. Yvon and F. Carre, "Structural Materials Challenges for Advanced Reactor Systems," *Journal of Nuclear Materials*, 2009. n. 385, pp. 217-222.
5. V. Marthandam, "Tensile Deformation, Toughness and Crack Propagation Study of Alloy 617," PhD Dissertation, UNLV, 2008.
6. M.H. Hasan, "Effects of Mechanical and Metallurgical Variables on Creep, Fracture Toughness and Crack Growth Behavior of Alloy 617," PhD Dissertation, UNLV, 2009.
7. M. Katcher and D.L. Klarstrom, "A Review of Haynes 230 and 617 Alloys For High Temperature Gas Cooled Reactors," *Material Science Forum*, 2008, v. 595-598, pp. 511-517.
8. Katherine Gray, "Creep Properties of Haynes 230 Alloy for NGNP Heat Exchangers," Materials Compatibility and Degradation in Advanced Nuclear Systems-II.
9. G.E. Dieter, Mechanical Metallurgy, Mc Graw Hill Book Company Limited, UK.
10. F.C. Campbell, Elements of Metallurgy and Engineering Alloys, ASM International.

11. L. Bendersky, A. Rosen and A.K. Mukherjee, "Creep and Dislocation Substructure," *International Metals Review*, 1985, v. 30, n. 1, pp. 1-15.
12. K. C. Valanis and C.F. Lee, "Deformation Kinetics of Steady State Creep in Metals," *International Journal of Solid Structures*, 1981, v. 17, pp. 589-604.
13. Javad Safari and Saeed Nategh, "Microstructural Evolution and its Influence on Deformation Mechanisms during High Temperature Creep of Nickel Base Superalloys," *Material Science and Engineering A*, 2009, v. 499, pp. 445-453.
14. R. A. Stevens and P.E.J. Flewett, "The Dependence of Creep Rate on Microstructure in a γ' Strengthened Superalloy," *Acta Metallurgica*, 1981, v. 29, pp. 867-882.
15. K. Shiozawa and J.R. Weertman, "The Nucleation of Grain Boundary Voids in a Nickel-Base Superalloy during High Temperature Creep," *Scripta Metallurgica*, 1982, v. 16, pp. 735-739.
16. H.M. Tawancy, "Nucleation of γ'' Phase in a Nickel Base Superalloy," *Journal of Material Science Letters*, 1992, v. 11, pp. 1446-1448.
17. M. Sundaram, W. Chen, and R.P. Wahi, "The Influence of Applied Creep Stress on Dislocation Distribution in a Nickel-Base Alloy," *Scripta* Metallurgica, 1989, v. 23, pp. 1021-1026.
18. J. Cadek et al, "On the Role of Recovery in Creep of Precipitation Strengthened Polycrystalline Nickel Base Alloys," *Material Science and Engineering A*, 1997, v. 238, pp. 391-398.
19. H.M. Tawancy, "Mechanisms of Dislocation-Particle Interaction during Creep Deformation of Selected Nickel-Base Alloys," *Journal of Material Science Letters*, 1995, v. 14, pp. 1421-1424.

20. J.L. Martin and A.S. Argon, "Low Energy Dislocation Structures due to Recovery and Creep," *Material Science and Engineering*, 1986, v. 81, pp. 337-348.

21. P. J. Henderson, "Dislocations at γ'/γ'' Interfaces during the Creep of Nickel-Base Superalloys," *Scripta Metallurgica*, 1988, v. 22, pp. 1103-1107.

22. R.R. Keller, H.J. Maier and H. Mughrabi, "Characterization of Interfacial Dislocation Networks in a Creep-Deformed Nickel-Base Superalloy," *Scripta Metallurgica et Materialia*, 1993, v. 28, pp. 23-28.

23. T. Link et.al, "<100> Dislocations in Nickel-Base Superalloys: Formation and Role in Creep Deformation," *Material Science and Engineering A*, 2005, v. 405, pp. 254-265.

24. H. M. Tawancy, "High Temperature Creep Behavior of a Ni-Cr-W-B Alloy," *Journal of Material Science*, 1992, v. 27, pp. 6481-6489.

25. D.B. Williams and E.P. Butler, "Grain Boundary Discontinuous Precipitation Reactions," *International Metals Review*, 1981, n. 3, pp. 153-183.

26. ASTM E139-06, "Standard Test Methods for Conducting Creep, Creep-Rupture, and Stress-Rupture Tests of Metallic Materials," 2007.

27. A.K. Roy, M.H. Hasan, J. Pal, "Creep Deformation of Alloys 617 and 276 at 750-950^{o}C," *Material Science and Engineering A*, 2009, v. 520, pp. 184-188.

28. F.A. Leckie, "The Micro- and Macromechanics of Creep Rupture," *Engineering Fracture Mechanics*, 1986, v. 25, n. 5/6, pp. 505-521.

29. A. Baldan, "On the Creep Rupture Life Prediction," *Journal of Material Science*, 1998, v. 33, pp. 3629-3637.

30. T.M. Kim, J. Yu, and J.Y. Jeon, "Creep Rupture in a Nickel Based Superalloy," *Metallurgical Transactions A*, 1992, v. 23A, pp. 2581-2587.
31. L.R. Liu et al, "Formation of Carbides and their Effects on Stress Rupture of A Nickel Base Single Crystal Superalloy,' *Materials Science and Engineering A*, 2003, v. 361, pp. 191-197.
32. K. Zhao, Y.H. Ma, L.H. Lou, "Improvement of Creep Rupture Strength of A Liquid Metal Cooling Directionally Solidified Nickel-Base Superalloys by Carbides," *Journal of Alloys and Compounds*, 2009, v. 475, pp. 648-651.
33. F. R. Larson and J. Miller, "A Time-Temperature Relationship for Rupture and Creep Stresses," *Transactions of ASME*, 1952, v. 74, pp. 765−775.
34. R. L. Orr, O.D. Sherby, and J.E. Dorn, "Correlations of Rupture Data for Metals at Elevated Temperatures," *Transactions of ASME*, 1954, v. 46, pp. 113-118.
35. S.S. Manson and A.M. Hafred, "Linear Time-Temperature Relation for Extrapolation of Creep and Stress Rupture Data," NASA TN2890, Mar 1952.
36. S.S. Manson and C.R. Ensign, "A Quarter-Century of Progress in the Development of Correlation and Extrapolation Methods for Creep Rupture Data," *Journal of Engineering Materials .and Technology*, 1979, v. 10, pp. 317-325.
37. B. Cotterell, "The Past, Present and Future of Fracture Mechanics," *Engineering Fracture Mechanics*, 2002, v. 69, pp. 533-553.
38. R.W. Hertzberg, Deformation and Fracture Mechanics of Engineering Materials, John Wiley and Sons Inc, 1996, pp. 359-369.

39. Xiao Guang, Zu Han Lai, "Realization of Single Specimen Analytical Method of J_{1C} Determination by using Compact Tension Loading," *Engineering Fracture Mechanics* , 1989, v. 34, n. 5/6, pp 1013-1021.
40. W.J. Mill, "Fracture Toughness of Two Ni-Fe-Cr Alloys," *Engineering Fracture Mechanics*, 1987, v. 26, n. 2, pp. 223-238.
41. Haynes 230 Alloy, High Temperature Alloys- Tech Brief, Haynes International, Jan 2003.
42. ASTM Designation E 813-1989, Standard Test Method for J_{1C}, A Measure of Fracture Toughness, American Society for Testing and Materials (ASTM) International.
43. ASTM Designation E 647-2000, Standard Test Method for Measurement of Fatigue Crack Growth Rates, American Society for Testing and Materials (ASTM) International.
44. ASTM Designation E 8-2004, Standard Test Methods for Tension Testing of Metallic Materials, American Society for Testing and Materials (ASTM) International.
45. BLUEHILL 2 Material Testing Software Program, INSTRON.
46. ASTM Designation E399, Standard Method for Linear-Elastic-Plane-Strain-Fracture Toughness (K_{IC}) of Metallic Materials, American Society for Testing and Materials (ASTM) International.
47. Instron Corp., Fast Track 2 - J_{1C} Unloading Compliance Software
48. B.K. Neale, "The Fracture Toughness Testing of Centre-Cracked Tensile Specimens using the Unloading Compliance Technique," *Engineering Fracture Mechanics*, 1998, v. 59, pp. 487-499.

49. J.E. Perez Ipiñaa, A.A. Yawnyb, R. Stukeb and C. Gonzalez Oliverb, "Fracture Toughness in Metal Matrix Composites," *Materials Research*, 2000, v. 3, pp. 74-78.

50. Richard W. Hertzberg, Deformation and Fracture Mechanics of Engineering Materials, Chapter 8, pp. 358-363.

51. S.S. Manson and C.R. Ensign, "Intrapolation and Extrapolation of Creep-Rupture Data by Minimum Commitment Method Part I Focal-Point Convergence," Characterization of Materials for Service at Elevated Temperatures, ASME/CSME Montreal Pressure and Piping Conference, Montreal, 1978, pp. 299-338.

52. M.R. Spiegel and L.J. Stephens, Schaum's Outline of Theory and Problems of Statistics, McGraw Hill Publication, 1999, Chapter 13 and 15.

53. R.W. Hertzberg, Deformation and Fracture Mechanics of Engineering Materials, John Wiley and Sons Inc, 1996, pp. 185-193.

54. GK. Sadananda, "Crack Propagation under Creep and Fatigue," *Nuclear Engineering and Design*, 1984, v. 83, pp. 303-323.

55. S. P. Lynch, T. C. Radtke, B. J. Wicks, R. T. Byrnes, Fatigue and Fracture of Engineering Materials and Structures, 1994, v. 17, pp.297-311.

56. ASTM Designation E 647-2000, Standard Test Method for Measurement of Fatigue Crack Growth Rates, American Society for Testing and Materials (ASTM) International.

57. P.C. McKeighan and D.J. Smith, "Determining the Potential Drop Calibration of a Fatigue Crack Growth Specimen Subject to Limited Experimental Observations," *Journal of Testing and Evaluation*, 1994, v. 22, n. 4, pp. 291-301.

58. Fracture Technology Associates, Automated Fatigue Crack Growth Testing – Series 2001, V3.03.02a.
59. ASTM Designation E 112-96, "Standard Test Methods for Determining Average Grain Size," American Society for Testing and Materials (ASTM) International, West Conshohocken, PA, 2004.
60. E.E. Underwood, Quantitative Stereology, Addison-Wesley Publishing Company, Reading, MA, 1970.
61. L. Ma, "Comparison of Different Sample Preparation Techniques in TEM Observation of Microstructure of Inconel Alloy 783 Subjected to Prolonged Isothermal Exposure," *Micron*, 2004, v. 35, n.4, pp. 273-279.
62. P. E. Fischione, "Materials Specimen Preparation for Transmission Electron Microscopy," E. A. Fischione Instruments, Inc. Export, PA, USA.
63. ASM Handbook, "Metallography and Microstructures," Publisher: ASM International, v. 9, Materials Park, OH, 2004.
64. K. Yabusaki and H. Sasaki, "Specimen Preparation Technique for a Microstructure Analysis using the Focused Ion Beam Process," Furukawa Review, 2002, n. 22.
65. J. Pal, "Fracture Toughness, Crack-Growth-Rate and Creep Studies of Alloy 276," PhD Dissertation, UNLV, 2009.
66. A. K. Roy, M. H. Hasan and J. Pal, "Creep Deformation of Alloys 617 and 276 at 750-950 °C," *Materials Science and Engineering A*, 2009, v. 520, n. 1-2, pp. 184-188.

67. K.S. Chan, Y.M. Pan and Y.D. Lee, "Computation of Ni-Cr Phase Diagram via a Combined First-Principles Quantum Mechanical and CALPHAD Approach," *Metallurgical and Materials Transactions A*, July 2006, v. 37A, pp. 2039-2050.
68. M. Hirabayashi et al, "An Experimental Study on the Ordered Alloy Ni_2Cr," *Transactions of Japan Institute of Metals*, 1969, v. 10, pp. 365-371.
69. L. Karmazin, "Lattice Parameter Studies of Structure Changes of Ni-Cr Alloys in the Region of Ni_2Cr," *Material Science and Engineering*, 1982, v. 54, pp. 247-256.
70. A. R. Ibañez, A. Saxena and J. D. Kang, "Creep Behavior of a Directionally Solidified Nickel Based Superalloy," *Strength, Fracture and Complexity*, 2006, v. 4, n. 2, pp. 75-81.
71. Y. L. Lu et.al., "Hold-time Effect on the Elevated-Temperature Crack Growth Behavior of Solid-solution-strengthened Superalloys," *Acta Materialia*, 2007, v. 55, pp. 767-775.
72. Haynes On-line Literature, No. H-3000, Haynes 230 Alloy Brochure, www.haynesintl.com.
73. Haynes On-line Literature, No. H-3171B, Haynes 617 Alloy Brochure, www.haynesintl.com.
74. Online Technical Data- Alloy800H, http://www.cornes.com.sg/a800h.htm.
75. P. Georgsson, "The Determination of Uncertainties in Fatigue Crack Growth Measurement," Manual of Codes of Practice for the Determination of Uncertainties in Mechanical Tests on Metallic Materials, Standards Measurement & Testing Programme, Issue 1, 2000.

76. BIPM, IEC, IFCC, ISO, IUPAC, OIML, “Guide to the Expression of Uncertainty in Measurement,” International Organization for Standardization, Geneva, Switzerland, 1st Edition, 1993.

VITA

Graduate College
University of Nevada, Las Vegas

Sudin Chatterjee

Degrees:

Bachelors of Engineering, Metallurgical Engineering, 1999
National Institute of Technology (previously, Regional Engineering College)
Rourkela, India

Masters of Technology, Materials and Metallurgical Engineering, 2001
Indian Institute of Technology (IIT)
Kanpur, India

Journal Articles:

1. A. K. Roy, S. Chatterjee, M. H. Hasan, J. Pal and L. Ma, Crack Growth Behavior of Alloy 230 under Creep-Fatigue Conditions, accepted for publication in Material Science and Engineering A.
2. Sudin Chatterjee and Ajit K Roy, Microstructural Evolution and Overall Mechanism of Creep Deformation in Alloy 230, under review.
3. A. Saha Podder, D. Bhattacharjee, Sudin Chatterjee and R. K. Ray, Evolution of Microstructure and Texture during Annealing of Two Interstitial Free Steels containing Nb and/or Ti, Material Science and Technology, 2009, 25, 12, pp. 1417-1421.
4. Sudin Chatterjee, A K Verma and Ananya Mukhopadhyay, Static Recrystallization of Nb, Ti, and V Microalloyed Steel during Hot Deformation, Ironmaking and Steelmaking, 2007, 34, 2, pp. 145-150.
5. Saurabh Kundu, Ananya Mukhopadhyay, Sudin Chatterjee and Sanjay Chandra, Modelling of Microstructure and Heat Transfer during Controlled Cooling of Low Carbon Wire Rod, ISIJ International, 2004, 44, 7, pp. 1217-1223.
6. Sudin Chatterjee, A K Verma, Ananya Mukhopadhyay, Static Recrystallization of Hot Deformed Austenite In Microalloyed Steels, Tata Search 2006.
7. Sudin Chatterjee et al, An Insight into the Outer Body Panels of Passenger Cars, Tata Search 2006.
8. Sudin Chatterjee, Saurabh Kundu, Ananya Mukhopadhyay and Sanjay Chandra, Modelling of Microstructure Evolution during Controlled Cooling of TMT re-bars, TataSearch, 2005.
9. A. Haldar, Sudin Chatterjee, Nitin Kumar, Hall Petch Relationship in Low and Ultra Low Carbon Steels, TataSearch, 2005.
10. A.Murugaiyan, A N Bhagat, Arijit Sahapodder, Sudin Chatterjee and N.Gope, Recrystallization Kinetics of Cold Rolled Ultra Low Carbon Steels, Tata Search, 2004.

Conference Presentations:

1. Muhammad Hasan, Joydeep Pal, Ajit Roy and Sudin Chatterjee, Time and temperature-dependent deformation of Alloy 617, TMS 2009 Conference, 22-26 Feb 2009, San Francisco, USA.
2. Shylu John, Saurabh Kundu, Ananya Mukhopadhyay, Sudin Chatterjee and Partha Majumdar, A complete simulation system for wire and rod rolling, International Conference on Long Products –'The challenges and opportunity', 9-10 Feb 2004, Jamshedpur, India.
3. Ananya Mukhopadhyay, Saurabh Kundu, Sudin Chatterjee and Sanjay Chandra, Modelling of Microstructure during Controlled Cooling of TMT wire rod, SIMPRO'04, Sept. 2004, Ranchi, India.

Dissertation Title: "Mechanical Behavior of Alloy 230 at Temperatures Relevant to NGNP Program."

Dissertation Examination Committee:

Chairperson, Brendan O'Toole, Ph.D.
Co-Chairperson, Ajit K. Roy, Ph.D.
Committee Member, WooSoon Yim, Ph.D.
Committee Member, Anthony E. Hechanova, Ph.D.
Committee Member, Daniel Cook, Ph. D.
Graduate Faculty Representative, Edward S. Neumann, Ph.D.